Quantum Magnetism in Synthetic Systems

Rossi, Dario

How to cite

ROSSI, Dario. Quantum Magnetism in Synthetic Systems. Thèse, 2026. doi: 10.13097/archive-ouverte/unige:191287

This publication URL: https://archive-ouverte.unige.ch/unige:191287
Publication DOI: 10.13097/archive-ouverte/unige:191287

UNIVERSITÉ DE GENÈVE
Section de Physique
Département de physique théorique

FACULTÉ DES SCIENCES
Professeur Louk Rademaker
Professeur Dmitry A. Abanin

Quantum Magnetism in Synthetic Systems

THÈSE

présentée à la Faculté des Sciences de l'Université de Genève
pour obtenir le grade de docteur ès Sciences, mention Physique

par

Dario Rossi
de
Correggio, RE (Italie)

Thèse n° 5969

GENÈVE
Atelier d'impression ReproMail
2026

DOCTORAT ÈS SCIENCES, MENTION PHYSIQUE

Thèse de Monsieur Dario ROSSI

intitulée :

«Quantum Magnetism in Synthetic Systems»

La Faculté des sciences, sur le préavis de

Monsieur L. RADEMAKER, professeur assistant et directeur de thèse
Département de Physique de la matère quantique

Monsieur D. ABANIN, professeur et codirecteur de thèse
Department of Physics, Princeton University , United States of America

Monsieur F. BAUMBERGER, professeur ordinaire
Département de Physique de la matière quantique

Monsieur R. THOMALE, professeur
Fakultät für Physik und Astronomie, Würzburg Universtität, Würzburg, Deutschland

autorise l'impression de la présente thèse, sans exprimer d'opinion sur les propositions qui y sont énoncées.

Genève, le 23 janvier 2026

Thèse - 5969 -

La Doyenne

N.B. - La thèse doit porter la déclaration précédente et remplir les conditions énumérées dans les "Informations relatives aux thèses de doctorat à l'Université de Genève".

To the people who made it possible.

“Moria... You fear to go into those mines. The dwarves delved too greedily and too deep. You know what they awoke in the darkness of Khazad-dum... shadow and flame.”
— J. R. R. Tolkien

Acknowledgements

At the end of a long journey-such as the four years I spent in Geneva working on my PhD-I find comfort in looking back on the many good moments I experienced and the people I had the pleasure of meeting along the way. What follows is a brief list of those who were important to me, both scientifically and personally.

First of all, I am deeply thankful to my supervisor Dima, for all the exciting work we did together and for always giving the right direction when the path to follow was unclear. My deeper thanks also go to my supervisor Louk, who I first met as a post-doc and was extremely helpful to follow me as supervisor for the second part of my PhD. The discussions with Louk I hold dearest, as his ways of explaining often complicated concepts always found a way to become simple.

I am deeply grateful to my friend, mentor and collaborator Johannes. Scientifically, I cannot stress enough how much most of what I accomplished is thanks to his help, support and also patience sometimes because of all the questions I asked him. But the support he gave me goes beyond this, in all the coffees we had and the cheddar tastings and the snowboard days in the mountains. Thank you very much for your friendship!

Many people made this thesis possible. I would like especially to thank my experimental collaborators: Alberto Morpurgo and Fengrui Yao for the work we did together on Chromium Bromite, Felix Baumberger, Gianmarco Gatti and Julia Issing for the ongoing work on WSe_2/WS_2 and Trond Andersen, Nikita Astrakhantsev and Jeronimo Martinez from the Google quantum AI collaboration. On the theoretical side, I am grateful for the useful discussions with Alessio Lerose, Alexios Michialidis, Julian Thoenniss, Jerome Lloyd and Michael Sonner.

I made many friends, both within and beyond the university, who made this journey truly meaningful. I would like to thank Julian in particular, for sharing both the good and the difficult moments, as well as a couple of well-deserved vacations. My sincere thanks go to Jerome, with whom I began my PhD; we shared many of the most exciting experiences of this journey, and whom I also have to thank (or blame) for introducing

me to climbing in Geneva. I am deeply grateful to Margherita for her unwavering support and help, especially during the final years of the PhD, when deadlines weighed heavily and my morale was at its lowest. She inspires me every day and reminds me of the value and goodness in the work we do.

I want to thank Lorenzo, for the 6 years and counting of friendship which I value very dear, and for showing me how to do a pretzel with the snowboard! Special thanks to Ivo for the uncountable experiences climbing, skiing and the many alpine adventures, pizzas and volleyball. If I got so much into mountains is also thanks to your enthusiasm, and if I am still here to write these acknowledgments is also thanks to your experience which often balances my recklessness. On the same line I want to thank Christophe, Giacomo, Michael, Michael (not a typo), Wouter, Valentin, Adriano, Florian and David for all the incredible adventures in the mountains which made these years exciting and truly memorable. My deep thanks also go to Anna, whose friendship, despite beginning in the worst possible conditions, has grown into a truly meaningful bond. My thanks to Lucia, with whom I shared my “loonines” and many great moments. I want to thank Giulia V., for always bringing a touch of fun in every situation, and Julia for all the help during the writing of the thesis. My heartfelt thanks to Ludovica for her friendship and for being so patient having me as a flatmate for the past 2 years.

I want to thank my friends from the years of the undergrad in Bologna, my dear Gallabra. I am truly grateful for all the moments we managed to spend together during these years scattered apart and in particular for all the holidays we managed to organize at the last second. These periods were always a re-charging period for my soul.

Thanks also to my friends from my hometown, in particular to Marcello, Riccardo, Joe, Luigi e Federico. And thanks to my partners in crime Francesco e Simone, for their long-time support and friendship.

Finally, I would like to thank my family for being always helpful and of support during all my life. Especially to my sister Irene, who was there during the darkest and brightest moments. Thank you from the heart!

Résumé en français

Cette thèse explore le magnétisme quantique dans des systèmes synthétiques bidimensionnels, où les fortes corrélations, la frustration géométrique et l'amplification des fluctuations quantiques donnent naissance à des phases magnétiques non conventionnelles. Dans ce manuscrit, je me concentre sur deux grandes classes de plateformes artificielles: les matériaux de moiré et les simulateurs quantiques. Ces systèmes synthétiques offrent un contrôle sans précédent sur la géométrie du réseau, les intensités d'interaction et les protocoles dynamiques, permettant d'accéder à des régimes inatteignables par les approches traditionnelles de la physique de la matière condensée.

Le premier projet concerne le magnétisme de moiré dans des multicouches de $CrBr_3$ soumises à une contrainte mécanique. Dans ce système, la superstructure de moiré est générée par une déformation plutôt que par un angle de rotation, produisant ainsi une modulation spatiale de l'échange inter-couche alternant entre ferromagnétisme et antiferromagnétisme. En raison du moment magnétique $S = 3/2$, le système admet une description classique de bicouche avec des interactions en compétition. Je développe un cadre théorique qui permet de décrire les ordres non collinéaires qui en résultent et de tenir compte des signatures expérimentales du magnétisme de moiré induit par la contrainte. Ceci exemplifie comment l'ingénierie de moiré peut stabiliser des textures magnétiques non triviales.

Le deuxième projet porte sur le magnétisme quantique dans une hétéro-bicouche WSe_2/WS_2 à dopage $n = 3/4$, où les électrons se localisent sur un réseau kagome effectif. À partir du modèle de Hubbard décrivant les bandes de moiré, j'obtiens un Hamiltonien de Heisenberg frustré comprenant plusieurs termes d'échange en compétition. En utilisant une théorie de champ moyen en bosons de Schwinger, j'établis un diagramme de phases montrant une compétition entre ordres non collinéaires et phases de liquide de spin. Pour des paramètres réalistes, l'état fondamental est un liquide de spin chiral, ce qui met en avant les dichalcogénures de métaux de transition moiré comme des plateformes prometteuses pour la réalisation de phases magnétiques topologiques et fortement corrélées.

Le troisième projet étudie la dynamique de transition de phase quantique au moyen de simulateurs quantiques basés sur des circuits supraconducteurs, en se concentrant sur des rampes d'Hamiltoniennes dans le modèle XY bidimensionnel. Un protocole analogique-numérique fait évoluer le système d'un état en escalier avec gap vers la phase XY sans gap. En analysant les corrélations obtenues, j'extrais la loi d'échelle de la longueur de corrélation en fonction de la vitesse de la rampe et la compare aux prédictions de Kibble–Zurek. Bien que globalement cohérents avec cette théorie, les résultats présentent une anomalie reflétant les effets de taille finie, de dimensionnalité et de contraintes expérimentales.

Le quatrième projet consiste en une description en ondes de spin de Holstein-Primakoff appliquée aux mêmes rampes du modèle XY. Comme la magnétisation se réoriente au cours de l'évolution, l'axe de quantification est ajusté à chaque instant à la direction du paramètre d'ordre, ce qui permet d'obtenir une théorie quadratique résoluble pendant toute la rampe. Ce cadre donne accès aux dispersions de magnons, à des corrélations dépendant du temps et de l'espace, ainsi qu'aux dynamiques d'excitations à un seul magnon, incluant leur décroissance et leur diffusion dans un environnement thermique. Ce travail fournit une description détaillée de la dynamique hors équilibre des quasi-particules dans un aimant bidimensionnel soumis à des champs dépendants du temps.

Ensemble, ces quatre projets montrent comment les matériaux moiré et les simulateurs quantiques permettent une exploration contrôlée du magnétisme frustré et fortement corrélé en deux dimensions. En combinant modélisation analytique et conditions expérimentales réalistes, cette thèse contribue à la compréhension de la manière dont la frustration, la topologie et la dynamique hors équilibre façonnent les phénomènes magnétiques quantiques dans les systèmes de basse dimension.

Abstract

This thesis investigates quantum magnetism in two-dimensional synthetic systems, where strong correlations, geometric frustration, and enhanced quantum fluctuations give rise to unconventional magnetic phases. In this manuscript I focus on two major classes of engineered platforms: moiré materials and quantum simulators. These synthetic systems offer unprecedented control over lattice geometry, interaction strengths, and dynamical protocols, enabling access to regimes beyond the reach of conventional condensed-matter approaches.

The first project concerns moiré magnetism in strained multilayers of $\mathrm{CrBr_3}$. Here the moiré pattern is generated by strain rather than twist, producing a spatial modulation of the interlayer exchange that alternates between ferromagnetic and antiferromagnetic. Owing to the $S = 3/2$ moments, the system admits a clear classical bilayer description with competing interactions. I develop a theoretical framework that captures the resulting non-collinear orders and accounts for the experimental signatures of strain-induced moiré magnetism, illustrating how moiré engineering can stabilize non-trivial magnetic textures.

The second project examines quantum magnetism in a $\mathrm{WSe_2}$/$\mathrm{WS_2}$ hetero-bilayer at $n = 3/4$ filling, where electrons localize into an effective kagome lattice. From the underlying Hubbard model, I derive a frustrated Heisenberg Hamiltonian with several competing exchanges. Using a Schwinger-boson mean-field theory, I map out a phase diagram featuring competing non-collinear orders and spin-liquid phases. For realistic parameters, the ground state is found to be a chiral spin liquid, highlighting transition metal dichalcogenide moiré materials as promising platforms for realizing topological and strongly correlated magnetic phases.

The third project investigates quantum phase-transition dynamics using superconducting circuit quantum simulators, focusing on Hamiltonian ramps in the 2D XY model. An analogue-digital protocol drives the system from a gapped staggered

state into the gapless XY phase. By analyzing the resulting correlations, I extract the scaling of the correlation length with ramp rate and compare it to Kibble–Zurek predictions. While overall consistent with Kibble–Zurek theory, the results exhibit an anomaly reflecting the effects of finite size, dimensionality, and experimental constraints.

The fourth project consists in a Holstein–Primakoff spin-wave description for the same XY ramps. As the magnetization reorients along the evolution, the quantization axis is adapted to the instantaneous order parameter, enabling a solvable quadratic theory throughout the ramp. This framework provides access to magnon dispersions, time- and space-dependent correlations, and the dynamics of single-magnon excitations, including their decay and scattering in a thermal environment. This study yields a detailed picture of non-equilibrium quasiparticle dynamics in a two dimensional magnet evolving under time-dependent fields.

Together, these four projects demonstrate how moiré materials and quantum simulators enable controlled investigations of frustrated and strongly correlated magnetism in two dimensions. By combining analytical modeling with experimentally relevant conditions, this thesis contributes to understanding how frustration, topology, and non-equilibrium dynamics shape quantum magnetic phenomena in low-dimensional systems.

Publication List

[1] F. Yao, **D. Rossi** et al., *Moiré magnetism in* $CrBr_3$ *multilayers emerging from differential strain*, Nat. Commun. **15**, 10377 (2024)

[2] J. Motruk, **D. Rossi**, D. A. Abanin, L. Rademaker, *Kagome chiral spin liquid in transition metal dichalcogenide moiré bilayers*, Phys. Rev. Research, **5**, L022049 (2023)

[3] **D. Rossi**, J. Motruk, L. Rademaker, D. A. Abanin, *Schwinger boson study of the* J_1-J_2-J_3 *kagome Heisenberg antiferromagnet with Dzyaloshinskii-Moriya interactions*, Phys. Rev. B **108**, 144406 (2023)

[4] T. I. Andersen, …**D. Rossi** et al., *Thermalization and criticality on an analogue–digital quantum simulator*, Nature **638**, 79-85 (2025)

Contents

CHAPTER 1

Introduction

Quantum magnetism The subject of this thesis is quantum magnetism, which is the study of how interacting quantum spins -usually the localized magnetic moments of electrons in a solid- organize themselves when quantum mechanics, not classical energetics alone, controls their behavior. At the microscopic level the simplest, effective description is the quantum Heisenberg model [5], where neighboring spin-$1/2$ (or higher-S) moments interact through exchange couplings and the Hamiltonian is an operator whose ground state and low-energy excitations are governed by superposition, entanglement and fundamentally quantum fluctuations. In two dimensions (2D) this physics is especially rich: quantum fluctuations are enhanced relative to three dimensions, geometry and frustration produce strong competition between many possible orders, and novel phases that have no classical analogue -such as quantum spin liquids and topologically ordered states- can appear [6].

A few conceptual pillars make 2D quantum magnetism unusual. First, the Mermin-Wagner theorem [7] states that continuous symmetries cannot be spontaneously broken at finite temperature in systems with dimension $d \leq 2$, meaning that spin rotational symmetry cannot be broken to produce conventional long-range magnetic order; quantum order at $T = 0$, however, remains possible and is determined by the balance of exchange, anisotropy and lattice geometry, specifically frustration. This separates the thermodynamic behavior at finite T from the richer quantum ground-state possibilities that appear at zero temperature. Second, the idea that a magnetically disordered but highly entangled ground state can exist - a *quantum spin liquid* - was proposed early on in the resonating-valence-bond (RVB) picture [8]. In RVB states spins form a liquid of singlets rather than a static Néel pattern; these states naturally support fractionalized excitations (spinons) and emergent gauge fields. The RVB viewpoint has been foundational for the analysis of many 2D quantum magnets.

Theory and solvable models have cemented that 2D magnets can host qualitatively new physics. A paradigmatic example is the Kitaev honeycomb model [9], an exactly solvable 2D spin-$1/2$ Hamiltonian whose ground states include gapped and gapless spin liquids with emergent Majorana fermions and anyonic excitations; this model demonstrates explicitly how highly anisotropic bond-dependent interactions can fractionalize spins and produce topological order. Such models give controlled theoretical footholds for thinking about experimental candidate materials and quantum information applications. Experimentally, 2D quantum magnetism on layered materials has matured from single-crystal neutron scattering and thermodynamic probes showing conventional antiferromagnetism to striking observations consistent with spin liquids. A celebrated example is the kagome-lattice material herbertsmithite [10], where inelastic neutron scattering finds a broad continuum of spin excitations rather than sharp spin waves -interpreted as evidence for fractionalized spinon excitations expected in a quantum spin liquid [11]. Advances like that, together with a steady stream of new 2D magnetic materials (organics [12], oxide layers, and spin-orbit entangled magnets), have turned theoretical possibilities into lab-testable phenomena. 2D magnets are also intimately connected to major problems in condensed matter: the parent antiferromagnetism of high-Tc cuprates [13], unconventional superconductivity emerging from doped Mott insulators [14], and candidate platforms for fault-tolerant quantum computation (via non-Abelian anyons or protected edge states) [15, 16].

Synthetic systems In the context of quantum magnetism, synthetic systems refer to engineered platforms that mimic the essential physics of interacting spins under controlled conditions. Unlike naturally occurring crystalline magnets, these synthetic platforms allow for tunable geometry, interaction strength, frustration, dimensionality, and external fields. Two major and complementary classes of synthetic systems that are playing an increasingly important role are *moiré hetero-structures* [17] and *quantum simulators* [18] designed to implement spin Hamiltonians directly. On the more condensed matter side, moiré systems arise when two two-dimensional layers of Van der Waals-type materials are stacked with a small relative twist angle or slight lattice mismatch, yielding a long-wavelength periodic modulation (the moiré superlattice) which dramatically reshapes the electronic band structure. In flat bands, the kinetic energy of electrons is reduced in favor of interactions, which in turn allows us to study correlated electron physics. Because these systems are highly tunable through twist angle, gating, straining and external fields, they serve as synthetic quantum magnets in two dimensions [19]: one can effectively dial the parameters of a 2D spin (or Hubbard)-type Hamiltonian, explore magnetically ordered and disordered phases, and probe quantum fluctuations. On the other hand we have quantum simulators, which are engineered, controllable quantum systems whose Hamiltonians can be tuned and whose evolution and measurement can be precisely controlled. Originally envisaged by Richard Feynman [20], they now include a variety of platforms such as superconducting qubits/circuits [21], ultracold atoms in optical lattices [22], trapped ions [23] and Rydberg-atomic arrays [24]. In the context of 2D quantum magnetism, quantum simulators allow direct realization of spin Hamiltonians in two spatial dimensions and direct observation of ground-state correlations, dynamics after quenches, frustrated magnetism, spin liquids, and phase transitions.

Methods The theoretical investigation of strongly correlated electron systems in two spatial dimensions is a major challenge, and several tools have been developed over the years to tackle this problem, each with its set of advantages and limitations. If the model at hand is not integrable, the only exact method possible is that of *exact diagonalization* (ED). ED provides numerically exact results for finite-size systems by fully diagonalizing the many-body Hamiltonian. It is particularly useful for benchmarking approximate methods and for probing excitation spectra, dynamical correlations, and topological signatures. For frustrated magnets, ED has been central in identifying models with candidate spin-liquid ground states and characterizing their symmetry properties [25, 26]. The main limitation of ED is the exponential growth of the Hilbert space with system size, restricting calculations to clusters of a few dozen sites at most. One of the major advances from the numerical side has come from tensor network techniques, in particular from the *density matrix renormalization group* (DMRG) [27]. Originally developed for one-dimensional systems, DMRG has become one of the most powerful methods for studying quasi-2D frustrated magnets. By systematically truncating the Hilbert space based on entanglement, DMRG achieves high accuracy for ground-state properties while retaining manageable computational cost. In 2D, DMRG is typically applied to cylinder geometries [2, 28], which allow access to larger systems than exact diagonalization but with some limitations from boundary effects. However, its efficiency decreases with system width due to the rapid growth of entanglement entropy, restricting the accessible lattice sizes. Another method which is very powerful for a certain set of systems is *quantum Monte Carlo* (QMC) [29]. QMC methods simulate quantum systems stochastically, offering access to large system sizes and finite-temperature properties. When applicable, QMC provides essentially exact results with controllable statistical errors. For non-frustrated magnets, it has been extremely successful in mapping out phase diagrams and critical behavior. However, in frustrated systems the notorious sign problem often renders QMC impractical, as negative weights in the sampling process cause exponential growth of statistical noise.

In this thesis I will primarily use mean-field theory methods to approach quantum magnetism. Mean-field theory (MFT) remains one of the most widely used and conceptually clear approaches for studying these systems in two dimensions. Its main limitation lies in its simplifying assumption: each spin experiences only an average effect from its neighbors, neglecting spatial correlations and quantum entanglement. As a result, MFT can fail to capture crucial 2D phenomena dominated by quantum fluctuations. Despite these shortcomings, mean-field theory provides a powerful and intuitive framework for studying quantum magnetism in two dimensions. It yields an analytically transparent and computationally efficient framework for mapping out phase diagrams, estimating critical points, and identifying candidate ordered phases. MFT often serves as a valuable first approximation or reference point for the more advanced methods mentioned above. Using different mean-field methods depending on the system under study, one can capture key qualitative features of low-dimensional quantum magnets and guide both theoretical and experimental investigations.

This thesis is divided into two parts, each discussing quantum magnetism emerging in the two main synthetic systems introduced above: moiré systems and quantum simulators.

Moiré Systems

The first part is dedicated to moiré systems. This subject has seen rising interest since the first proposal by Bistritzer and MacDonald [30] of a *magic angle* in twisted bilayer graphene where the resulting flat bands would result in a platform with the possibility to unveil many phenomena inherent to strong electronic correlations. A moiré lattice may be created by twisting two 2D materials (twisted bilayer), or by superimposing two lattices with different lattice constant, which can be due to different chemical composition (hetero-bilayer) or also by strain applied on of the layers (strained bilayer).

In this part of my thesis, I will discuss two examples in which moiré systems are used to study magnetism. In chapter 2, I discuss the observation of strain-induced moiré magnetism in a stack of $CrBr_3$ magnetic layers [1]. The moiré periodicity emerges due to the strain applied by the contacts on one side of the stack by a metallic gate. From a theoretical perspective, this system is of great interest since in addition to the intra-layer ferromagnetic coupling, the inter-layer exchange varies from ferromagnetic to antiferromagnetic depending on the stacking [31]. Due to the high-spin value of $3/2$, the system's magnetic properties, though of quantum origin, can be treated "classically" as a bilayer of magnetic sites with competing interactions, the result of which are various non-collinear magnetic orders. In this chapter, I describe the characteristics of the experiment that proves the presence of moiré magnetism and in particular I lay down the theoretical description we developed to describe the system. This project is a good starting point since it shows how magnetism may arise in moiré systems and it has a very intuitive classical description.

Following the discovery of correlated insulating phases and unconventional superconductivity in twisted bilayer graphene [17, 30, 32, 33], the landscape of experimental platforms hosting strongly correlated electrons has significantly increased.

Bilayers consisting of transition metal dichalcogenides (TMD) have emerged as particularly promising, as they exhibit even stronger electronic correlations than their graphene-based counterparts [34]. TMD moiré bilayers are a good platform to study quantum magnetism, since when charge degrees of freedom become localized, only the spin dynamics remain active, opening the door to emergent magnetic phenomena [35–37]. In chapter 3, I focus on the study of the emergent magnetic properties of a WSe_2/WS_2 hetero-bilayer. The moiré properties of this compound are also extremely rich, and the determination of how the moiré periodicity influences the electronic band structure is currently under study [38, 39]. In this chapter, I report on this hetero-bilayer's magnetic properties: I first show [2] how from the Hubbard model describing the moiré system one can derive an effective Heisenberg Hamiltonian governing the spins, which at $n = 3/4$ filling are localized on a kagome lattice. While in [2] we used DMRG to determine the phase diagram of this system, I will focus mostly on the work carried out in [3], in which I developed a Schwinger boson mean-field theory to solve this model. The high degree of frustration of the kagome lattice and the competition between further neighbor exchange interactions result in a rich phase diagram with various spin liquid and magnetic long-range orders. In particular, we find that for physically relevant WSe_2/WS_2 parameters, the system should host a *chiral* spin liquid ground state, making it a strong candidate for the possible observation of this highly-sought-for exotic phase of matter.

Quantum Simulators

In the second part of the thesis, I will discuss results obtained studying quantum magnetism by means of quantum simulators realized in superconducting quantum chips. The recent technological maturation of superconducting quantum processors has made possible the exploration of exotic phases with a level of control which is unattainable in solid-state platforms. This is the ideal playground to test theory and numerical methods, since the size of the attainable experimental systems are now closely approaching the limit of what it is possible to simulate numerically.

In chapter 4, I give an introduction to the field of superconducting quantum chips and set the stage for the results we obtained in studying Hamiltonian ramps for the ground state preparation [4] of the 2D XY model. In particular, I will show how by means of an *analogue-digital* technique, it is possible to perform time evolution on a system of qubits in order to ramp the state from a gapped staggered-field Néel-like state to the gapless XY model. This method was employed in [4] where we showed that by varying the ramp time, the state gets increasingly closer to the ground state of the gapless phase, following the expected behavior of the Kibble-Zurek [40,41] (KZ) mechanism, but with a surprising anomaly. My main contribution in this work was in the determination of the scaling behavior of the correlation length across the quantum phase transition as expected from the KZ mechanism, and in the interpretation of the results.

Finally, in chapter 5 I describe my contribution to the understanding of the dynamical properties of the 2D XY model. In order to give a theoretical description of the quantum dynamics which could be observed on a digital-analog quantum simulator, I employ a Holstein-Primakoff [42] spin wave expansion to describe the system along the ramp. The system transitions from a gapped staggered state to a gapless XY phase, meaning that its magnetization along the ramp will change depending on the parameters of the Hamiltonian. By changing the quantization axis depending on the local direction of the magnetization, it is possible to derive a solvable theory over which to compute eigenstates and correlation functions. Thanks to this technique we are able to describe in detail the magnon excitations in the system and compute spatial and time dependent correlation functions from which one can derive accurate information about the magnon contributions. Finally, I also describe how to create single magnon excitations and the consequent results of their decay and scattering with a thermal environment.

Part I

Moiré Systems

CHAPTER 2

Moiré Magnetism in Strained Chromium Bromide

2.1 Introduction

One experimentally accessible route to engineer moiré superlattices in two dimensional (2D) materials is to introduce strain between adjacent layers of the same compound. While this may seem like a straightforward geometrical manipulation, the underlying physics that emerges from such moiré structures is remarkably rich and far from trivial. The long-wavelength periodicity associated with moiré patterns can give rise to a wide range of novel physical phenomena, many of which are still being uncovered [43].

In the case of magnetic van der Waals materials, moiré engineering has recently opened a new frontier, often referred to as *moiré magnetism*. Since in each moiré unit cell the stacking configuration varies, this can lead to spatially inhomogeneous couplings and thus to highly tunable and inhomogeneous magnetic landscapes. Beyond its fundamental interest, moiré magnetism holds promise for practical applications [19], such as the development of energy-efficient spintronic devices, electrically tunable magnetic memories, and as a platform for realizing exotic quasiparticles—including Majorana zero modes and topological magnons—that could become building blocks for fault-tolerant quantum computation.

In this chapter, I focus on a specific realization of moiré magnetism in chromium trihalides, namely $CrBr_3$ multilayers. The work has been carried out in collaboration with the group of Prof. Morpurgo at the University of Geneva [1], and is centered around the experimental observation of unusual magnetotransport properties in $CrBr_3$ tunnel barriers. In these devices, Fe_3GeTe_2 and graphene were employed as electrodes to contact the barrier. A striking feature of the experiments was that the magnetoconductance spectra obtained with Fe_3GeTe_2 contacts exhibited features absent in the devices using graphene. This contrast immediately pointed to the role of the contact material in modifying the electronic and magnetic response of the $CrBr_3$ barrier.

Through our theoretical analysis, we show that these features can be consistently explained by the presence of differential strain exerted on the $CrBr_3$ stack by the Fe_3GeTe_2 contact. This strain gives rise to a moiré periodicity across the multilayer, such that a single moiré unit cell effectively samples all possible stacking configurations of $CrBr_3$ layers (see e.g. Figure 2.1a-c). Importantly, previous work by a collaborator [31] demonstrated that different stacking geometries in chromium halides correspond to markedly different interlayer exchange couplings, ranging from strongly ferromagnetic to antiferromagnetic. As a result, the moiré structure naturally imprints a modulation of the magnetic exchange landscape, which in turn leaves a measurable fingerprint in the magnetoconductance.

In this chapter, I go through the results published in [1] with a focus on the theoretical description. In section 2.2, I describe the experimental setting and the magnetotransport measurements performed on $CrBr_3$. We show that the jumps observed in the magnetoconductance can be attributed to structural deformations of the strained $CrBr_3$ multilayer. In section 2.3, I outline and expand the theoretical framework we developed, emphasizing the connection between strain-induced moiré structures and the emergence of moiré magnetism in $CrBr_3$. Finally, in section 2.4 I illustrate the numerical results and the comparison with the experiments.

2.2 Experimental Setting

Moiré superlattices in two-dimensional (2D) materials have so far been primarily realized by twisting adjacent layers, leading to a wealth of emergent correlated phenomena such as flat-band superconductivity [44], magnetism [45,46], Mott–Hubbard states [47], and spatially modulated non-collinear spin textures [48–52]. However, the physical properties of these moiré van der Waals (vdW) structures depend sensitively on the twist angle, which is fixed during assembly and difficult to control *in situ*. Achieving uniform twist angles over large areas and ensuring reproducibility remain major experimental challenges [53, 54].

To overcome these limitations, differential strain between adjacent layers has emerged as a promising alternative route to generate moiré-like superlattices [43,55]. By imposing controlled strain gradients perpendicular to the layers, neighboring atomic planes acquire slightly different lattice constants, giving rise to a periodic modulation analogous to the moiré pattern in twisted heterostructures of transition-metal dichalcogenides [34, 56] (Figure 2.1b,c). Crucially, strain-induced moiré patterns offer a key advantage: their periodicity can, in principle, be tuned continuously by varying the applied strain, enabling dynamic control unattainable in twist-based

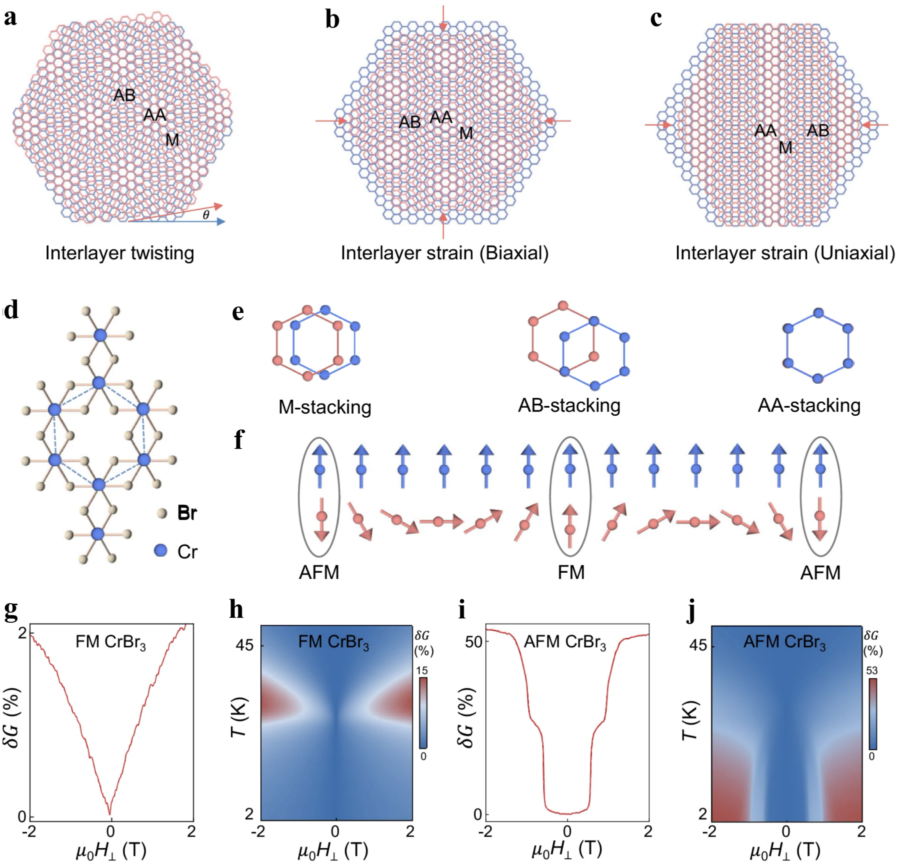

Figure 2.1: Moiré superlattices may arise from a small twist angle θ (**a**) and also from interlayer biaxial (**b**) and uniaxial (**c**) differential strain. **d**, Top view of the lattice structure of monolayer $\mathrm{CrBr_3}$. **e**, Depending on how layers are stacked, three distinct (meta)stable structures of $\mathrm{CrBr_3}$ are known: the M (monoclinic) and AA stackings lead to antiferromagnetic (AFM) interlayer coupling; the rhombohedral (AB) stacking leads to interlayer ferromagnetic (FM) ordering. **f**, The spatial dependence of the interlayer exchange spontaneously results in the formation of non-collinear spin textures. **g**, the tunneling magnetoconductance $\delta G(H, 2\text{ K})$ of FM barriers (data measured on a four-layer AB stacked $\mathrm{CrBr_3}$ junction) is small (2%) at low temperature and exhibits characteristic "lobes" near T_c as shown in **h**. In contrast, AFM barriers (data measured on a four-layer M stacked $\mathrm{CrBr_3}$ junction) exhibit a large low-T magnetoconductance (**i**) due to the spin-flip transitions of the inner and outer layers, which is suppressed as T is increased, and which vanishes above T_c (**j**). *Figure adapted from [1] under the Creative Commons BY 4.0 license. To view a copy of this license, visit https://creativecommons.org/licenses/by/4.0/.*

systems. Despite this potential, experimental realizations of strain-engineered moiré structures in vdW materials—and the exploration of their associated emergent phenomena—are still lacking.

In this section, I show that differential strain gives rise to moiré magnetism [48–52, 57–65] in multilayers of an originally ferromagnetic system, resulting in the coexistence of ferromagnetic and antiferromagnetic regions. The experiments rely on tunneling magnetotransport measurements through $CrBr_3$ barriers sandwiched between a Fe_3GeTe_2 metallic ferromagnetic electrode and a graphene contact. The magnetoconductance of such devices shows that the expected spin-valve effect –determined by the relative orientation of the magnetization in the Fe_3GeTe_2 electrode and the $CrBr_3$ barriers– coexists with an unexpected, reproducible background. This feature is confirmed to be moiré-related by performing the same experiment on a twisted stack of $CrBr_3$ barriers contacted with only graphene electrodes.

2.2.1 Detecting Moiré Magnetism with Magnetotransport

A single $CrBr_3$ layer (see Figure 2.1d) is ferromagnetic with out-of-plane magnetic order, and Curie temperature near 30 K [66,67]. A multilayer $CrBr_3$ has three known (meta)stable structures [31, 68], with the coupling between adjacent $CrBr_3$ layers being either ferromagnetic –for rhombohedral (AB) stacking– or antiferromagnetic –for AA or Monoclinic (M) stacking (see Figure 2.1e).

Tunneling occurs in the Fowler-Nordheim regime and the magnetoconductance varies with the alignment of the spins between layers in the $CrBr_3$ barrier, with increasing spin alignment that lowers the barrier height [68–70]. Accordingly, in ferromagnetic $CrBr_3$ barriers the magnetoconductance is small at low T (Figure 2.1g) –because the spins already align spontaneously in the absence of an applied field $\mu_0 H$ – and peaks near the Curie temperature (Figure 2.1h). In the antiferromagnetic phases of $CrBr_3$, instead, the low-T magnetoconductance is large (see Figure 2.1i,j), because the applied field flips the magnetization of individual layers and drastically improves spin alignment [70–75]. In both cases, the total magnetization of the barrier is the primal contributor to the magnetoconductance, i.e. $\delta G\big(H,T\big) = \delta G\big(M(H,T)\big)$ [70].

We observe a qualitative change of the magnetoconductance when one of the graphene electrodes is substituted with a FGT multilayer [76] (Figure 2.2a,b). When electrons are injected from FGT (Figure 2.2d), hysteresis appears and the barrier conductance is smaller when the magnetization directions in $CrBr_3$ and FGT are antiparallel (Figure 2.2f). The phenomenon is the expected spin-valve effect [77], as the $CrBr_3$ barrier spin-filters the spin-polarized electrons injected from the ferromagnetic contact [78]. Unexpectedly, however, the hysteretic contribution is superimposed onto a positive magnetoconductance background absent in devices with only graphene contacts. The background δG_{bg}, shown in the bottom panel of Figure 2.2f, resembles the magnetoconductance of antiferromagnetic $CrBr_3$ barriers: it

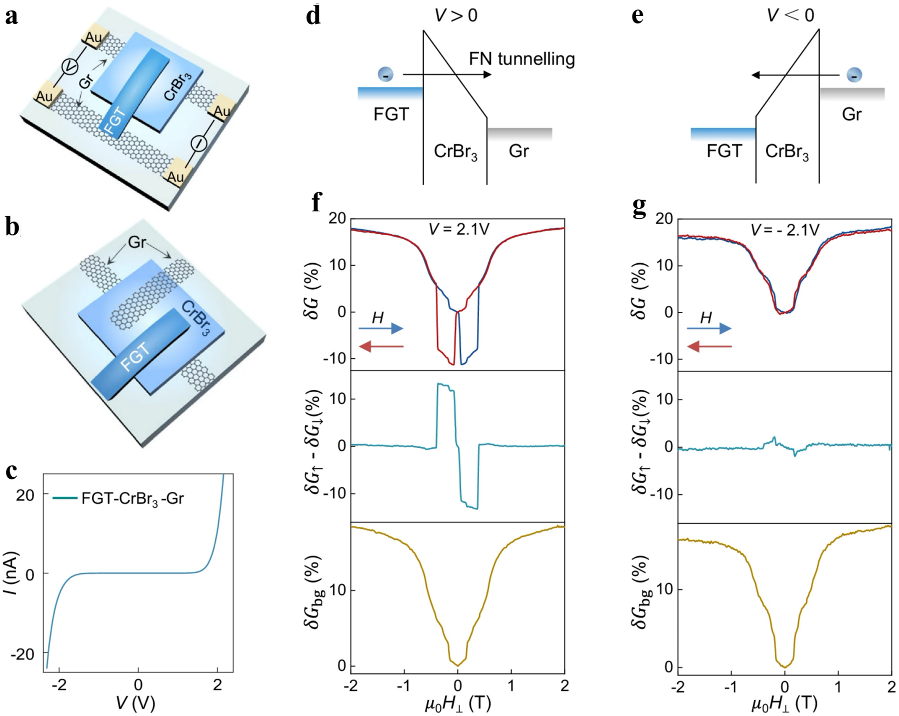

Figure 2.2: **a**, Schematic structure of a FGT/CrBr$_3$/Gr tunnel barrier device. **b**, Schematic view of a device consisting of a FGT/CrBr$_3$/Gr and a Gr/CrBr$_3$/Gr tunnel barriers realized on a same CrBr$_3$ multilayer. **c**, example of current-voltage (I-V) characteristics (data measured at $T = 2$ K). **d**,**e**, For positive and negative bias, electrons injected from the FGT or the Gr electrode respectively, tunnel through the CrBr$_3$ barrier (~ 8.5 nm), with transport occurring in the Fowler-Nordheim (FN) regime. **f**, Tunneling magnetoconductance for electrons injected from the FGT contact (top panel). The hysteresis is a manifestation of the spin-valve effect. The spin-valve magnetoconductance ($\delta G_\uparrow - \delta G_\downarrow$, middle panel) is superimposed on a sizable magnetoconductance background ($\delta G_{\rm bg} = \big((\delta G_\uparrow + \delta G_\downarrow) + (|\delta G_\uparrow - \delta G_\downarrow|)\big)/2$, bottom panel). **g**, Tunneling magnetoconductance measured with electrons injected from the graphene electrode (top panel). The spin valve effect (middle panel) is absent but the background magnetoconductance (bottom panel) is virtually identical to that measured when injecting electrons from the FGT contact. *Figure adapted from [1] under the Creative Commons BY 4.0 license. To view a copy of this license, visit https://creativecommons.org/licenses/by/4.0/.*

occurs on comparable magnetic field scales, has smaller but comparable magnitude, and an identical temperature dependence, albeit without equally sharp jumps. When electrons are injected from the graphene electrode (Figure 2.2e), hysteresis is nearly absent, but the magnetoconductance background remains unchanged (Figure 2.2g). We studied experimentally four FGT/$CrBr_3$/Gr junctions, all showing the same qualitative features.

We understand the lack of hysteresis in the Gr-injected electrons due to the resistance being dominated by the injection process in the Fowler-Nordheim regime. The finding that the background magnetoconductance is the same irrespective of the injecting electrode indicates that the phenomenon does not originate from injection at either contact, but is a manifestation of a property of the $CrBr_3$ barrier itself, which is modified by the presence of the FGT electrode.

We confirm that the background magnetoconductance only occurs in the presence of FGT electrodes by observing the same behavior in a pair of tunnel junctions fabricated on the *same* $CrBr_3$ multilayer. In one of the junctions, the $CrBr_3$ barrier is sandwiched between two graphene contacts, and in the other junction, one of the electrodes is an FGT crystal (see Figure 2.2b).

These observations establish that whenever FGT contacts are used, the magnetoconductance systematically exhibits a magnetic field and temperature dependent background that is indicative of the presence of antiferromagnetism, even if a purely ferromagnetic pristine $CrBr_3$ multilayer is employed to realize the tunnel barrier. We therefore conclude that bringing a $CrBr_3$ ferromagnetic multilayer into contact with a FGT electrode induces antiferromagnetism in $CrBr_3$. Ferro and antiferromagnetic regions are then simultaneously present, as expected in the presence of a moiré, and such coexistence can account for all the different aspects of the measured magnetoconductance.

2.3 Theoretical Model

Modeling quantum transport in magnetic tunnel junctions is a notoriously challenging task, particularly when one seeks quantitative agreement with experiments. In the case of $CrBr_3$ barriers, a positive tunneling magnetoconductance arises from the reduction of the effective barrier height when the spins within the barrier are aligned. This implies a direct link between the magnetoconductance and the overall magnetization of the $CrBr_3$ multilayer.

For ferromagnetically ordered $CrBr_3$ barriers — such as those aligned with AB stacking — it has been demonstrated that the tunneling magnetoconductance scales approximately quadratically with the magnetization [70], following the relation

$$\delta G \sim \delta M^2$$

This motivates the expectation that even in the presence of strain-induced moiré patterns, where local stacking configurations vary across the sample, the global magnetoconductance should remain strongly correlated with the net magnetization of the barrier.

Unlike transport properties, which require complex modeling of tunneling processes and electronic structure, the magnetization of a layered spin system can be addressed more directly, both analytically and numerically. For this reason, our approach begins with the construction of a spin model for strained $\mathrm{CrBr_3}$ multilayers under an applied magnetic field. By computing the magnetization across a range of field strengths, we establish a quantitative connection between the predicted magnetic response and the experimentally observed magnetoconductance.

This section follows closely the supplementary information of [1], with some additional details.

2.3.1 Spin Hamiltonian

We model the single layers of $\mathrm{CrBr_3}$ as featuring Heisenberg interactions (with negligibly small anisotropy) and a non-negligible single-ion easy-axis (out-of-plane) anisotropy [79]. Using the Pauli spin operators $\boldsymbol{S}_i$, for layer l this reads

$$\mathcal{H}_l = \frac{1}{2}\sum_n \sum_{\boldsymbol{\delta}} \tilde{J}_{\boldsymbol{\delta}} \boldsymbol{S}_l(\boldsymbol{x}_n) \cdot \boldsymbol{S}_l(\boldsymbol{x}_n + \boldsymbol{\delta}) - \tilde{h}\sum_n S_l^z(\boldsymbol{x}_n) - \tilde{d}\sum_n \left(S_l^z(\boldsymbol{x}_n)\right)^2$$

where $J_{\boldsymbol{\delta}}$ is the Heisenberg exchange between two sites connected by a lattice vector $\boldsymbol{\delta}$, $\boldsymbol{x}_n$ is the position of lattice site n, $\tilde{h}$ is an external out-of-plane magnetic field parameter, and $\tilde{d}$ is the anisotropy. Strain between adjacent layers is expected to lead to a moiré pattern, meaning that different stacking configurations will be present at once in the moiré unit cell. The stacking-dependence of interlayer Heisenberg exchange [31] is the reason we expect to find the coexistence of FM and AFM interactions between layers. This motivates us to consider the interlayer Hamiltonian

$$\mathcal{H}_{l,\perp} = \sum_n \tilde{J}_\perp(\boldsymbol{x}_n) \boldsymbol{S}_l(\boldsymbol{x}_n) \cdot \boldsymbol{S}_{l+1}(\boldsymbol{x}'_n)$$

where $\boldsymbol{x}'_n$ is the position of the lattice site in layer $l+1$ that is closest to $\boldsymbol{x}_n$. The total Hamiltonian for L layers is then

$$\mathcal{H} = \sum_l^L \mathcal{H}_l + \sum_l^{L-1} \mathcal{H}_{l,\perp} \tag{2.1}$$

The next step is taking the continuum limit of (2.1). This is motivated by the observation that magnetic properties will be defined on the moiré scale, which in any realistic straining situation is much larger then the atomic scale. We therefore substitute

$$\begin{aligned}\sum_n f(\boldsymbol{x}_n) \quad &\longrightarrow \quad 2V_u^{-1}\int d^2x f(\boldsymbol{x}) \\ \boldsymbol{S}_l(\boldsymbol{x}_n) \quad &\longrightarrow \quad S\boldsymbol{m}_l(\boldsymbol{x})\end{aligned}$$

and expand the Heisenberg exchange term in powers of $\boldsymbol{\delta}$. Here, V_u is the unit cell area, $S = \frac{3}{2}$ is the total on-site spin, $\boldsymbol{m}$ is the magnetization unit vector, and the factor 2 accounts for the presence of two spins per unit cell in hexagonal CrBr$_3$. Finally, we can write down the Hamiltonian density of a two-layer system as

$$\mathscr{H}(\boldsymbol{x}) = \sum_l^2 \frac{\rho^{ab}}{2}\left(\frac{\partial \boldsymbol{m}_l}{\partial x_a}\right)\cdot\left(\frac{\partial \boldsymbol{m}_l}{\partial x_b}\right) - d\left(m_l^z\right)^2 - hm_l^z + J_\perp(\boldsymbol{x})\boldsymbol{m}_1\cdot\boldsymbol{m}_2$$

where $\rho^{ab} = -S^2V_u^{-1}\sum_{\boldsymbol{\delta}}\tilde{J}_{\boldsymbol{\delta}}\delta^a\delta^b$ is the spin stiffness tensor, $d = 2\tilde{d}S^2V_u^{-1}$, $J_\perp = 2\tilde{J}_\perp S^2V_u^{-1}$ and $h = 2\tilde{h}SV_u^{-1}$. In a honeycomb lattice, the spin stiffness tensor is diagonal.

At this point, one of the key observations we can make is that if any non-collinear texture exists due to a sufficiently strong interlayer coupling $J_\perp$, then the magnetization will be *coplanar*. In fact, non-coplanar features, like skyrmions, will have a much larger energy cost. Since we consider only coplanar orders, we parametrize the magnetization by a position-dependent angle for each layer as $\boldsymbol{m}_l(\boldsymbol{x}) = \hat{\boldsymbol{x}}\sin\varphi_l(\boldsymbol{x}) + \hat{\boldsymbol{z}}\cos\varphi_l(\boldsymbol{x})$, and write the Hamiltonian density as

$$\begin{aligned}\mathscr{H}(\boldsymbol{x}) =& \frac{\rho}{2}\left[(\nabla\varphi_1)^2 + (\nabla\varphi_2)^2\right] + J_\perp(\boldsymbol{x})\cos(\varphi_1-\varphi_2) \\ &- d\left(\cos^2\varphi_1 + \cos^2\varphi_2\right) - h\left(\cos\varphi_1 + \cos\varphi_2\right)\end{aligned} \tag{2.2}$$

The energy minima must satisfy the Euler-Lagrange equations

$$\begin{cases}\rho\nabla^2\varphi_1 = d\sin 2\varphi_1 + h\sin\varphi_1 - J_\perp(\boldsymbol{x})\sin(\varphi_1-\varphi_2) \\ \rho\nabla^2\varphi_2 = d\sin 2\varphi_2 + h\sin\varphi_2 + J_\perp(\boldsymbol{x})\sin(\varphi_1-\varphi_2)\end{cases} \tag{2.3}$$

Alternatively, the Hamiltonian density and the corresponding Euler-Lagrange equations can be written in terms of the (anti-)symmetric polar angles $\varphi_s = \varphi_1 + \varphi_2$ and $\varphi_a = \varphi_1 - \varphi_2$ like

$$\mathscr{H}(\boldsymbol{x}) = \frac{\rho}{4}\left((\nabla\varphi_s)^2 + (\nabla\varphi_a)^2\right) + \cos\varphi_a\big(J_\perp(\boldsymbol{x}) - d\cos\varphi_s\big) - 2h\cos\frac{\varphi_s}{2}\cos\frac{\varphi_a}{2}$$

$$\begin{cases}\frac{\rho}{2}\nabla^2\varphi_s = d\cos\varphi_a\sin\varphi_s + h\cos\frac{\varphi_a}{2}\sin\frac{\varphi_s}{2} \\ \frac{\rho}{2}\nabla^2\varphi_a = -\sin\varphi_a\big(J_\perp(\boldsymbol{x}) - d\cos\varphi_s\big) + h\sin\frac{\varphi_a}{2}\cos\frac{\varphi_s}{2}\end{cases}$$

which is used by Ref. [58] and is, in general, more suited for analytical treatment.

	Source	$\tilde{J}_{\text{NN}}$	$\tilde{J}_\perp$ (AA)	$\tilde{d}$
First-principle calculations	Cai [80]	1.36	-	0.04
	Akram [62]	3.42	-	0.03
	Tong [57]	1.5	-	0.026 (exp.)
	Gibertini [31]	-	0.62	-
	Sun [81]	0.77-0.98	-	0.012
	Singh [79]	1.9	-	0.08
Experimental fitting	Fumega (+DFT) [82]	2.5	0.5	-
	Nikitin [83]	1.485	-	0.028
	Cai [80]	1.48	-	0.02

Table 2.1: Comparison of ferromagnetic nearest-neighbor Heisenberg exchange $\tilde{J}_{\text{NN}}$, interlayer coupling at AA stacking $\tilde{J}_\perp$ and single-ion easy-axis anisotropy $\tilde{d}$ from different sources in the literature. All values are in meV.

2.3.2 Physical Parameters

The parameters used in our theoretical spin model have been studied experimentally and numerically in the past. Table 2.1 summarizes some of the results obtained from experiments and first principle simulations. As Table 2.1 suggests, however, there is no agreement on the precise values for the magnetic parameters in CrBr_3, but they do provide an estimate for the order of magnitude of the parameters.

To estimate the interlayer coupling, we combine the ab initio results of Ref. [31] with experimental results on CrBr_3 multilayers. Ref. [68] studied the response of different antiferromagnetic stackings to an applied in- and out-of-plane magnetic field. In particular, there is a critical orthogonal field at which two neighboring layers align, which is $0.55\,\text{T}$ for the M metastable stacking and $0.2\,\text{T}$ for the AA metastable stacking. These critical spin-flip fields are directly proportional to the interlayer antiferromagnetic Heisenberg coupling strength. For this reason, we rescale the ab initio interlayer Heisenberg coupling to have the correct ratio of $\tilde{J}_\perp$ in the M'- and AA-stacked regions. In the rescaling process, we preserve the maximum and minimum values of the original data. The result is presented in Figure 2.3. In particular, we notice that the interlayer Heisenberg coupling at and near the AA antiferromagnetic region has a reduced magnitude after the rescaling.

Localized Moiré Interface

In the modeling of this system, we argue that the CrBr_3 multilayer experiences differential strain due to its coupling to the Fe_3GeTe_2 electrode. The strong metallic coupling of Fe_3GeTe_2 to CrBr_3 ensures that the top layer of CrBr_3 experiences a nonzero strain $\epsilon^{(1)}$. The question is how and whether this strain will propagate through the other layers, each of which can be characterized by a strain parameter $\epsilon^{(\ell)}$.

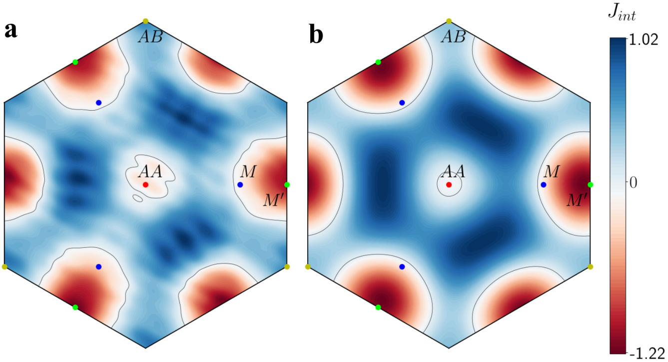

Figure 2.3: **a**, Interlayer exchange interaction calculated from first principles [31] and **b** rescaled interlayer interaction to be consistent with the relative switch fields in AA and M stackings. High symmetry points are highlighted: AB, AA, M and M'. *Figure adapted from [1] under the Creative Commons BY 4.0 license. To view a copy of this license, visit https://creativecommons.org/licenses/by/4.0/.*

In the simplest approximation, there are now three energy contributions that affect the strain propagation:

- The **in-plane strain energy** increases quadratically with the effective strain of each layer ℓ, giving $U \sim \sum_\ell (\epsilon^{(\ell)})^2$. This energy therefore favors as few layers as possible to have nonzero strain.

- The **stacking energy** between adjacent layers is minimized for perfect AB stacking. However, when two adjacent layers have different strain, $\epsilon^{(\ell)} \neq \epsilon^{(\ell+1)}$, a large-scale moiré structure arises with locally different stacking. The stacking energy is therefore minimized when neighboring layers have the same strain.

- The **magnetic energy** is minimized when the interlayer coupling is ferromagnetic. Any non-collinear texture, inevitable in the presence of a moiré interface, costs energy.

These three contributions together imply, without having to calculate the precise balance, that the total energy is minimized by having a *single moiré interface* where the $CrBr_3$ in-plane lattice constant goes from the Fe_3GeTe_2-mandated value to the relaxed monolayer value (Figure 2.4b). Where precisely this interface occurs in the multilayer depends on the interplay between the magnetic energy, the in-plane strain energy and the possible effect of lattice relaxation. The experimental evidence that ferromagnetism and antiferromagnetism coexist in the $CrBr_3$ multilayer further supports the notion that a moiré interface appears. We conclude that we can model the magnetic texture of the multilayer through the simple bilayer model presented in the previous section.

Let us also mention that since all layers on each side of the moiré interface have the same magnetic texture, the effective spin stiffness at the interface increases with the multilayer thickness.

Magnitude of Strain

Since both Fe_3GeTe_2 and $CrBr_3$ have hexagonal unit cells with a lattice constant ratio between 1.5 and 1.6, we expect that a strong binding between Fe_3GeTe_2 and $CrBr_3$ will force the more elastic layer ($CrBr_3$) to strain in order to achieve some commensurability. Depending on the angle at which Fe_3GeTe_2 and $CrBr_3$ make contact, the strain required to achieve commensurability can vary a lot and it can be different along the two lattice vectors. Based on a simple geometric matching of the lattice constants with varying twist angles, we find that realistic strains of the top $CrBr_3$ layer can vary between approximately 0.3% and 3%. In our simulations we take into consideration the possibility of having either *biaxial* or *uniaxial* strain, to cover all possibilities.

2.3.3 Magnetic Orders and Transitions

In the absence of a magnetic field, a perturbative analytical solution for the bilayer system can be found in Ref. [58] in the case when $\int_{\text{moiré}} d^2x J_\perp(\boldsymbol{x}) = 0$. Depending on the strain, spin stiffness, and anisotropy, they find three classes of ground states:

- **Collinear** (*c*) – All spins in the two layers are oriented out-of-plane. Characterized by strong anisotropy.
- **Twisted-s** (*tw-s*) – $\varphi_s = 0/\pi$ and φ_a follows the interlayer coupling. Characterized by weak anisotropy.
- **Twisted-a** (*tw-a*) – One layer is pinned $\varphi_1 = 0$ and the other aligns parallel or anti-parallel, depending on the local value of $J_\perp$. Characterized by strong interlayer coupling.

In the case of $CrBr_3$, regardless of the precise values, the interlayer Heisenberg coupling is always at least one order of magnitude larger than the anisotropy. This leads us to believe that at realistic strains, which produce very large moiré unit cells, the ground state magnetization is in a *tw-a* phase. The transitions from *tw-a* to *c* and from *tw-a* to *tw-s* have a jump in the magnetization and resemble a spin flip and a spin flop transition, respectively (see Figure 2.4a, c). The transition from *tw-s* to *c* instead is continuous in the magnetization. We expect that by applying a magnetic field one can drive these transitions.

In the presence of a magnetic field, the model becomes impossible to solve analytically. Intuitively, we expect that in the *tw-a* phase, applying a magnetic field will

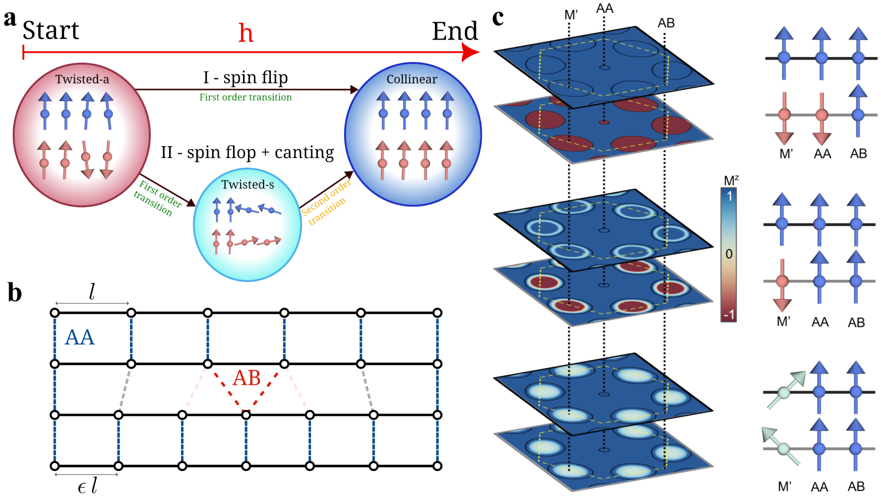

Figure 2.4: **a**, Passing from the twisted-a to the collinear spin configuration, there can either be a spin flip of an intermediate spin flop, followed by canting of the spins. **b**, Cartoon of strain localized at one interface of a multilayer with two different lattice constants. **c**. Transition in hexagonal bilayer following path II (**a**) showed on the rescaled interlayer coupling. *Panel **c** adapted from [1] under the Creative Commons BY 4.0 license. To view a copy of this license, visit https://creativecommons.org/licenses/by/4.0/.*

move the domain wall; in the *tw-s* phase, we expect the magnetic field to cant all spins towards the direction of the field, thus, also moving the domain wall.

An antiferromagnetic dome, starting in the *tw-a* phase, shrinks upon application of an out-of-plane magnetic field. There are two possible paths that the system can then take (Figure 2.4a):

I. A sharp transition to a *c* phase.

II. A sharp transition to a *tw-s*, phase, which then continuously transforms into a *c* phase at larger fields.

Whether or not the system passes through the *tw-s* phase depends on the spin stiffness and anisotropy, as well as the shape and magnitude of the interlayer coupling at the dome (e.g. if the interlayer coupling potential varies very smoothly, the *tw-a* domain wall might shrink all the way to a single spin before flipping and never transitioning to a *tw-s* phase). This also means that the domes, corresponding to local AA and M stacking, may have different transitions once a magnetic field is applied. A numerical solution is required to find out what exactly happens to the magnetization in a $CrBr_3$ strained bilayer.

2.3.4 Numerical Methods

We solve the model numerically with a gradient descent routine. We define the spins of one moiré unit cell on a grid of linear size L. To compute the energy (2.2), we need to evaluate the gradient of the phases (polar angles) $\varphi_{1/2}$, and to compute the functional derivatives of the Euler-Lagrange equations (2.3), we need to evaluate the Laplacian. Since the phases are defined on a grid, we compute these quantities with a central finite difference using the appropriate coefficients up 8th order of accuracy. The parameters are reported in Table 2.2. Since the phases are stored in a matrix with the two dimensions representing the two lattice directions, the finite-size derivatives are computed along these vectors, so a coordinate transformation is needed to compute derivatives and Laplacians.

position	-4	-3	-2	-1	0	1	2	3	4
f'	1/280	-4/105	1/5	-4/5	0	4/5	-1/5	4/105	-1/280
f''	-1/560	8/315	-1/5	8/5	-205/72	8/5	-1/5	8/315	-1/560

Table 2.2: Coefficients for central differences at 8th order.

The initial condition of the minimization is taken to be a constant phase in the two layers. We consider many initial conditions with different phases to avoid getting stuck in local minima. At each step, we compute the functional derivative of the Hamiltonian $d\mathscr{H}$ (see eq. (2.3)) and evaluate the energy of the new state $E(\varphi_1 + \eta d\mathscr{H}_1, \varphi_2 + \eta d\mathscr{H}_2)$ for a range of η and keep the one yielding the lowest energy. We update the phases and iterate this step until the energy converges to a stable value.

The finite-size nature of the derivatives makes it such that the shorter the distance between points in the grid, the better it approximates the continuum. In the results reported here, we use a 300×300 grid for biaxial strain and 500×3 for uniaxial strain in the a_1 direction.

We considered two types of strain in this work: *biaxial strain*, which corresponds to the case of two superimposed honeycomb lattices with different lattice lengths (see Figure 2.1b) and *uniaxial strain* along the a_1 direction, which yields an effective 1-D moiré unit cell (see Figure 2.1c). We expect the features to be stable also for more general cases. This can be understood through an easy argument. When straining or rotating one lattice with respect to the other, we are creating a moiré pattern. This pattern always starts from an AA-kind of stacking and has to end with another AA-stacking. The relative displacement between the two lattices in between always follows the same pattern. This means that, in the end, the main differences for what regards the interlayer interaction are the relative orientation of the two moiré vectors and their length. This also implies that the actual mechanism leading to the moiré pattern is not relevant in our calculation, it could also be a combination of strain (uniaxial, biaxial, shear ecc..) and relative *rotation* of the two layers. The physical parameters entering in the Hamiltonian of our model are the intra-layer spin stiffness

ρ_1, anisotropy d and the strain ϵ determining the moiré size.

2.4 Results

To further confirm that the coexistence of ferromagnetism and antiferromagnetism measured in FGT/CrBr$_3$/Gr tunneling junction comes from moiré magnetism, we have compared the behavior of these devices to that of small-angle (less than 3°) twisted CrBr$_3$ barriers, similar to twisted CrI$_3$ bilayers in which moiré magnetism is established [48–51]. The twisted CrBr$_3$ multilayers are sandwiched between graphene contacts. In one device, the non-twisted region was also sandwiched by two graphene contacts (see Figure 2.5a) to confirm that the constituent CrBr$_3$ multilayers consist of rhombohedral ferromagnetic stacking. The results of the low-temperature magnetoconductance measurements of non-twisted and twisted regions are shown in Figure 2.5b and Figure 2.5c (dashed lines), respectively.

In all twisted multilayer devices, a positive magnetoconductance background nearly saturating at (or just below) $\mu_0 H_\perp = 1$ T is observed at $T = 2$ K, whose shape is very similar to the magnetoconductance background seen in FGT/CrBr$_3$/Gr devices (compare Figure 2.5c with Figure 2.2f,g bottom panels). To better compare the magnetoconductance curves of the four different FGT/CrBr$_3$/Gr barriers with that of the twisted CrBr$_3$ barriers, we normalized the data to the value of the magnetoconductance measured at $\mu_0 H_\perp = 1$ T and plotted all curves together (see Figure 2.5c). The differences in magnetoconductance between twisted CrBr$_3$ and FGT/CrBr$_3$/Gr devices is within the spread of the curves due to differences in twist angle or in strain orientation (i.e., the relative orientation of the crystalline structures of the FGT and CrBr$_3$ multilayers). Finding that the magnetoconductance of FGT/CrBr$_3$/Gr devices exhibits trends identical to those of devices based on twisted CrBr$_3$, whose magnetoconductance is due to moiré magnetism, confirms that, despite the absence of any twist, moiré magnetism is present FGT/CrBr$_3$/Gr devices.

Having concluded experimentally that the magnetoconductance measured in FGT-gated devices originates from differential strain in CrBr$_3$ induced by the contact with FGT, we take into account into our theoretical model the experimentally relevant parameters for this system. We find that a CrBr$_3$ moiré bilayer in the absence of a magnetic field has a magnetic texture with locally c-axis aligned ferromagnetic or antiferromagnetic order, separated by coplanar domain walls. Upon the application of a magnetic field these domain walls move, and the antiferromagnetic domains shrink, leading to smooth changes in magnetization that indeed mimic the observed smooth change in magnetoconductance (Figure 2.5d).

At a first critical field $H_\perp^{AA}$ –whose value depends on the strain pattern and effective spin stiffness– the antiferromagnetic domain around the AA region disappears through a spin-flip transition, causing a kink in the magnetization curve (Figure 2.6 from panel a to b, pink shaded region in Figure 2.5d). This is because dM/dH is determined by the shift of domain walls, and the removal of AFM domains changes

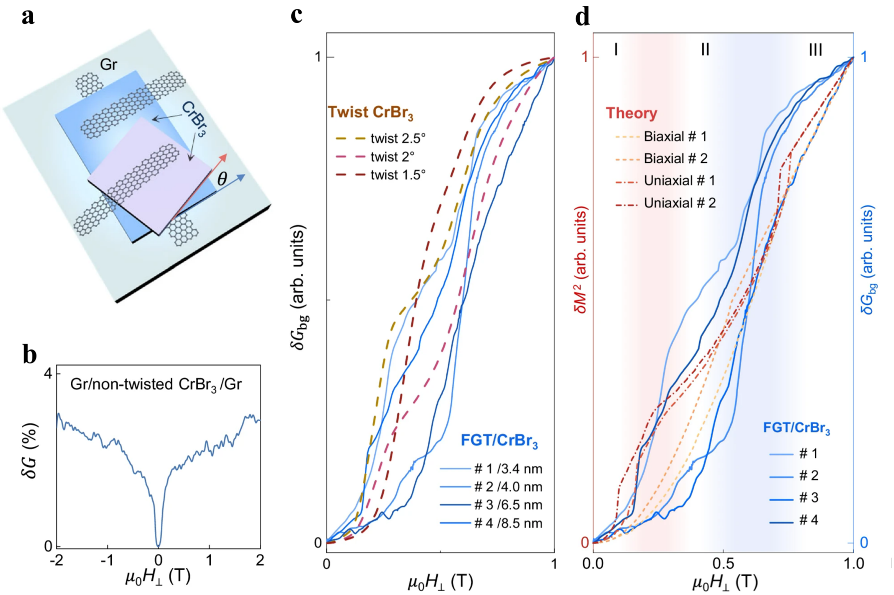

Figure 2.5: **a**, Schematic of the device configuration, showing a Gr/twisted-$CrBr_3$/Gr junction with a Gr/untwisted-$CrBr_3$/Gr tunnel barrier fabricated on the same $CrBr_3$ multilayer. **b**, Magnetoconductance of the Gr/untwisted-$CrBr_3$/Gr junction measured at $T = 2$ K, showing the behavior typical of ferromagnetic $CrBr_3$ barriers. **c**, Plot of the magnetoconductance background δG_{bg} of all the measured FGT/$CrBr_3$/Gr devices (continuous lines) compared to the magnetoconductance of the three twisted $CrBr_3$ devices (dashed lines). All curves are normalized to 1 at $\mu_0 H_\perp = 1$ T for ease of comparison. **d**, Plot of the magnetoconductance background δG_{bg} and of δM^2, as a function of H. Both δG_{bg} and δM^2 increase smoothly at first, up to the critical field for the spin-flip transition at the AA-stacked region at $\mu_0 H_\perp \sim 0.2$ T (pink shaded region). A second smooth increase then occurs with the antiferromagnetic domains near the M'-stacked region that are further reduced in size, up to a second critical field $\mu_0 H_\perp \sim 0.5 - 0.7$ T associated with a spin flop-transition (blues shaded region). The two theoretical curves for biaxial strain have 1% strain, spin stiffness is 1.4 meV, and anisotropy is 0.01 meV and 0.02 meV, respectively. The two curves with uniaxial strain have 1% and 3% strain, respectively, the spin stiffness is 10 meV, and anisotropy is 0.01 meV. *Figure adapted from [1] under the Creative Commons BY 4.0 license. To view a copy of this license, visit https://creativecommons.org/licenses/by/4.0/.*

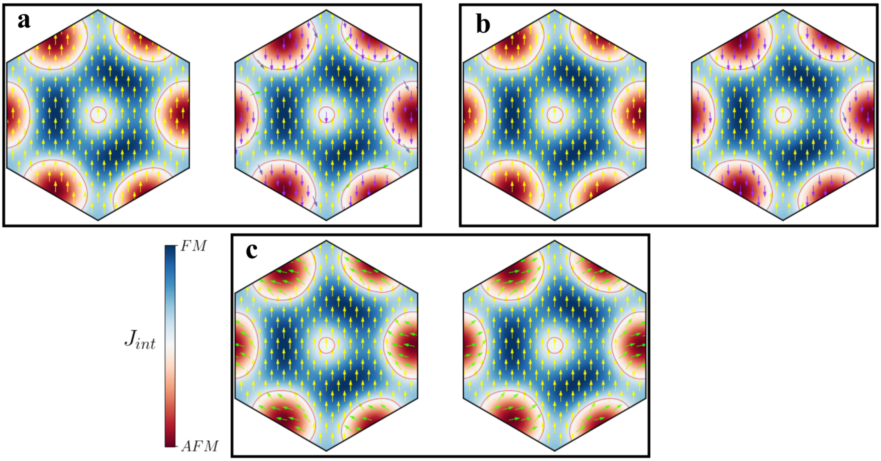

Figure 2.6: Spin texture in the two layers of our model for three prototypical cases. The little arrows describe the spin directions in the $x - z$ plane in a moiré unit cell where the background is the interlayer coupling of Figure 2.3. In **a** a typical *tw-a* phase, where all AFM regions are pointing in the z direction. In **b** a configuration after the spin-flip of the region AA. We can start to see here also the boundary between the FM and AFM regions close to the M stacking. Finally, in **c** we show the spin texture of a typical configuration after the spin-flop transition of the M' region. *Figure adapted from [1] under the Creative Commons BY 4.0 license. To view a copy of this license, visit https://creativecommons.org/licenses/by/4.0/.*

this slope. A second kink at higher fields $H_{\perp}^{M}$ (Figure 2.6 from panel b to c, blue shaded region in Figure 2.5d) is associated with a spin-flop at a field comparable to –but somewhat larger than– the spin-flip field seen in M-stacked bilayers. This is consistent with the ab initio prediction that the strongest antiferromagnetic interlayer coupling does not occur for the M-stacked structures, but for a different monoclinic stacking (M') that does not correspond to a (meta)stable M stacking of $CrBr_3$.

The features that we find are robust, in the sense that the two kinks appear regardless of the details such as the precise form of strain, stiffness, and spin anisotropy. The exact values of the spin flip and flop fields depend on details such as the thickness of the $CrBr_3$ multilayer and the induced differential strain, as explained in the next section. As shown in Figure 2.5d, a qualitative agreement between the experimentally measured magnetoconductance and the square of the magnetization is found for a realistic set of model parameters. We compare to the square of the magnetization since for ferromagnetic barriers the relation between magnetoconductance and magnetization is approximately quadratic [70].

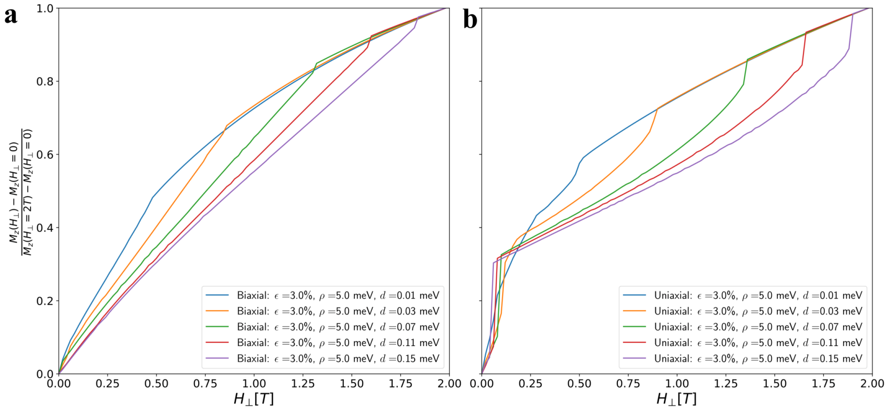

Figure 2.7: Magnetization curves as a function of magnetic field for biaxial (**a**) and uniaxial (**b**) strain. The curves are at a fixed strain (3%) and stiffness (5 meV), with varying anisotropy. Note that compared to Figure 2.5d, we are considering here a wider range of parameters, including the applied magnetic field up to 2 T. *Figure adapted from [1] under the Creative Commons BY 4.0 license. To view a copy of this license, visit https://creativecommons.org/licenses/by/4.0/.*

2.4.1 Stability of Solutions

We find that the features related to the spin flip-flop of the AA and M’ regions are very stable to the choice of physical parameters. We show this by exploring a large window of parameters for the stiffness, anisotropy and strain. For the stiffness we consider the values $\rho = 0.1, 1.4, 5, 10, 100\,\text{meV}$, for the anisotropy $d = 0.01$, 0.03, 0.0709, 0.11, 0.15 meV and finally, for the strain we consider $\epsilon = 5\%$, 4%, 3%, 2%, 1%, 0.5%. The magnetization curves as a function of the applied magnetic field show particular features when an antiferromagnetic region undergoes a transition. We can see a family of such curves in Figure 2.7 for biaxial and uniaxial strain. We can clearly see the features occurring at the flop transition of the M’ region. The feature at the AA region is less evident in the biaxial strain than in the uniaxial case, because the area occupied by this antiferromagnetic region is much less in the former case.

The choice of physical parameters determines the position in the magnetic field at which the mentioned features appear. We went on to extract the main features of the magnetization plots in order to determine the tendencies upon variation of the parameters of the Hamiltonian. We computed magnetization plots for a broad range of parameters and we extracted the fields at which features appear. The results are shown in Figures 2.8, 2.9, 2.10, and 2.11.

We can, first of all, appreciate how the difference in moiré periodicity becomes more and more important when increasing the spin stiffness. In particular, features

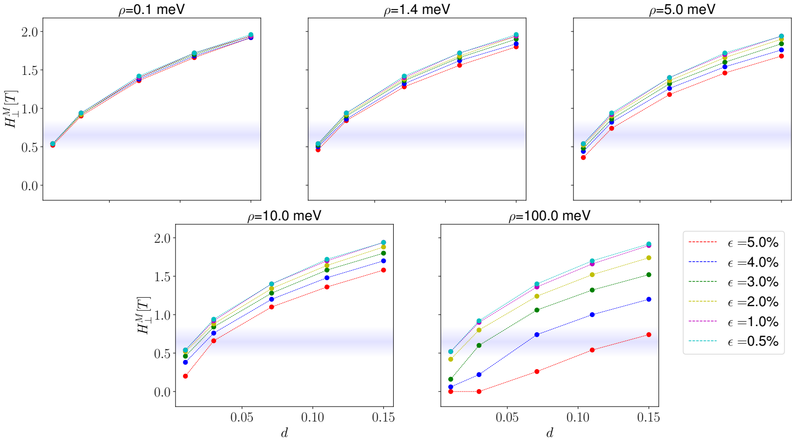

Figure 2.8: Transition field of M' region for different values of biaxial strain as a function of anisotropy. The blue shaded region refers to the range of applied magnetic fields where the spin flop transition in the M' region occurs in the experimental samples. *Figure adapted from [1] under the Creative Commons BY 4.0 license. To view a copy of this license, visit https://creativecommons.org/licenses/by/4.0/.*

appear at lower fields for smaller moiré unit cells. This occurs because there is a smaller region that needs to be flipped in order for the transition to happen.

From Figures 2.9 and 2.11, we can see that the dependence of the transition field at AA is less dependent on the anisotropy than the one at M'. In general, the transition field decreases with the stiffness and the anisotropy. Also the strain plays an important role, with features occurring at higher fields for smaller strain parameters, corresponding to big moiré unit cells.

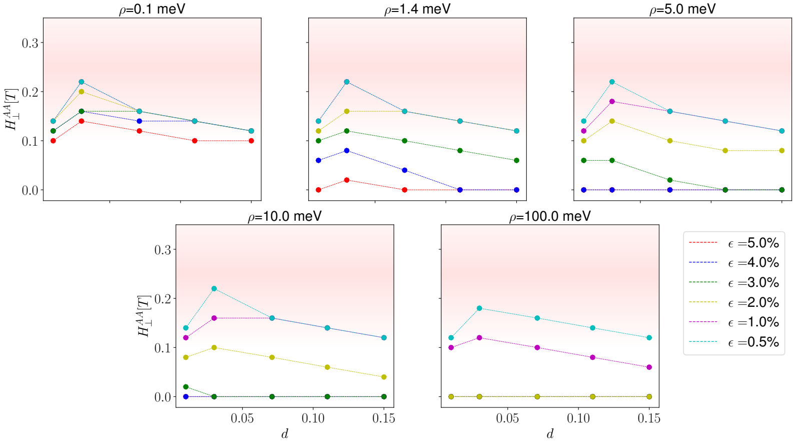

Figure 2.9: Transition field of AA region for different values of biaxial strain as a function of anisotropy. The red shaded region refers to the range of applied magnetic fields where the spin flip transition in the AA region occurs in the experimental samples. *Figure adapted from [1] under the Creative Commons BY 4.0 license. To view a copy of this license, visit https://creativecommons.org/licenses/by/4.0/.*

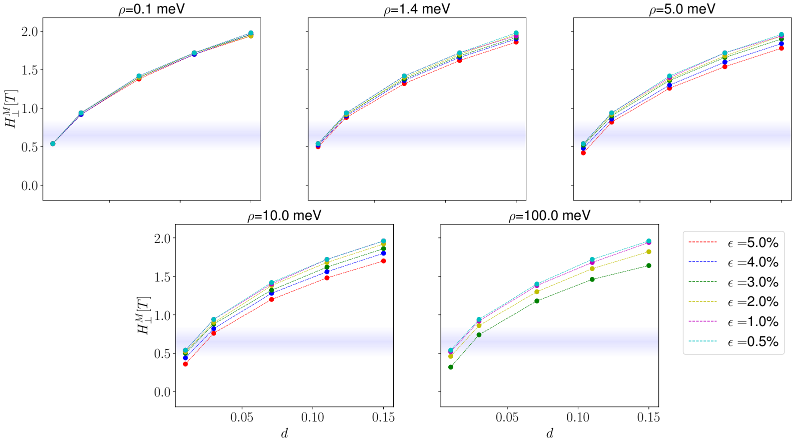

Figure 2.10: Transition field of M’ region for different values of uniaxial strain as a function of anisotropy. Here we considered no translation in the a_2 direction. The blue shaded region refers to the range of applied magnetic fields where the spin flop transition in the M’ region occurs in the experimental samples. *Figure adapted from [1] under the Creative Commons BY 4.0 license. To view a copy of this license, visit https://creativecommons.org/licenses/by/4.0/.*

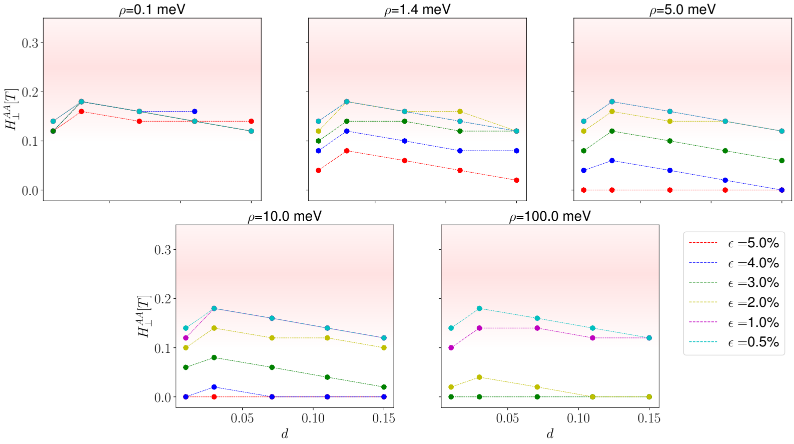

Figure 2.11: Transition field of AA region for different values of uniaxial strain as a function of anisotropy. Here we considered no translation in the a_2 direction. The red shaded region refers to the range of applied magnetic fields where the spin flip transition in the AA region occurs in the experimental samples. *Figure adapted from [1] under the Creative Commons BY 4.0 license. To view a copy of this license, visit https://creativecommons.org/licenses/by/4.0/.*

CHAPTER 3

Quantum Magnetism in a TMD Hetero-Bilayer

3.1 Introduction

One of the most important and spoken-of phases predicted by quantum magnetism are *quantum spin liquids*. Spin liquids are an exotic phase of matter which has been at the center of theoretical and experimental exploration because of its unique properties. The main concept at the core of the quantum spin liquid phase is its characteristic of having strong quantum fluctuations which destroy magnetic order down to zero temperature. Paramagnetic systems have the tendency to order at low temperature by developing a finite magnetization pattern, thus reducing the symmetry of the system, in a mechanism known as spontaneous symmetry breaking. Spin liquids instead remain disordered, feature long range quantum entanglement and often also topological properties like ground state degeneracy [11].

Spin liquids, being characterized by their lack of features, have proven to be extremely hard to observe in solid state systems. Theoretically, a fertile ground for the emergence of spin liquids is that of *frustrated* quantum magnets, where the usually huge degeneracy of classical ground states leads to strong quantum fluctuations. Another characteristic usually found in spin liquids is that of *fractionalization*: the spin degree of freedom can be decomposed into multiple components which turn out to be the excitations of the system, with the main example given by the exact solution of the Kitaev honeycomb model [9]. As will be explained in this chapter, the choice of decomposition can describe different types of spin liquid phases [84], being it *gapped*, *gapless* or even featuring time-reversal symmetry breaking, i.e. a *chiral* spin liquid [85, 86].

Moiré systems, in particular transition metal dichalcogenide (TMD) hetero-bilayers are very good candidates to study the emergence of spin liquids. In fact, they exhibit strong electronic interactions and feature many tuning knobs by which it is possible to alter these interactions: twist angle, choice of the material and dielectric environment. Experiments on TMD moiré systems have uncovered evidence of Mott insulating behavior [47, 87–90], the quantum anomalous Hall effect [91], and, in hetero-bilayer configurations, generalized Mott–Wigner crystalline states at fractional fillings [88, 92–96]. This latter case is particularly important for quantum magnetism, since when charge carriers become localized, only the spin degrees of freedom remain active, giving rise to magnetism. Theoretical descriptions of hetero-bilayers map naturally onto extended Hubbard models [97–100] on triangular lattices, where geometric frustration among localized spins can suppress conventional order.

In the following chapter I will describe the work carried out in Refs. [2] and [3] in which we identify a TMD hetero-bilayer (WSe_2/WS_2) as a possible candidate for the realization of a chiral spin liquid phase. In section 3.2 I describe the derivation of the Heisenberg model for the spin degree of freedom starting from the Hubbard model describing the moiré WSe_2/WS_2 hetero-bilayer [2]. While the motivation to study this model lies in the solid-state realization of a spin liquid phase, the main focus of the chapter will be on the Schwinger boson mean-field theory (SBMFT) I carried out to study the phase diagram of the $J_2 - J_3$ Heisenberg model on the kagome lattice with Dzyaloshinski-Moryia interactions [3]. In section 3.3 I first describe and then employ SBMFT to compute the phase diagram of the model. I also classify the classical magnetic orders and the different spin liquid phases allowed by symmetry through a projective symmetry group classification of mean-field ansätze. Finally, in section 3.4 I discuss the results of mean-field theory and compare them with the results of DMRG [2] on the same model to establish the features which are captured at the mean-field level and to draw conclusions on the ground state of this hetero-bilayer.

3.2 Derivation of the Spin Hamiltonian

Moiré systems of TMDs can be tuned in filling in order to realize various strongly correlated phases [92, 93]. In particular, when filling at $n = \pm 3/4$ a WSe_2/WS_2 hetero-bilayer, it has been shown that the electrons localize on an emergent kagome lattice. This is particularly interesting from the quantum magnetism perspective since the kagome lattice inherently exhibits strong geometric frustration.

To show this, we start from the description of flat bands in the moiré hetero-bilayer by a spin-orbit-coupled extended Hubbard model on the triangular lattice

$$\mathcal{H} = \sum_{jk,\sigma} |t_{jk}| \left[e^{-i\sigma\phi_{jk}} c^{\dagger}_{j\sigma} c_{k\sigma} + \text{H.c.} \right] + U \sum_{j} n_{j\uparrow} n_{j\downarrow} + V \sum_{\langle jk \rangle,\sigma} n_{j\sigma} n_{k\sigma}, \quad (3.1)$$

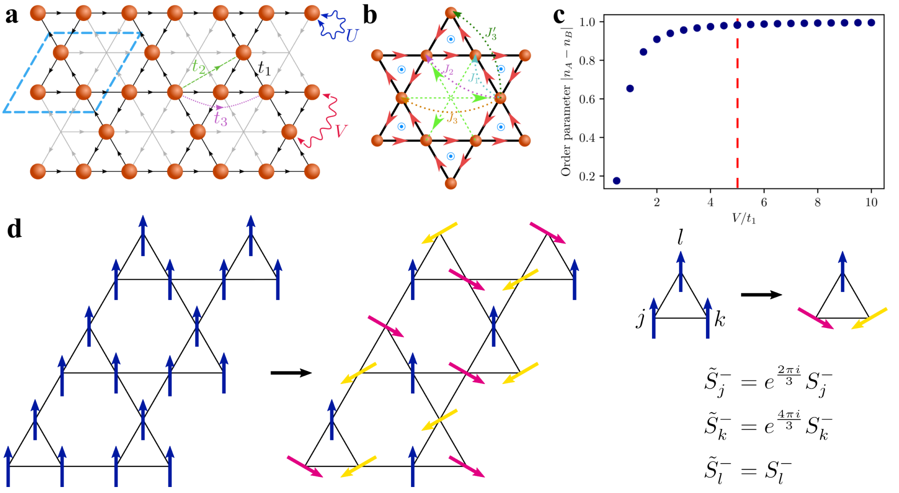

Figure 3.1: **a**, Extended Hubbard model at $n = 3/4$ filling with all charges localized on a kagome lattice. The unit cell of the charge ordering is indicated by the blue-lined box. When a spin-↑ particle hops from a site j to a site k along the direction of an arrow, it picks up a phase of ϕ_{jk}. **b**, Interactions of the Heisenberg model: curved arrows indicate the neighbor coupling exchange, red and green arrows show the direction of the DM interaction on each 1st and 3rd nearest neighbor bond. Blue circles indicate the sign of the DM vector. **c**, Kagome charge order parameter as a function of V/t_1 at zero temperature, based on mean-field theory. Unity means that all the charge is localized on the kagome lattice. **d**, Local spin rotation that restores $SU(2)$ invariance of the Hamiltonian by transforming away the DM interactions. The Hamiltonian written in terms of the $\tilde{S}$ operators contains only Heisenberg terms. As shown here, an in-plane ferromagnet (left) develops $\sqrt{3} \times \sqrt{3}$ order (middle) under this transformation. *Figure adapted from [2] under the Creative Commons BY 4.0 license. To view a copy of this license, visit https://creativecommons.org/licenses/by/4.0/.*

where $\langle jk \rangle$ denotes nearest-neighbor sites and σ the spin. We include the hopping matrix elements t_{jk} up to third-nearest neighbor, where ϕ_{jk} represent their phases induced by spin-orbit coupling. When the nearest-neighbor repulsion is sufficiently large, a charge density wave is stabilized at commensurate fillings. In particular, at $n = \pm 3/4$ filling, the charge order forms a *kagome* lattice (see Figure 3.1a). The simplest description of the kagome charge order amounts to a mean-field theory for spinless electrons with nearest neighbor hopping on a triangular lattice and nearest-neighbor repulsion $V \sum_{\langle ij \rangle} n_i n_j$. With the mean-field decoupling $n_i n_j \to -\langle n_i \rangle \langle n_j \rangle + n_i \langle n_j \rangle + \langle n_i \rangle n_j$ the resulting Hamiltonian is solved self-consistently for fixed particle filling $n = 3/4$. The $T = 0$ expectation value for the occupation difference between the kagome sites and the empty site is shown in Figure 3.1c. We also find within our mean-field theory that for $V/t > 0.4$ a full gap in the spectrum appears, with the charge excitation gap at large V scaling as $\Delta \approx 2V - t$. At $V/t = 5$ the charge on the occupied sites exceeds $n_A = 0.98$. We choose this as threshold for charge localization, and therefore as a limit on the applicability of our strong coupling expansion of the effective spin model.

We then derive the effective model describing the spin degree of freedom by a strong coupling expansion. We expand the extended Hubbard Hamiltonian (3.1) in the ratio of hoppings to interactions according to Ref. [101]. We keep all terms of second and third order in the hoppings, and all fourth order terms $\propto t_1^4$. Details of this calculation can be found in the supplementary material of [2]. The resulting spin model is an XXZ Heisenberg model with Dzyaloshinskii–Moriya interactions up to third nearest neighbor (Figure 3.1b)

$$\mathcal{H} = \sum_{\gamma} J_\gamma \sum_{\langle ij\rangle_\gamma} \Big(S_i^z S_j^z + \cos\big(2\phi_{ij}^\gamma\big)\left(S_i^x S_j^x + S_i^y S_j^y\right) + \sin\big(2\phi_{ij}^\gamma\big)\left[\hat{\mathbf{z}} \cdot \left(\boldsymbol{S}_i \times \boldsymbol{S}_j\right)\right]\Big) \tag{3.2}$$

where the summation over γ includes first, second and the two types of third nearest neighbor and $\langle i, j\rangle_\gamma$ denotes the γ-th nearest neighbor. In [2] we explored how these parameters emerge from the Hubbard hoppings t_1, t_2 and t_3 and computed their values for different twist angles. We showed that by using the twist angle and the dielectric screening as tuning knobs, one can tune the J_2-J_3 phase diagram of the model, with J_3' terms being negligible.

3.2.1 Dzyaloshinskii–Moriya Interaction

The spin model (3.2) contains XXZ and Dzyaloshinskii–Moriya (DM) terms caused by the nonzero phases ϕ_{jk} of the hoppings in the extended Hubbard model. These phases are constrained by symmetry [99] in TMD hetero-bilayers and translate into the phases for the spin model as $\tilde{\phi}_1 = 4\pi/3$, $\tilde{\phi}_2 = 0$, and $\tilde{\phi}_3 = 2\pi/3$ for nearest, next-nearest and next-next-nearest neighbor couplings, respectively. This combination of phases is special because it allows for a local three sublattice gauge transformation of the form showed in Figure 3.1d. It amounts to a sublattice-dependent spin rotation in the x-y plane, that brings the model into $SU(2)$-invariant form, hence, the model still exhibits a hidden $SU(2)$ symmetry [102–104]. This transformation is related to the invariance of the spectrum of the underlying Hubbard model under the introduction of 2π flux through a triangular plaquette.

In the following, we will consider the following more general regime which follows from the analysis of Ref. [102] motivated by homo-bilayers

$$\phi^2 = 0, \tag{3.3a}$$

$$\phi^3 = 2\phi^1. \tag{3.3b}$$

From now on let us define $\phi \doteq \phi^1$ which we will later tune to study the emerging J_1-J_2-J_3 phase diagram. The Hamiltonian term describing general DM interactions is usually written as

$$\mathcal{H}_{DM} \propto \boldsymbol{D}_{ij} \cdot (\boldsymbol{S}_i \times \boldsymbol{S}_j) \,. \tag{3.4}$$

In our case, the DM vector $\vec{D}_{ij}$ is pointing uniformly in the $\hat{z}$ direction. Its orientation is shown in Figure 3.1b. The red arrows indicate the direction over which to take the cross product of (3.4). We will refer to this kind of DM interaction as "uniform" DM interaction since all the DM vectors point in the same direction, as opposed to the "staggered" case which has been considered in many other works in the literature [105–108]. Our choice of the DM angles in (3.3) is such that at particular angles $\phi = n\pi/3$, the $SU(2)$ symmetry is restored. As mentioned above, such DM phases can be eliminated by a gauge transformation of the spins (a local spin rotation in the xy-plane) following a $\sqrt{3} \times \sqrt{3}$ type of pattern (explained in section 3.3.3). For this reason, we expect to see a periodicity in the phase diagram as a function of ϕ with period $2\pi/3$.

3.3 Heisenberg Model on the Kagome Lattice

The Heisenberg model on the kagome lattice has been the subject of extensive investigations due to its strong geometric frustration which makes it a prime candidate for the realization of a quantum spin liquid phase [6, 26, 109–116]. This interest is not only theoretical in nature, but various materials are believed to be approximately described by the model [109, 110]. The most intensely studied compound is Herbertsmithite ($\mathrm{ZnCu_3(OH)_6Cl_2}$) [117–121], but alternative material realizations have been investigated, and found not to exhibit any signs of ordering much below the temperature scales associated to the respective spin coupling [122–128].

On the theoretical side, the problem has a long history and has been approached with every conceivable method ranging from mean-field theory of partons [129–133], variational [124, 134–137] and renormalization techniques [138–140] to numerically exact algorithms [25, 26, 112, 113, 115, 141–149] and tensor networks [114, 150–152]. It is widely believed that the nearest-neighbor-only model hosts a spin liquid ground state, but its nature is under ongoing debate.

Early density matrix renormalization group (DMRG) studies pointed to a gapped ($\mathbb{Z}_2$) ground state [113, 146, 147], whereas variational Monte Carlo [136, 137, 153], more recent DMRG [115, 149] and two-dimensional tensor network studies [114, 152] favor a gapless $U(1)$ Dirac spin liquid instead. While the nearest-neighbor-only model has always been in the focus of attention, various perturbations to the system have been considered as well. Both longer range interactions [116, 154–159] and $SU(2)$ breaking Dzyaloshinskii–Moriya (DM) [105–107, 160–166] terms have been studied. With varying parameters, it has been shown that other states such as a chiral spin liquid (CSL) [85, 86, 167] and valence bond orders can be ground states or closely competing states [105, 133, 153, 155, 157–159, 168–170].

In this section, I present the study of the phase diagram of the antiferromagnetic

Heisenberg model on the kagome lattice with up to third-nearest neighbor and additional DM interactions by Schwinger boson mean-field theory (SBMFT), following the description given in [3]. We derive the projective symmetry group (PSG) classification of both time reversal (TR) symmetric and TR symmetry breaking chiral $\mathbb{Z}_2$ spin liquid ansätze on the kagome lattice for the given interactions. We use these ansätze and the classification of classical long-range magnetic orders to derive the phase diagram of the model.

3.3.1 Schwinger-Boson Mean-Field Theory

The main idea of SBMFT is to replace the spin operators $\mathbf{S}$ with boson operators a, b in a way that respects the $SU(2)$ symmetry of the model. This allows a mean-field theory treatment of both symmetric and symmetry broken phases. Concretely, the spin operators are substituted by Schwinger bosons (also called *spinons*) as

$$\boldsymbol{S}_i = \frac{1}{2}\begin{pmatrix} a_i^\dagger b_i^\dagger \end{pmatrix} \vec{\sigma} \begin{pmatrix} a_i \\ b_i \end{pmatrix}, \tag{3.5}$$

with $\vec{\sigma}$ Pauli matrices. This substitution enlarges effectively the Hilbert space of the model, meaning that in order to get physical solutions one has to impose the occupation constraint

$$a_i^\dagger a_i + b_i^\dagger b_i = 2S \tag{3.6}$$

on each site of the lattice. We already see from this constraint that the spin value S is a parameter entering our model as a tuning knob of quantum fluctuations. In fact, in SBMFT the spin S is a free parameter not necessarily restricted to $1/2$. A lower value produces more quantum fluctuations, while for $S \to \infty$, the classical limit is recovered. A value frequently used arises from fixing $\langle \mathbf{S}^2 \rangle = 3S(S+1)/2 = 3/4$, which leads to $S = (\sqrt{3}-1)/2 \approx 0.366$ [106, 171, 172]. In the following, we vary S to evoke transitions from long-range magnetic orders to quantum spin liquids.

Let us review the derivation of the mean-field Hamiltonian in order to explain the notation and highlight the key steps of the procedure. For a thorough explanation of SBMFT see Refs. [172, 173]. By substituting the Schwinger bosons into the Hamiltonian we obtain the familiar form

$$\mathcal{H} = \sum_\gamma J_\gamma \sum_{\langle ij \rangle_\gamma} \left(: B_{ij}^{\gamma\dagger} B_{ij}^\gamma : - A_{ij}^{\gamma\dagger} A_{ij}^\gamma \right) + \sum_i \lambda_i \left(a_i^\dagger a_i + b_i^\dagger b_i - 2S \right)$$

The double dots denote normal ordering and λ_i are the Lagrange multipliers enforcing the constraint (3.6). We introduced here the pairing A_{ij}^γ and hopping B_{ij}^γ operators defined as

$$A_{ij}^\gamma = \frac{1}{2}(\tau_{ij}^{\gamma*} a_i b_j - \tau_{ij}^\gamma a_j b_i), \tag{3.7a}$$

$$B_{ij}^\gamma = \frac{1}{2}(\tau_{ij}^\gamma a_i^\dagger a_j + \tau_{ij}^{\gamma*} b_i^\dagger b_j), \tag{3.7b}$$

where $(\tau_{ij}^{\gamma})^2 = e^{-i2\phi_{ij}^{\gamma}}$ carries the information of the DM phase. This decoupling is useful since it allows us to express the quartic Hamiltonian in terms of products of $U(1)$ invariant bond operators that explicitly preserve the rotational invariance of the interactions. In the Heisenberg case without DM interactions, these operators are $SU(2)$ invariant.

Up to this point we merely rewrote the original Hamiltonian and, if the single occupation constraint is strictly respected at each site, the two models are equivalent and will have exactly the same ground state. We note that the operators appearing in the Hamiltonian have changed from 2-spin operators to 4-boson operators. The next step is to implement the mean-field approximation, which in our case is

$$A_{ij}^{\gamma\dagger} A_{ij}^{\gamma} \simeq \mathcal{A}_{ij}^{\gamma *} A_{ij}^{\gamma} + A_{ij}^{\gamma\dagger} \mathcal{A}_{ij}^{\gamma} - |\mathcal{A}_{ij}^{\gamma}|^2,$$

where we use $\mathcal{A}_{ij} = \langle A_{ij} \rangle$ and $\mathcal{B}_{ij} = \langle B_{ij} \rangle$ to denote the expectation value of pair and hopping operators, respectively. We can now perform a Fourier transformation of the spinon operators

$$a_i = \frac{1}{\sqrt{\Omega}} \sum_{\boldsymbol{k} \in \mathrm{BZ}} e^{i\boldsymbol{k}\cdot\boldsymbol{x}_i} a_{\mu_i,\boldsymbol{k}}$$

where we split the site index i into the unit cell (UC) coordinates $\boldsymbol{x}_i$ and the index within the unit cell μ_i. Let us note here that the *lattice* unit cell in the kagome lattice contains three sites, but depending on the ansatz used in the minimization, we will use unit cells of three and six sites. We obtain the mean-field Hamiltonian

$$\begin{aligned} \frac{\mathcal{H}_{MF}}{N_s} =& \lambda\left(2S+1\right) + \sum_{\gamma} \frac{1}{2} z_{\gamma} J_{\gamma} \left(|\mathcal{A}_{ij}^{\gamma}|^2 - |\mathcal{B}_{ij}^{\gamma}|^2\right) \\ &+ \frac{\lambda}{\Omega m} \sum_{\boldsymbol{k}} \sum_{i \in UC} \left(a_{\mu_i,\boldsymbol{k}}^{\dagger} a_{\mu_i,\boldsymbol{k}} + b_{\mu_i,-\boldsymbol{k}} b_{\mu_i,-\boldsymbol{k}}^{\dagger} \right) \\ &+ \sum_{\gamma} \frac{J_{\gamma}}{2\Omega m} \sum_{\boldsymbol{k}} \sum_{\langle i,j \rangle_{\gamma}} \Bigg\{ \Bigg[\mathcal{B}_{ij}^{\gamma *} \left(e^{i\boldsymbol{k}\cdot\boldsymbol{\delta}} \tau_{ij}^{\gamma} a_{\mu_i,\boldsymbol{k}}^{\dagger} a_{\mu_j,\boldsymbol{k}} + e^{-i\boldsymbol{k}\cdot\boldsymbol{\delta}} \tau_{ij}^{\gamma *} b_{\mu_i,-\boldsymbol{k}}^{\dagger} b_{\mu_j,-\boldsymbol{k}} \right) \\ &\qquad + \mathcal{B}_{ij}^{\gamma} \left(e^{-i\boldsymbol{k}\cdot\boldsymbol{\delta}} \tau_{ij}^{\gamma *} a_{\mu_i,\boldsymbol{k}} a_{\mu_j,\boldsymbol{k}}^{\dagger} + e^{i\boldsymbol{k}\cdot\boldsymbol{\delta}} \tau_{ij}^{\gamma} b_{\mu_i,-\boldsymbol{k}} b_{\mu_j,-\boldsymbol{k}}^{\dagger} \right) \\ &\qquad - \mathcal{A}_{ij}^{\gamma *} \left(e^{-i\boldsymbol{k}\cdot\boldsymbol{\delta}} \tau_{ij}^{\gamma *} a_{\mu_i,\boldsymbol{k}} b_{\mu_j,-\boldsymbol{k}} - e^{i\boldsymbol{k}\cdot\boldsymbol{\delta}} \tau_{ij}^{\gamma} b_{\mu_i,-\boldsymbol{k}} a_{\mu_j,\boldsymbol{k}} \right) \\ &\qquad - \mathcal{A}_{ij}^{\gamma} \left(e^{i\boldsymbol{k}\cdot\boldsymbol{\delta}} \tau_{ij}^{\gamma} a_{\mu_i,\boldsymbol{k}}^{\dagger} b_{\mu_j,-\boldsymbol{k}}^{\dagger} - e^{-i\boldsymbol{k}\cdot\boldsymbol{\delta}} \tau_{ij}^{\gamma *} b_{\mu_i,-\boldsymbol{k}}^{\dagger} a_{\mu_j,\boldsymbol{k}}^{\dagger} \right) \Bigg] \Bigg\} \end{aligned} \tag{3.8}$$

with z_{γ} the coordination number, m the number of sites in the unit cell, Ω the number of points in the Brillouin zone (see appendix A.1 for the relation with N_s and m) and $\boldsymbol{\delta} = \boldsymbol{x}_j - \boldsymbol{x}_i$ the distance between unit cells. In this equation we have summations over γ which labels the neighbor distance (from first to third nearest-neighbor), over $\boldsymbol{k}$ which spans the Brillouin zone, over the sites of a unit cell i and finally over j which is the γ-th nearest-neighbor of site i.

In this step, we made the additional assumption that $\lambda_i = \lambda$ in order to have a single Lagrange multiplier to enforce the occupation constraint, meaning that the constraint is only imposed on average. This approximation might lead to nonphysical results, so one might improve the simulation by considering different λ for each site in the unit cell, which also enlarges the parameters space and thus the complexity of the minimization.

The mean-field Hamiltonian can be rewritten in a compact form by introducing the vectors

$$\psi^\dagger_{\boldsymbol{k}} = \left(a^\dagger_{1,\boldsymbol{k}}, a^\dagger_{2,\boldsymbol{k}}, \dots a^\dagger_{m,\boldsymbol{k}}, b_{1,-\boldsymbol{k}}, b_{2,-\boldsymbol{k}}, \dots b_{m,-\boldsymbol{k}}\right),$$

such that (3.8) becomes

$$\frac{\mathcal{H}_{MF}}{N_s} = \sum_\gamma \frac{1}{2} z_\gamma J_\gamma \left(|\mathcal{A}^\gamma_{ij}|^2 - |\mathcal{B}^\gamma_{ij}|^2\right) + \lambda\left(2S+1\right) + \frac{1}{\Omega m} \sum_{\boldsymbol{k}} \psi^\dagger_{\boldsymbol{k}} \mathcal{N}_{\boldsymbol{k}} \psi_{\boldsymbol{k}}.$$

Here $\mathcal{N}_{\boldsymbol{k}}$ is a $(2m, 2m)$ matrix. The elements of $\mathcal{N}_{\boldsymbol{k}}$ are found in the last summation of (3.8), which gives this matrix the general structure

$$\mathcal{N}_{\boldsymbol{k}} = \mathrm{diag}(\lambda) + \left(\begin{array}{cc|cc} \ddots & \alpha & \ddots & \eta \\ \gamma & \ddots & \theta & \ddots \\ \hline \ddots & \zeta & \ddots & \delta \\ \epsilon & \ddots & \beta & \ddots \end{array}\right)$$

where the Greek letters from α to θ refer to the terms in (3.8). They are upper/lower triangular matrices which overlap on the diagonals. Since $\mathcal{N}_{\boldsymbol{k}}$ is Hermitian, these terms are related as $\gamma = \alpha^\dagger$, $\zeta = \theta^\dagger$, $\epsilon = \eta^\dagger$, and $\beta = \delta^\dagger$, and they read

$$\alpha = \sum_\gamma \frac{J_\gamma}{2} \sum_{i \in UC} \sum_{j \in nn_\gamma(i)} \mathcal{B}^{\gamma *}_{ij} e^{i\boldsymbol{k}\cdot\boldsymbol{\delta}} \tau^\gamma_{ij}$$

$$\delta = \sum_\gamma \frac{J_\gamma}{2} \sum_{i \in UC} \sum_{j \in nn_\gamma(i)} \mathcal{B}^{\gamma}_{ij} e^{i\boldsymbol{k}\cdot\boldsymbol{\delta}} \tau^\gamma_{ij}$$

$$\eta = -\sum_\gamma \frac{J_\gamma}{2} \sum_{i \in UC} \sum_{j \in nn_\gamma(i)} \mathcal{A}^{\gamma}_{ij} e^{i\boldsymbol{k}\cdot\boldsymbol{\delta}} \tau^\gamma_{ij}$$

$$\theta = \sum_\gamma \frac{J_\gamma}{2} \sum_{i \in UC} \sum_{j \in nn_\gamma(i)} \mathcal{A}^{\gamma}_{ij} e^{-i\boldsymbol{k}\cdot\boldsymbol{\delta}} \tau^{\gamma *}_{ij}$$

In order to diagonalize the mean-field Hamiltonian, we perform a Bogoliubov transformation. The ground state energy per site then reads

$$\mathcal{E}_{MF} = \sum_\gamma \frac{1}{2} z_\gamma J_\gamma \left(|\mathcal{A}^\gamma_{ij}|^2 - |\mathcal{B}^\gamma_{ij}|^2\right) + \lambda\left(2S+1\right) + \frac{1}{\Omega m} \sum_{\boldsymbol{k},\mu} \epsilon^\mu(\boldsymbol{k}), \tag{3.9}$$

where $\mu = 1, \ldots, m$ and ϵ^μ are the positive eigenvalues. This transformation for bosons is reviewed in [174] and more generally in [129, 175]. To be more specific, we need to find a matrix $M_{\boldsymbol{k}}$ which transforms

$$\psi_{\boldsymbol{k}} = M_k \tilde{\psi}_{\boldsymbol{k}}, \tag{3.10}$$

such that two conditions are satisfied: the final matrix has to be diagonal and the vectors $\tilde{\psi}_{\boldsymbol{k}}$ in addition have to satisfy the canonical commutation relations $\left[\tilde{\psi}^\dagger_{\boldsymbol{k}}, \tilde{\psi}_{\boldsymbol{k}}\right] = \mathcal{J}$, where $\mathcal{J}$ is a diagonal $(2m, 2m)$ matrix with -1 on the first m terms and 1 on the others. These two conditions can be written as

$$M^\dagger_{\boldsymbol{k}} \mathcal{N}_{\boldsymbol{k}} M_{\boldsymbol{k}} = \omega_{\boldsymbol{k}}, \tag{3.11a}$$

$$M^\dagger_{\boldsymbol{k}} \mathcal{J} M_{\boldsymbol{k}} = \mathcal{J}. \tag{3.11b}$$

The second condition makes the Bogoliubov transformation different from the normal diagonalization, where $\mathcal{J} = \mathbb{1}$. In order to perform this transformation we first have to verify that $\mathcal{N}_{\boldsymbol{k}}$ is *positive definite*. In fact, while performing the minimization there might be parameter choices that do not yield positive eigenvalues, which then have to be discarded as non-physical. Then, we find an upper-triangular matrix $\mathcal{C}_{\boldsymbol{k}}$ such that $\mathcal{N}_{\boldsymbol{k}} = \mathcal{C}^\dagger_{\boldsymbol{k}} \mathcal{C}_{\boldsymbol{k}}$ through a Cholesky decomposition. Finally, we diagonalize $\mathcal{G}_{\boldsymbol{k}} = \mathcal{C}^\dagger_{\boldsymbol{k}} \mathcal{J} \mathcal{C}_{\boldsymbol{k}}$. This is a Hermitian matrix whose first m eigenvalues are positive and the others negative.

Since the kagome lattice has a three-site unit cell, it is not well suited for an analytic treatment in this framework. Therefore, we rely on numerical simulations. The ground state of the model can be found by extremizing the MF energy with respect to all the mean-field parameters and the Lagrange multiplier. This procedure involves a large number of mean-field parameters, so, in order to be able to find a solution we rely on the *projective symmetry group* classification of possible ansätze. This assumes that some symmetries, such as translational invariance, will be respected by the solution, thus reducing the number of free parameters. The classification for our model will be laid in the next section.

Minimization and Self-Consistency

There are two equivalent ways of finding the ground state. The first one consists in looking for the saddle point where the derivative of the free energy with respect to all the mean-field parameters is zero by using a *gradient descent* routine, i.e. updating the search of the parameters by computing numerical derivatives. An important aspect of the gradient descent minimization is that we are not minimizing the energy with respect to each of the parameters. This is due to the fact that the solution lies actually at a saddle point: it is maximal with respect to the Lagrange multiplier. In addition to this, there is a fundamental difference between pairing and hopping mean-field parameters: the solution has to be a the minimum with respect to $\mathcal{A}^\gamma$

and a maximum with respect to $\mathcal{B}^\gamma$ for positive couplings J_γ. This can be seen by computing the second derivative of $\mathcal{E}_{MF}$:

$$\frac{\partial^2 \mathcal{E}_{MF}}{\partial^2 |\mathcal{A}^\gamma|} \propto J_\gamma,$$
$$\frac{\partial^2 \mathcal{E}_{MF}}{\partial^2 |\mathcal{B}^\gamma|} \propto -J_\gamma.$$

Hence, while performing the minimization, we also need to consider the sign of the second derivatives of the parameters to establish whether it is a minimum or a maximum.

The gradient descent method requires computation of derivatives of the free energy with respect to the mean-field parameters, which when done with a finite difference method, can introduce numerical inaccuracies. Furthermore, the method becomes rapidly computationally expensive with a growing number of parameters. Another way of reaching the ground state is that of iteratively solving the *self-consistency* relations. These are of the form

$$\mathcal{A}_{ij}^\gamma = \langle A_{ij}^\gamma \rangle.$$

In order to do so, we need to write down the hopping and pairing operators in terms of Bogoliubov bosons using (3.10) and to exploit the definition of ground state as the vacuum of such excitations. We decompose the transformation matrix $M_{\boldsymbol{k}}$ as

$$M_{\boldsymbol{k}} = \begin{pmatrix} U_{\boldsymbol{k}} & X_{\boldsymbol{k}} \\ V_{\boldsymbol{k}} & Y_{\boldsymbol{k}} \end{pmatrix},$$

where each component is a $m \times m$ matrix. The final form of pairing and hopping operators then is

$$\langle A_{ij}^\gamma \rangle = \frac{1}{2\Omega} \sum_{\boldsymbol{k}} \Big(\tau_{ij}^{\gamma *} e^{i\boldsymbol{k}\cdot(\boldsymbol{x}_i - \boldsymbol{x}_j)} U_{\mu\nu}(\boldsymbol{k}) V_{\lambda\nu}^*(\boldsymbol{k}) - \tau_{ij}^{\gamma} e^{-i\boldsymbol{k}\cdot(\boldsymbol{x}_i - \boldsymbol{x}_j)} Y_{\mu\nu}^*(k) X_{\lambda\nu}(k) \Big),$$
$$\langle B_{ij}^\gamma \rangle = \frac{1}{2\Omega} \sum_{\boldsymbol{k}} \Big(\tau_{ij}^{\gamma} e^{-i\boldsymbol{k}\cdot(\boldsymbol{x}_i - \boldsymbol{x}_j)} X_{\mu\nu}^*(\boldsymbol{k}) X_{\lambda\nu}(\boldsymbol{k}) + \tau_{ij}^{\gamma *} e^{i\boldsymbol{k}\cdot(\boldsymbol{x}_i - \boldsymbol{x}_j)} V_{\mu\nu}(\boldsymbol{k}) V_{\lambda\nu}^*(\boldsymbol{k}) \Big),$$

where μ, λ are the unit cell indexes of respectively sites i, j and summation over repeated indexes is implied. The procedure of this method of solution is the following: starting from a set of mean-field parameters $\{O\}$, we maximize the free energy with respect to the Lagrange multiplier λ in order to fulfill the occupation constraint. Then, using λ and $\{O\}$ we compute a new set of mean-field parameters using the relations above and iterate this procedure until convergence to a stationary point. This procedure is more efficient than the gradient descent and allows to consider a larger set of mean-field parameters, thus making it best suited for considering a large number of different ansätze. In both approaches, one has to pay attention to the dependence on initial conditions. Hence, we need to repeat the procedure many times with different initial parameters in order to be sure to find all the saddle points of the free energy.

3.3.2 Projective Symmetry Group Classification

In this section I review the derivation of the projective symmetry group (PSG) classification presented in [174] and adapt it to our specific model. The mean-field parameters' manifold grows exponentially in system size. In addition, the Lagrange multipliers have to be optimized for each free energy evaluation, making the numerical convergence of the problem a demanding task. This was done for relatively small system sizes in [176] and it was shown that in almost all cases the mean-field solution was highly symmetric. The idea then is to restrict our search to solutions of the self-consistency equations that respect some of the symmetries of the model. A set of mean-field parameters $\{\mathcal{A}_{ij}, \mathcal{B}_{ij}, \lambda\}$ is called an *ansatz*. We demand that our ansätze respect some symmetries of the original Hamiltonian. The symmetries of the Heisenberg interaction on the kagome lattice are: global spin rotation, time reversal (TR) symmetry and lattice symmetries (translations T_1 and T_2, rotations R_6 and reflections σ for the kagome lattice, shown in Figure 3.2a). In our case the ansatz automatically respects the spin rotation symmetry since we are considering bond operators of the form (3.7). Furthermore, we want to consider ansätze which respect the lattice symmetries and, eventually, also time-reversal symmetry. In addition, our Hamiltonian contains DM interactions which break some of these symmetries. The resulting PSG will thus be different from the one of the pure Heisenberg model.

First of all, let us note that the introduction of bosonic operators imbues the theory with a $\mathcal{G} = U(1)$ gauge freedom. A gauge transformation (GT) acts on the Schwinger bosons as

$$b_{j,\sigma} = e^{i\theta(j)} b_{j,\sigma}.$$

The effect on the bond operators (3.7) is thus

$$\begin{aligned} A_{ij} &\to e^{i(\theta(i)+\theta(j))} A_{ij}, \\ B_{ij} &\to e^{-i(\theta(i)-\theta(j))} B_{ij}, \end{aligned}$$

and since it is a GT, the Hamiltonian described by $\{\mathcal{A}_{ij}, \mathcal{B}_{ij}\}$ will remain unaffected by the action of the gauge transformation. If two mean-field Hamiltonians $\mathcal{H}_{MF}$ have the same physical properties, then their ansätze are related by a GT. Hence, a GT modifies the ansatz, but not the physical quantities.

Let us now consider the lattice symmetry group χ. The spinon (bosonic) operators will transform under the action of $X \in \chi$ as

$$a_i \to a_{X(i)},$$

The same happens for b_i and by extension for the bond operators (3.7). If an ansatz respects a symmetry, then the physical quantities are the same before and after the application of that symmetry transformation. But we also know that if two systems have the same physical quantities, then they are related by a GT. This means that there exists at least one GT $G_X \in \mathcal{G}$ such that $G_X X$ leaves the ansatz invariant. The set of transformations $\mathcal{G} \times \chi$ which do not change the ansatz is called the projective symmetry group (PSG) *of that particular ansatz*. This group only depends on the lattice symmetries χ and on the ansatz, not on the Hamiltonian. An important subgroup of the PSG is the so-called invariant gauge group (IGG) which is the group of gauge transformations related to the identity $X = I$. The IGG is the group of gauge transformations that leaves the ansatz invariant. From the PSG of an ansatz we therefore know which symmetries it preserves and how these symmetries are realized projectively in the gauge group.

For our purpose of restricting the space of relevant ansätze, we would like to choose a symmetry group χ and find all the possible ansätze compatible with it. In order to do so we have to find the so-called *algebraic* PSG (A-PSG), which is constructed by constraining the possible gauge group representations using the symmetry relations of χ. The idea is that any symmetry group will have to respect some consistency relations. These can be written in the form of products of symmetry operations on the lattice yielding the identity. If a lattice symmetry can be written in several ways, also the associated gauge transformations should be compatible, with the identity in that case being the IGG. For example, if we have a relation $X_1X_2 = X_2X_1$ for $X_i \in \chi$, then we can re-write this as $X_1X_2X_1^{-1}X_2^{-1} = 1$. In terms of the associated GT, this becomes $G_1X_1G_2X_2X_1^{-1}G_1^{-1}X_2^{-1}G_2^{-1} \in$ IGG, and leads to a constraint on the possible realizations of G_χ.

In the non-TR symmetry breaking classification, we consider χ as the group of all lattice symmetries, and at the end impose TR symmetry by considering only ansätze which are real up to a gauge transformation. This was done before in [177]. Chiral solutions (that break TRS) have been shown to be competitive ground states, as shown for example in [133]. To also include chiral ansätze, we will follow the procedure outlined in [174]. The idea is to consider ansätze that respect all the lattice symmetries only up to a TR transformation. In order to do so, we need to distinguish between *odd* and *even* lattice symmetries: they are characterized by having odd or even parity under TR, respectively. Once we know χ_e, we construct its A-PSG. Then, we consider the odd symmetries χ_o, which leads to two types of constraints: first, same type (pairing or hopping) mean-field parameters on bonds related by such symmetries will have the same modulus. Second, fluxes are physical quantities and thus gauge independent, and are sent to their opposite by TR. Thus, they are unchanged by even transformations. The constraints arise from considering all non-trivial fluxes on the lattice and consider all possible cases of parities for the transformations of χ_o under TR.

Let us start by deriving the A-PSG of a triangular Bravais lattice, which has

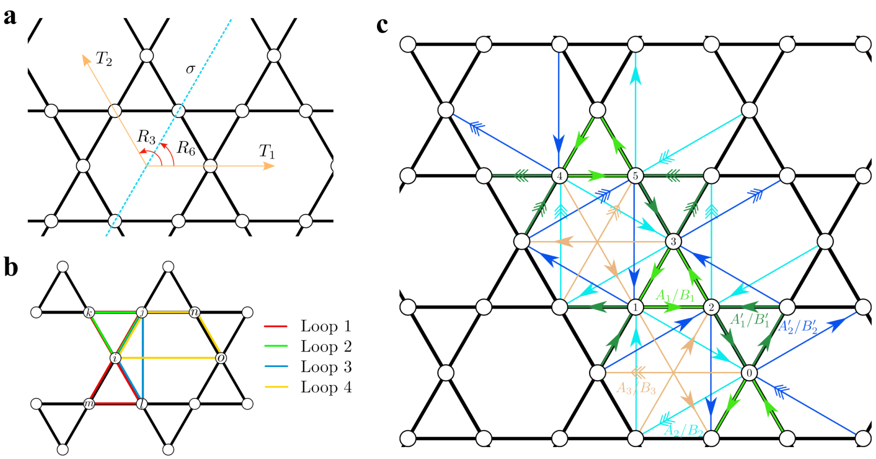

Figure 3.2: a, Symmetries of the kagome lattice. The lattice directions considered in the text coincide with T_1 and T_2. **b**, Loops that need to be considered in order to account for χ_o. **c**, Bond relations of hopping and pairing operators on the kagome lattice. These relations come from the A-PSG derived using only translations and R_3 rotations. For first and second neighbor distances there are two nonequivalent bonds. A double arrow on the bond indicate that the phase of the corresponding mean-field parameter has an additional phase $p_1\pi$. Numbers on the sites indicate the used convention for ordering the 6-sites unit cell. *Figure adapted from [3] with permission from the American Physical Society.*

$\chi_e = \{T_1, T_2, R_3\}$. These are all even symmetries for the kagome lattice. Since R_6 is also a symmetry in the kagome lattice, $R_3 = R_6^2$ must have even parity. By considering the lattice relation $T_2 R_6 = R_6 T_1 T_2$ we can see that $T_1 \in \chi_e$ and in the same way the relation $T_1 R_6 = R_6 T_2^{-1}$ yields $T_2 \in \chi_e$. Thus, the odd symmetry group will be $\chi_o = \{R_6, \sigma\}$. The symmetries are reported in Figure 3.2a. This A-PSG was computed in [174], the gauge transformations associated to each symmetry operator are

$$
\begin{aligned}
\theta_{T_1}(r_1, r_2) &= 0 \\
\theta_{T_2}(r_1, r_2) &= p_1\pi[r_1] \\
\theta_{R_3}(r_1, r_2) &= p_1\pi[r_1]\left([r_2] - \frac{[r_1]+1}{2} + [r_2^* - r_1^*]\right) + g_{R_3}(r_1^*, r_2^*)
\end{aligned}
$$

with $p_1 \in \{0, 1\}$ labeling the two different ansätze and r_1, r_2 are coordinates in the two lattice directions, with an integer $[r_i]$ and fractional r_i^* part.

With the A-PSG at hand we first of all note that it only depends on one parameter p_1, meaning that there are only two equivalence classes. In particular, since p_1 enters in the definition of θ_{T_2}, we see that the ansatz will have a 3-site unit cell for $p_1 = 0$, while it is doubled for $p_1 = 1$. For each type of bond, we need to consider a starting point to cover all the lattice using the symmetries of χ_e (see Figure 3.2c). For first and second nearest neighbors, there are two nonequivalent sets of bonds not related by any symmetry and we will denote them with a prime index: for example the nearest neighbor pairing mean-field operators $\mathcal{A}_1$ and $\mathcal{A}'_1$. Starting from a bond, we can obtain the values of the others by the procedure

$$\mathcal{A}_{i\to j} = e^{i(\theta_\chi(i)+\theta_\chi(j))}\mathcal{A}_{\chi(i)\to\chi(j)}$$
$$\mathcal{B}_{i\to j} = e^{i(\theta_\chi(i)-\theta_\chi(j))}\mathcal{B}_{\chi(i)\to\chi(j)}$$

This yields the bond relations in Figure 3.2c for first, second and third nearest-neighbors.

Up to this point there is a total of 20 mean-field parameters: 10 moduli $\mathcal{A}_1$, $\mathcal{A}'_1$, $\mathcal{A}_2$, $\mathcal{A}'_2$, $\mathcal{A}_3$, $\mathcal{B}_1$, $\mathcal{B}'_1$, $\mathcal{B}_2$, $\mathcal{B}'_2$, $\mathcal{B}_3$ and the corresponding 10 phases. This is still a large parameter space in which to look for solutions. Luckily, we can restrict this number of free parameters by exploiting the remaining symmetries. First of all, we can fix $\phi_{\mathcal{A}_1} = 0$. The relevant additional symmetries not yet considered will be R_6 ($\pi/3$-rotations) and σ (reflection) for the Heisenberg model, only R_6 in the case of the staggered DM interactions considered in [105–108, 178] and finally only σ for the uniform DM interaction used in our model [1]. By looking at the interaction directions in 3.1b, we can see that reflection symmetry is respected while $\pi/3$ rotations are not. This can be illustrated by applying a lattice rotation: the link changes direction, but the DM vector stays the same, therefore the energy changes in the symmetry transformed bond. When applying a reflection instead, the link as well as the DM vector stay the same. The completely opposite scenario happens if we consider instead a staggered DM vector on all triangles. Then, it is clear that σ is no longer a symmetry, while R_6 is restored.

Let us now take into consideration both R_6 and σ, in order to classify all the ansätze of the pure Heisenberg model. The loops that need to be considered in the lattice are reported in Figure 3.2b. The corresponding operators are

$$\begin{aligned}
\text{Loop 1:} &\quad A^\dagger_{ij}A_{jk}A^\dagger_{ki}A_{il}A^\dagger_{lm}A_{mi},\\
\text{Loop 2:} &\quad A^\dagger_{ij}A_{jk}B_{ki},\\
\text{Loop 3-a:} &\quad A^\dagger_{lj}A_{ji}B_{il},\\
\text{Loop 3-b:} &\quad A^\dagger_{ji}A_{il}B_{lj},\\
\text{Loop 4-a:} &\quad A^\dagger_{io}A_{on}B_{nj}B_{ji},\\
\text{Loop 4-b:} &\quad A^\dagger_{on}A_{nj}B_{ji}B_{io},
\end{aligned}$$

---

[1] Note the ambiguity in the definition of staggered and uniform DM interactions [179]. In this dissertation we stick to the notation of [106].

$N°$	$(\epsilon_R, \epsilon_\sigma)$	p_1	$\phi'_{\mathcal{A}_1}$	$\phi_{\mathcal{B}_1}$	$\phi'_{\mathcal{B}_1}$	$\phi_{\mathcal{A}_2}$	$\phi'_{\mathcal{A}_2}$	$\phi_{\mathcal{B}_2}$	$\phi'_{\mathcal{B}_2}$	$\phi_{\mathcal{A}_3}$	$\phi_{\mathcal{B}_3}$	compatible order(s)
1	$(1,1)$	0	0	$p_2\pi$	$p_2\pi$	free	$\phi_{\mathcal{A}_2}$	$p_3\pi$	$p_3\pi$	-	$p_4\pi$	$\mathbf{Q}=0$
2	$(1,1)$	0	π	$p_2\pi$	$p_2\pi$	-	-	$p_3\pi$	$p_3\pi$	free	$p_4\pi$	$\sqrt{3}\times\sqrt{3}$
3	$(1,1)$	1	0	$p_2\pi$	$p_2\pi$	free	$\phi_{\mathcal{A}_2}$	$p_3\pi$	$p_3\pi$	free	-	?
4	$(1,1)$	1	π	$p_2\pi$	$p_2\pi$	-	-	$p_3\pi$	$p_3\pi$	-	-	?
5	$(1,-1)$	0	0	free	$\phi_{\mathcal{B}_1}$	$p_2\pi$	$p_2\pi$	free	$\phi_{\mathcal{B}_2}$	-	$p_3\pi$	$\mathbf{Q}=0$
6	$(1,-1)$	0	π	free	$\phi_{\mathcal{B}_1}$	$p_2\pi+\frac{\pi}{2}$	$p_2\pi-\frac{\pi}{2}$	free	$\phi_{\mathcal{B}_2}$	$p_3\pi$	$p_4\pi$	$\sqrt{3}\times\sqrt{3}$
7	$(1,-1)$	1	0	free	$\phi_{\mathcal{B}_1}$	$p_2\pi$	$p_2\pi$	free	$\phi_{\mathcal{B}_2}$	$p_3\pi$	$\frac{\pi}{2}+p_4\pi$	?
8	$(1,-1)$	1	π	free	$\phi_{\mathcal{B}_1}$	$p_2\pi+\frac{\pi}{2}$	$p_2\pi-\frac{\pi}{2}$	free	$\phi_{\mathcal{B}_2}$	-	$\frac{\pi}{2}+p_3\pi$	*octahedral*
9	$(-1,1)$	0	0	free	$-\phi_{\mathcal{B}_1}$	free	-$\phi_{\mathcal{A}_2}$	$p_2\pi$	$p_2\pi$	-	free	$\mathbf{Q}=0$
10	$(-1,1)$	0	π	free	$-\phi_{\mathcal{B}_1}$	-	-	$p_2\pi$	$p_2\pi$	$p_3\pi$	free	$\sqrt{3}\times\sqrt{3}$
11	$(-1,1)$	1	0	free	$-\phi_{\mathcal{B}_1}$	free	-$\phi_{\mathcal{A}_2}$	$p_2\pi$	$p_2\pi$	$p_3\pi$	-	*cuboc-2*
12	$(-1,1)$	1	π	free	$-\phi_{\mathcal{B}_1}$	-	-	$p_2\pi$	$p_2\pi$	-	-	?
13	$(-1,-1)$	0	ϕ	$p_2\pi$	$p_2\pi$	$\frac{\phi}{2}+p_3\pi$	$\frac{\phi}{2}+p_3\pi$	free	$-\phi_{\mathcal{B}_2}$	$\frac{\phi+\pi+2p_4\pi}{2}$	$p_5\pi$	$\mathbf{Q}=0, \sqrt{3}\times\sqrt{3}$
14	$(-1,-1)$	1	ϕ	$p_2\pi$	$p_2\pi$	$\frac{\phi}{2}+p_3\pi$	$\frac{\phi}{2}+p_3\pi$	free	$-\phi_{\mathcal{B}_2}$	$\frac{\phi+2p_4\pi}{2}$	-	*cuboc-1*
15	$(\cdot,1)$	0	0	free	$-\phi_{\mathcal{B}_1}$	free	free	$p_2\pi$	$p_3\pi$	-	free	$\mathbf{Q}=0$
16	$(\cdot,1)$	0	π	free	$-\phi_{\mathcal{B}_1}$	-	-	$p_2\pi$	$p_3\pi$	free	free	$\sqrt{3}\times\sqrt{3}$
17	$(\cdot,1)$	1	0	free	$-\phi_{\mathcal{B}_1}$	free	free	$p_2\pi$	$p_3\pi$	free	-	*cuboc-2*
18	$(\cdot,1)$	1	π	free	$-\phi_{\mathcal{B}_1}$	-	-	$p_2\pi$	$p_3\pi$	-	-	?
19	$(\cdot,-1)$	0	ϕ	free	$\phi_{\mathcal{B}_1}$	$\frac{\phi}{2}+p_2\pi$	$\frac{\phi}{2}+p_3\pi$	free	free	$\frac{\phi+\pi+2p_4\pi}{2}$	$p_5\pi$	$\mathbf{Q}=0, \sqrt{3}\times\sqrt{3}$
20	$(\cdot,-1)$	1	ϕ	free	$\phi_{\mathcal{B}_1}$	$\frac{\phi}{2}+p_2\pi$	$\frac{\phi}{2}+p_3\pi$	free	free	$\frac{\phi+2p_4\pi}{2}$	$p_5\pi-\frac{\pi}{2}$	*cuboc-1,octahedral*

Table 3.1: All possible ansätze for the Heisenberg model on the Kagome lattice without (1 to 14) and with (15 to 20) uniform DM interaction. $p_i = \pm 1$ and an empty spot means that the corresponding bond has to vanish because of symmetry constraints. All amplitudes at the same distance (1st, 2nd, 3rd n.n.) are equal (separately for $\mathcal{A}$ and $\mathcal{B}$ parameters) without DM. For uniform DM interaction this is not true for the 2nd nn parameters, i.e. $|\mathcal{A}_2| \neq |\mathcal{A}'_2|$ and same for $\mathcal{B}_2$. The last column reports the regular orders compatible with each ansatz.

where each bond has to be taken with the correct sign and phase, as defined in Figure 3.2c. In order to implement a symmetry χ, one needs to impose that the phase of a loop is ϵ_χ times the phase of the χ-transformed loop.

If we consider both R_6 and σ we obtain the following constraints

$$\begin{aligned}
\phi'_{\mathcal{A}_1} &= -\epsilon_{R_6}\phi'_{\mathcal{A}_1} \\
\phi'_{\mathcal{A}_1} &= -\epsilon_{\sigma}\phi'_{\mathcal{A}_1} \\
\phi_{\mathcal{B}_1} &= \epsilon_{R_6}\phi'_{\mathcal{B}_1} \\
\phi_{\mathcal{B}_1} &= -\epsilon_{\sigma}\phi'_{\mathcal{B}_1} \\
\phi'_{\mathcal{A}_2} &= \epsilon_{R_6}(\phi_{\mathcal{A}_2} - \phi'_{\mathcal{A}_1}) \\
\phi'_{\mathcal{A}_2} &= \epsilon_{\sigma}(\phi'_{\mathcal{A}_2} - \phi'_{\mathcal{A}_1}) \\
\phi'_{\mathcal{B}_2} &= \epsilon_{R_6}\phi_{\mathcal{B}_2} \\
\phi'_{\mathcal{B}_2} &= -\epsilon_{\sigma}\phi'_{\mathcal{B}_2} \\
\phi_{\mathcal{A}_3} + p_1\pi &= \epsilon_{R_6}\phi_{\mathcal{A}_3} + \pi + \phi'_{\mathcal{A}_1} \\
\phi_{\mathcal{A}_3} + p_1\pi &= \epsilon_{\sigma}\phi_{\mathcal{A}_3} + \pi + \phi'_{\mathcal{A}_1} \\
\phi_{\mathcal{B}_3} + p_1\pi &= -\epsilon_{R_6}\phi_{\mathcal{B}_3} \\
\phi_{\mathcal{B}_3} + p_1\pi &= \epsilon_{\sigma}\phi_{\mathcal{B}_3}
\end{aligned}$$

Order	$(\epsilon_R, \epsilon_\sigma)$	p_1	$\mathcal{A}_1$	$\mathcal{B}_1$	$\mathcal{A}_2$	$\mathcal{B}_2$	$\mathcal{A}_3$	$\mathcal{B}_3$	$\phi'_{\mathcal{A}_1}$	$\phi_{\mathcal{B}_1}$	$\phi'_{\mathcal{B}_1}$	$\phi_{\mathcal{A}_2}$	$\phi'_{\mathcal{A}_2}$	$\phi_{\mathcal{B}_2}$	$\phi'_{\mathcal{B}_2}$	$\phi_{\mathcal{A}_3}$	$\phi_{\mathcal{B}_3}$
$\mathbf{Q} = 0$	$(\pm 1, \pm 1)$	0	$\sqrt{3}/4$	$1/4$	$\sqrt{3}/4$	$1/4$	0	$1/2$	0	π	π	π	π	π	π	-	0
$\sqrt{3} \times \sqrt{3}$	$(\pm 1, \pm 1)$	0	$\sqrt{3}/4$	$1/4$	0	$1/2$	$\sqrt{3}/4$	$1/4$	π	π	π	-	-	0	0	0	π
cuboc-1	$(-1, -1)$	1	$\sqrt{3}/4$	$1/4$	$1/4$	$\sqrt{3}/4$	$1/2$	0	$2\theta_0$	π	π	$\pi + \theta_0$	$\pi + \theta_0$	$-\theta_0$	θ_0	θ_0	-
cuboc-2	$(-1, 1)$	1	$1/4$	$\sqrt{3}/4$	$\sqrt{3}/4$	$1/4$	$1/2$	0	0	$\pi + \theta_0$	$\pi - \theta_0$	$\pi - \theta_0$	$\pi + \theta_0$	0	0	0	-
octahedral	$(1, -1)$	1	$1/(2\sqrt{2})$	$1/(2\sqrt{2})$	$1/(2\sqrt{2})$	$1/(2\sqrt{2})$	0	$1/2$	π	$5\pi/4$	$5\pi/4$	$3\pi/2$	$\pi/2$	$\pi/4$	$\pi/4$	-	$3\pi/2$

Table 3.2: Pairing and hopping amplitudes and phases for classical $O(3)$ regular orders on the Kagome lattice. The value of θ_0 is $\arctan(\sqrt{2}) \approx 0.95$.

There is one main difference between Heisenberg and staggered DM, which respect R_6, and uniform DM, which does not: when R_6 is a symmetry, all bonds of the same distance have the same amplitude. In the uniform DM case, instead, they can in principle assume different values. Nevertheless, since σ is a symmetry, the difference arises only at the second-nearest neighbor level. We report the full set of ansätze for the Heisenberg model and the uniform DM interaction in Table 3.1. Parameters p_i can take values $0, 1$ and differentiate the ansätze. In the table, we numbered the ansätze for different choices of ϵ_χ and p_1.

Counting all the possible combinations of p_i, there are many more different ansätze for the pure Heisenberg model than for the model with DM interactions. This is due to the fact that in the latter case, there are less symmetry restrictions leading to more free parameters in general, both phases and amplitudes.

3.3.3 Classical Orders

Once the ground state of the mean-field Hamiltonian has been obtained, we determine from the spinon dispersion whether it features a gap or not. SBMFT is particularly well suited for distinguishing long-range orders from gapped spin liquids. When the gap closes, the spinons are allowed to condense in the ground state. This condensate breaks the spin rotational invariance and results in a long-range ordered arrangement of spins on the lattice. In general, the long-range order to which an ansatz can condense is given by the form of the condensate. However, there are also examples of ansätze which do not allow condensation to any magnetic order as we will see later in the results' section. The set of classical orders that can be formed is restricted to states respecting the remaining symmetries up to a global spin rotation. These are the so-called *regular magnetic orders*, which have been classified, also for chiral orders, in [180]. In this classification, all possible classical orders on the kagome lattice that are $O(3)$-regular have been taken into account. These are the orders which for any lattice symmetry X allow for a global spin rotation $S_X \in O(3)$ such that the state is invariant under $S_X X$. The group $O(3)$ has been considered since it is the spin symmetry of the Heisenberg model.

The important quantities that will be useful for our analysis are the values of the amplitudes and phases of the pairing and hopping parameters in these classical orders, which then can be used as starting parameters for the minimization procedure. These values have been computed in Table 3.2 for $O(3)$ regular orders on the kagome

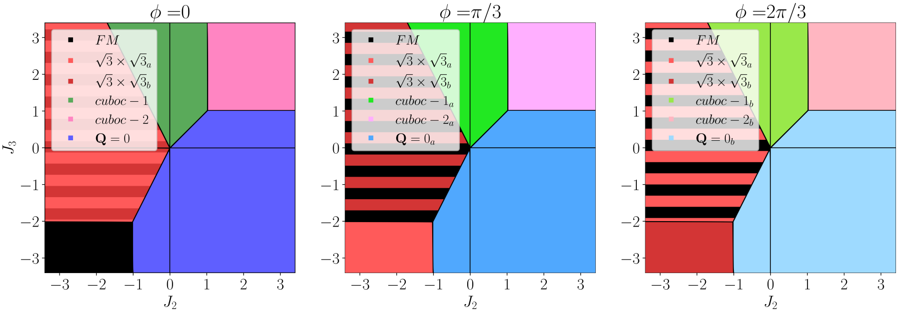

Figure 3.3: Classical phase diagram of the Heisenberg model (3.2). Choosing the value of the DM (first n.n.) angle to $n\pi/3$, $n = 0, 1, 2$, yields the same phase diagram with gauged transformed orders. $\sqrt{3} \times \sqrt{3}$ comes in two vector chiralities denoted by subscript a, b. Gauged transformed versions of $\mathbf{Q} = 0$, *cuboc-1*, *cuboc-2*, *octahedral* are also referred to in this way. FM stands for ferromagnetic order. *Figure adapted from [3] with permission from the American Physical Society.*

lattice with all lattice symmetries.

All phases and amplitudes have been obtained by considering the same loops used to evaluate the constraints of the A-PSG derived above. We start by taking the product of pairing and hopping operators along a loop and subsequently expanding them as in (3.7). This results in a sum of terms containing an even number of single-site boson operators. By considering the expression of the spins in terms of Schwinger bosons (3.5), we can then derive

$$\begin{aligned} a_i^\dagger a_i &= \frac{1}{2} + S^z, \\ b_i^\dagger b_i &= \frac{1}{2} - S^z, \\ a_i^\dagger b_i &= S^x + iS^y. \end{aligned}$$

Inserting these relations into the loop expressions and considering the real space values of the spin directions for the different orders, we obtain the results in Table 3.2.

3.4 Results

3.4.1 Classical Phase Diagram

It is instructive to first determine the classical ground state phase diagram corresponding to our model. As candidate states, we consider the regular orders defined in [180]. In addition, we take into account the orders obtained by gauge transforming the regular orders through our $\sqrt{3} \times \sqrt{3}$-type transformation mentioned in the

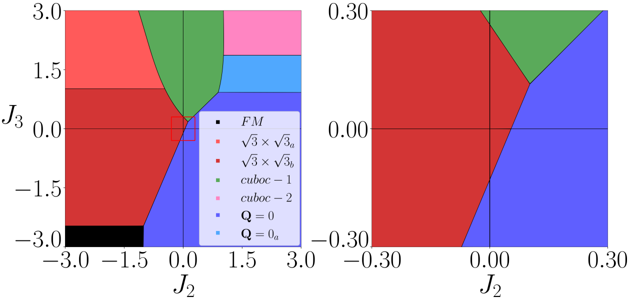

Figure 3.4: Classical phase diagram with DM angle $\phi = 0.05$. On the left panel a bigger parameter space is shown while in the right one we zoom in the region close to the $J_2 = J_3 = 0$ point. *Figure adapted from [3] with permission from the American Physical Society.*

introduction (Figure 3.1d). A third set of possible ground states is given by the generalized spiral orders. These are the magnetic orders which are obtained by considering only translations as symmetries in the method of Ref. [180]. They are defined by the directions of the spins in a 6-site unit cell [2] and by two angles defining the rotations of the spins when moving to the neighboring unit cell along the two nonequivalent lattice directions. In addition to the rotation, there can be also an inversion leading to two additional parameters and a total of 15 parameters. By minimizing the energy of such spiral states, we find the most probable candidate ground state at the classical level. With this most general choice of parameters, spiral states include all regular orders, gauged orders and umbrella states. The phase diagrams for different DM angles at $SU(2)$-invariant values are shown in Figure 3.3.

We can see that the two $\sqrt{3} \times \sqrt{3}$ orders with opposite vector chirality are degenerate at zero DM angle, while at DM angle $\phi = n\pi/3, n = 1, 2$, the degeneracy is lifted and one of them becomes degenerate with the in-plane ferromagnetic (FM) order at each point. This is due to the fact that the ferromagnetic order is transformed into one of the $\sqrt{3} \times \sqrt{3}$ orders under the gauge transformation, which in turn is transformed into its other vector chirality and finally back to the ferromagnetic order. As with the $\sqrt{3} \times \sqrt{3}$/ferromagnetic state, all the orders come in sets of three states that are generated by acting with the gauge transformation once or twice on the original order. We denote the once (twice) gauge transformed versions with the subscript a (b). Since the points with the DM phases $\phi = n\pi/3, \quad n = 1, 2$ are all effectively $SU(2)$ invariant, the structure of the phase diagram is the same.

Outside of these $SU(2)$ invariant points, the situation changes. The classical phase diagram for $\phi = 0.05$ is shown in Figure 3.4. We first of all note that a finite value of ϕ lifts the degeneracy between the two vector chiralities of the $\sqrt{3} \times \sqrt{3}$

---

[2] The general unit cell has 6 sites because of the parameter p_1 found in the PSG classification. By considering only a 3-site unit cell, orders like *cuboc-1*, *cuboc-2* and *octahedral* are excluded.

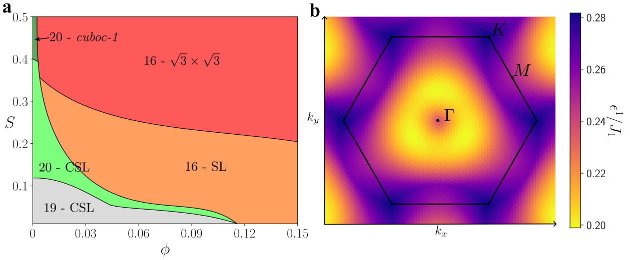

Figure 3.5: **a**, Phase diagram of 1st n.n. Heisenberg model on kagome lattice with the addition of DM interaction as a function of spin S and DM phase ϕ. When gapped, solution 16 is a spin liquid (SL) while solutions 19, 20 are chiral spin liquids (CSL). Ordered phases *cuboc-1* and $\sqrt{3} \times \sqrt{3}$ are gapless solutions of ansätze 20 and 16, respectively. **b**, Lowest band spinon dispersion of ansatz 19 evaluated for $S \sim 0.11$ and $\phi = 0$, showing a ring-like shape. *Figure adapted from [3] with permission from the American Physical Society.*

order. Also, the origin $J_2 = J_3 = 0$ of the phase diagram is no longer a degenerate point of three orders and it becomes fully $\sqrt{3} \times \sqrt{3}$. By zooming in on the region close to the origin (right panel of Figure 3.4) we illustrate how the degeneracy is lifted leaving a clear $\sqrt{3} \times \sqrt{3}$ order at the origin.

3.4.2 First Nearest-Neighbor

Turning to the quantum case, let us start by computing the $J_2 = J_3 = 0$ phase diagram in terms of the DM phase ϕ and spin S along the same line as [105–108], only with a uniform DM interaction instead. In this first calculation, we used a self-consistent method for finding the saddle points of the free energy and considered ansätze 15 to 20 in 3.1. The mean-field parameters thus are: $|\mathcal{A}_1|, |\mathcal{B}_1|, \phi_{\mathcal{B}_1}$, with the addition of $\phi'_{\mathcal{A}_1}$ for ansätze 19 and 20. The resulting phase diagram is reported in Figure 3.5a. First of all, we note that the chiral ground state at 0 DM is rapidly substituted by a $\sqrt{3} \times \sqrt{3}$ type of phase as the DM phase increases. By decreasing the spin value, we see that LRO phases get substituted by SL ones, as expected since quantum fluctuations become stronger. Three of the six solutions of Table 3.1 appear in the phase diagram: 16, 19 and 20. While 16 and 20 condense to coplanar $\sqrt{3} \times \sqrt{3}$ and chiral *cuboc-1* orders, respectively, after gap closing, there is no known order corresponding to ansatz 19. From the value of its phases, we determine that it is chiral, but it only appears as a SL in the phase diagram. This solution is the analog of the phase $A_4(0, 1)$ found in [105] for uniform DM interactions. It also has the same circular minima in spinon spectrum, as shown in Figure 3.5b. In our simulations, in the entire parameter region in which it converges as a solution of the self-consistent equations, it remains gapped.

This phase diagram should coincide with the ones in [105, 107] for DM phase $\phi = 0$. However, we see a slight difference at small S (around $S \lesssim 0.1$), where we find solution 19, while the *cuboc-1* was reported up to very small spin values in [105]. In our simulations, we took a precision of 10^{-7} for amplitudes and 10^{-5} for phases of the mean-field parameters, normalizing with respect to the spin value in order to achieve a uniform precision. We also note that the phase $A_1(1,0,1)$ found in [105], which would correspond to our ansatz 17, does not appear in our simulations.

We also computed the spin structure factor

$$\Xi(\boldsymbol{Q}) = \frac{1}{\mathcal{N}} \sum_{i,j} e^{-i\boldsymbol{Q}\cdot(\boldsymbol{r}_i - \boldsymbol{r}_j)} \langle \boldsymbol{S}_i \cdot \boldsymbol{S}_j \rangle \tag{3.12}$$

to distinguish the phases. The details of the computation are given in appendix A.2. From the structure factors, we can see the peaks which would show up in neutron scattering experiments in long-range orders, while we expect to see broader features in the spin liquid phases. In general, we expect DM interactions to favor in-plane orders due to the out-of-plane direction of the DM vector (see Figure 3.1b). Also, as argued in section 3.2, the presence of DM interactions reduces the symmetry of the model. This in turn reduces the effect of quantum fluctuations, thus favoring long-range order configurations. This general tendency can be observed in Figure 3.5a by noticing that the transition line between $\sqrt{3} \times \sqrt{3}$ LRO to SL (ansatz 16) happens at decreasing spin S values by increasing the DM strength.

Finally, we emphasize that the part of the phase diagram with multiple competing phases is restricted to DM angles $\phi \lesssim 0.12$ with our choice of DM interactions. For larger DM angle, the only solution that remains is 16, gapped (SL) and gapless ($\sqrt{3} \times \sqrt{3}$). In contrast, in the case of staggered DM interactions the phase diagram has multiple phases up to $\phi \sim 0.3$, after which the $\mathbf{Q} = 0$ order dominates.

3.4.3 Full Phase Diagrams

We now turn to the model with finite J_2 and J_3 parameters in the presence of uniform DM interactions of the form given in (3.3). We start with the phase diagrams at the $SU(2)$ invariant points, i.e. for DM phase equal to $\phi = 0, \pi/3, 2\pi/3$, in Figure 3.6a. We use a self-consistent method with precision 10^{-6} for amplitudes and 10^{-4} for phases, again normalized by the spin value in order to get a uniform precision in various plots. To distinguish between SL and LRO, we performed finite size scaling up to lattices of 2401 (ansatz) unit cells and used a cutoff of 10^{-2} for the gap value, as discussed in detail in appendix A.1.

The ansätze we considered are 15 to 20 in 3.1, since they are more general and include the solutions 1 to 14, which are expected to be the ansätze for the $SU(2)$ invariant points. We computed the J_1-J_2-J_3 phase diagram for spin values $S = 0.5, (\sqrt{3}-1)/2, 0.3, 0.2$. Four solutions mainly appear in the phase diagrams: 15, 16, 20 and 19. The first three condense, after gap closing to $\mathbf{Q} = 0$, $\sqrt{3}\times\sqrt{3}$ and *cuboc-1*

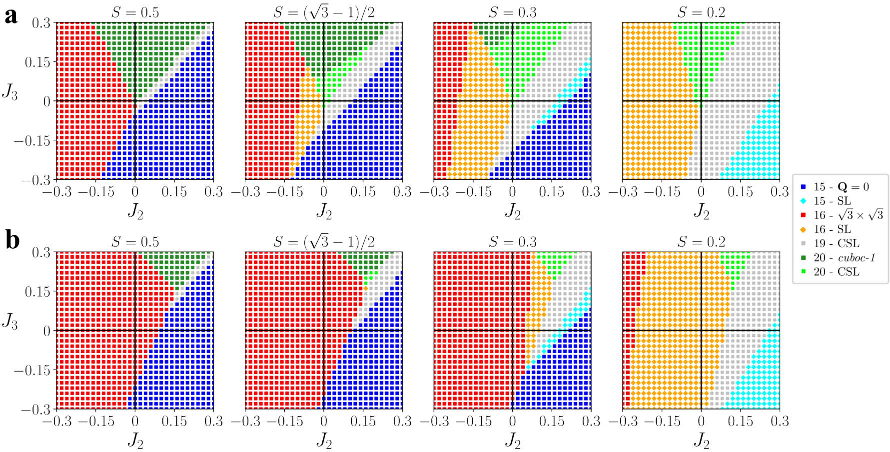

Figure 3.6: **a**, J_2-J_3 Phase diagrams at different spin values for DM phase $\phi = 0$. The other $SU(2)$ invariant points result in equal diagrams. The orders appearing are the same as for the classical phase diagram, namely $\sqrt{3} \times \sqrt{3}$, $\mathbf{Q} = 0$ and *cuboc-1*. We find one additional solution (19) appearing at the border between $\mathbf{Q} = 0$ and *cuboc-1*, which is chiral and always gapped (i.e. a SL). We can also appreciate that already at $S = (\sqrt{3} - 1)/2$ the ground state of the $J_2 = J_3 = 0$ Heisenberg antiferromagnet is in a gapped chiral spin liquid phase. By decreasing further the spin value, the whole considered parameter space becomes gapped. **b**, Same phase diagrams but with uniform DM interaction $\phi = 0.05$. The DM interaction favors solution 16 which becomes predominant in the considered parameter space. Also, it reduces the quantum fluctuations resulting in a phase diagram with more LRO gapless phases with respect to the same spin values in **a**. *Figure adapted from [3] with permission from the American Physical Society.*

orders, respectively. In particular, the solutions appearing in the diagrams correspond to ansatz 15 with $p_2 = p_3 = 1$, 16 with $p_2 = p_3 = 0$, 20 with $p_2 = p_3 = 1,\ p_4 = 0$, and finally 19 with $p_2 = p_3 = 1,\ p_4 = p_5 = 0$. For ansatz 20, the value of p_5 is not important since all the found solutions have $B_3 \approx 0$.

As expected, the structures of the phase diagrams for the different $SU(2)$ invariant points are exactly the same. The only difference lies in the static spin structure factor of the LRO phases since the spin orientations are changed by the gauge transformation. We compute structure factors using the methods described in appendix A.2 to compare the orders at different DM angles and spin values. In Figure 3.7, we report the SSF at $\phi = 0, 2\pi/3$ for specific points in the phase diagram in the regular LRO phases. These patterns coincide with the classical predictions for the respective regular orders.

Let us now discuss the phase diagrams for $\phi = 0$, Figure 3.6a. As expected, quantum effects become more relevant for decreasing spin values and from a mostly

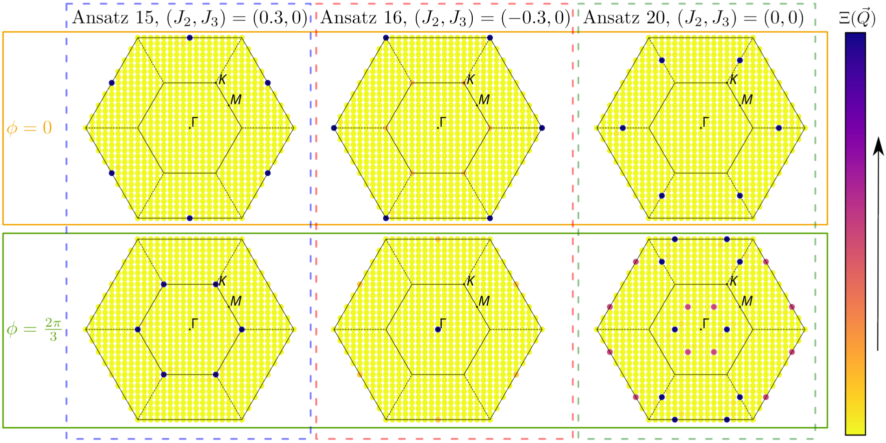

Figure 3.7: Spin structure factors of the orders found in Figure 3.6 for spin $S = 0.5$. Darker colors indicate a higher value of the structure factor. In the lower row we show the difference in SSF arising from the gauge transformation of Figure 3.1d. *Figure adapted from [3] with permission from the American Physical Society.*

LRO phase diagram at $S = 0.5$ we reach a completely SL one at $S = 0.2$. The phase diagrams follow quite closely the classical prediction for higher spin values while they differ from it at lower S. As already reported in [133], we also see that the $J_2 = J_3 = 0$ point has a chiral solution, which is a *cuboc-1* order at high spin values and turns into a chiral spin liquid for $S < 0.4$. More interestingly, for spin value 0.5 we find an additional solution to the ones reported in [133], which is the further neighbor version of ansatz 19, realizing a chiral spin liquid phase. It is remarkable that this phase remains gapped even at spin 0.5, a feature not observed in any SBMFT calculation on any lattice to the best of our knowledge. The region of the phase diagram where this new solution appears approximately coincides with the region identified in [158] and [2] as chiral spin liquid, Figure 3.8a. As mentioned above, a practice commonly used in SBMFT studies is to assume $S = (\sqrt{3} - 1)/2 \approx 0.366$ as an effective spin value. In this case, the phase diagram is much richer since it features $\mathbf{Q} = 0, \sqrt{3} \times \sqrt{3}$ and *cuboc-1* long-range orders together with three different kinds of spin liquids. In particular, with solutions 19 and 20 being both chiral since $\phi'_{A1} \neq 0, \pi$, we observe two different kinds of phases in the chiral spin liquid region identified in [2, 158]. The main difference in the form of the ansätze is p_1, thus, they have different unit cell size. By further decreasing the spin value, the chiral region increases and all phases turn towards gapped solutions.

We compute the spin structure factor for ansatz 19 and 20 for values of the parameters J_2, J_3, S where they appear as gapped SL, for comparison, in Figure 3.8b. For ansatz 20 at $J_2 = J_3 = 0$ and $S = (\sqrt{3} - 1)/2$, the structure factor is more smeared out with the peaks remaining at the positions of the LRO ones, as can be seen by comparing it with the top right structure factor of Figure 3.7. More interesting is the case of ansatz 19, where the structure factor shows a smeared pattern with peaks around the position expected for $\mathbf{Q} = 0$, as reported in the top left SSF of Figure 3.7. This is not surprising since the value of $\phi'_{\mathcal{A}_1}$ of ansatz 19 is around 0.3, and this ansatz coincides with 15 when $\phi'_{\mathcal{A}_1} = 0$ as shown in Table 3.1.

We finally study the case with a finite offset of the DM value from the $SU(2)$ invariant point. In particular, we consider a small phase $\phi = 0.05$ since we have seen how even a small value can strongly affect the phase diagram. We again take into account ansätze 15 to 20 in 3.1 and find a self-consistent solution, similar to the $SU(2)$-invariant case. The results are shown in Figure 3.6b. The solutions at finite DM angle belong to the same phases which were found above without DM interaction. In principle, the system is free to converge towards more general solutions since there are fewer symmetries (and in turn, constraints). Nevertheless, we find that all solutions which converge to a saddle point in the energy are more symmetric than their original Hamiltonian. In particular, we notice that there are no solutions with $|\mathcal{A}_2| \neq |\mathcal{A}'_2|$ or $|\mathcal{B}_2| \neq |\mathcal{B}'_2|$. This behavior can actually be expected from the choice of DM interaction (3.3). In fact, with the second nearest-neighbor phase being equal to zero, we could have considered the R_6 symmetry in the PSG construction to be valid at the second-nearest neighbor level, yielding a constraint for these amplitudes.

We notice that the $J_2 = J_3 = 0$ point remains $\sqrt{3} \times \sqrt{3}$ ordered up to much lower spin values with the introduction of the DM interaction. Also, the SL region is reduced greatly in general, as is evident from the two plots at $S = (\sqrt{3} - 1)/2$. As argued in 3.4.2, this tendency to favor in-plane configurations and reduce quantum fluctuations is expected in the presence of DM interactions. The results of this section show that the phases need to be kept close to the $SU(2)$ invariant points for spin liquid ground states to appear [181].

3.4.4 Discussion

Finally, we explored the phase diagram of the Heisenberg model on the kagome lattice taking into consideration further neighbor exchange and Dzyaloshinskii–Moriya interactions using Schwinger boson mean-field theory. Through the projective symmetry group approach, we classified all possible chiral and symmetric ansätze of the model both with and without DM interactions. Then, we employed Schwinger boson mean-field theory to compute the ground state of the model across a wide range of parameters. We first studied how uniform DM interactions affect the ground states in the nearest-neighbor kagome model. We find that the uniform DM pattern destabilizes the *cuboc-1* order and CSL at their respective effective spin values for even smaller finite DM angle than in the staggered case. This hints at a limited stability of potential spin liquid phases in TMD moiré bilayers away from the $SU(2)$ symmetric point, consistent with a functional renormalization group study on the triangular lattice [181].

We then investigated the model at the $SU(2)$ symmetric points including second and third neighbor interactions. The SBMFT accurately predicts the same phase boundaries for these points that can be related by local spin rotations in the xy plane. Furthermore, it correctly captures the different coplanar magnetic orders related by this gauge transformation, e.g. the two vector chiralities of the $\sqrt{3} \times \sqrt{3}$ and the in-plane ferromagnet. Regarding spin liquids, surprisingly, we found a chiral spin liquid close to the $J_2 = J_3$ line that remains stable up to a spin of $S = 0.5$, described by an ansatz that had previously not been considered. This is, to the best of our knowledge, the first time a spin liquid in SMBFT has been reported at such a high value of the spin. It appears around the region in which the CSL had been detected in DMRG simulations [2, 158] and could indicate an exceptional stability of this state. An open question is the relation of this CSL, which had been reported in the nearest-neighbor model in Ref. [105], to the one of the quantum disordered version of the *cuboc-1* state that emerges next to it for sufficiently small spin values.

Finally, we added DM interactions away from the $SU(2)$ symmetric point also in the J_1-J_2-J_3 model and found that the spin liquids quickly destabilize in analogy with the nearest neighbor system. Additionally, the coplanar orders are favored over the chiral *cuboc-1* state. Although the symmetry of the Hamiltonian has been reduced from $SU(2)$ to $U(1)$, we still only find magnetically ordered states with a classical analog among the regular magnetic orders of $O(3)$ symmetric Hamiltonians [180, 182].

Overall, we can conclude that the mean-field calculations of the phase diagrams qualitatively agree well with numerically exact DMRG results in parameter regimes where the latter have been performed and for the phases that can be captured by the Schwinger boson ansatz. The spin value of $S = (\sqrt{3} - 1)/2 \approx 0.366$ that is motivated by setting the onsite spin fluctuations equal to the quantum mechanical value, in particular predicts comparable parameter values for the transition lines between long-range orders and spin liquids. We thus demonstrated that SBMFT is an excellent approach to narrow down a large parameter space to regions that can potentially host spin liquid ground states on extended kagome lattice models, without the need to immediately resort to numerically more expensive methods. This might be of great use especially in the rapidly evolving understanding of the microscopic description of TMD moiré bilayers [183, 184].

Finally, we established that a variety of magnetic phases can be realized in an effective spin model on the kagome lattice which describes TMD bilayers at a filling of $3/4$ holes or electrons. In particular, the chiral spin liquid as well as the kagome spin liquid can emerge for experimentally realistic parameters (see Figure 3.8), in addition to several magnetically ordered phases. Moreover, the tunability of TMD moiré systems allows for a systematic search of elusive spin liquid physics, and as such it opens up a promising new direction in the search of highly entangled quantum matter.

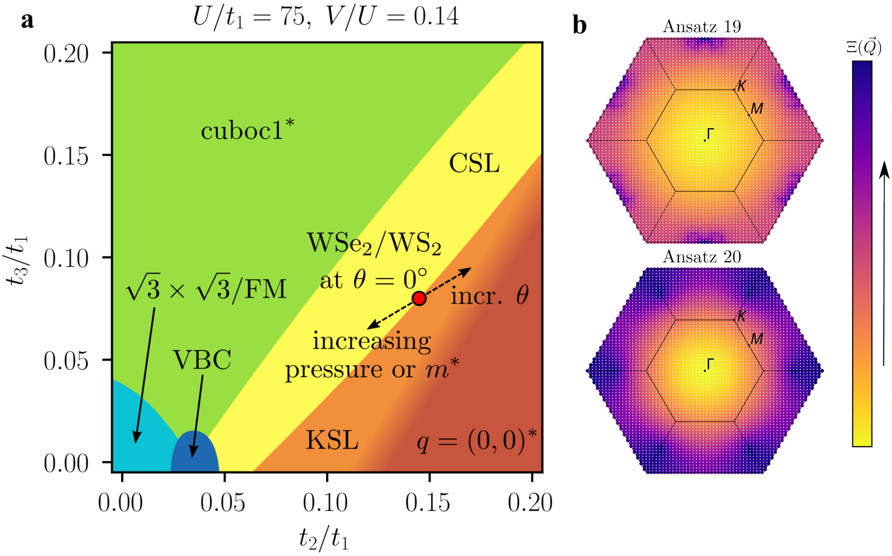

Figure 3.8: **a**, Ground state phase diagram evaluated with DMRG of the effective spin model (3.2) for $U/t_1 = 75$ and $V/t_1 = 10.5$ – corresponding to the interactions for $\varepsilon \approx 9.5$ in WSe$_2$/WS$_2$ at $\theta = 0°$ – as a function of t_2/t_1 and t_3/t_1. The appearing phases are the chiral spin liquid (CSL), the kagome spin liquid (KSL) connected to the ground state of the nearest-neighbor Heisenberg Hamiltonian, a valence bond crystal (VBC), and cuboc1*, $q = (0,0)^*$ and $\sqrt{3} \times \sqrt{3}$/FM -ordered phases. The $\sqrt{3} \times \sqrt{3}$ and ferromagnet are energetically degenerate. The red dot indicates the t_2/t_1 and t_3/t_1 values for WSe$_2$/WS$_2$ at $\theta = 0°$. Arrows show how this point would shift qualitatively when tuning twist angle, pressure or changing the effective mass by a different material choice. **b**, Spin structure factors of ansätze 19 and 20 in a gapped spin liquid solution. Ansatz 19 is computed at $J_2 = 0.06,\ J_3 = 0.02,\ \phi = 0$ and spin $S = 0.5$, ansatz 20 instead at $J_2 = 0,\ J_3 = 0,\ \phi = 0$ and spin $S = (\sqrt{3} - 1)/2$. *Panel* **a** *adapted from [2] under the Creative Commons BY 4.0 license. To view a copy of this license, visit https://creativecommons.org/licenses/by/4.0/. Panel* **b** *adapted from [3] with permission from the American Physical Society.*

Part II

Quantum Simulators

CHAPTER 4

Hamiltonian Quenches for Ground State Preparation

4.1 Introduction

The study of Hamiltonian systems in solid state platforms is always constrained to practical realizations and by the limitations of material properties. The possibility to create spin systems with tunable interactions is one of the reasons quantum simulators are regarded as the best platform to study extreme quantum systems [20]. With quantum simulators, we are provided with the necessary tools to explore quantum phenomena on a macroscopic scale, with applications ranging from quantum chemistry to quantum computation.

The main interest of this thesis is the study of quantum spin Hamiltonians, a formidable task which thanks to quantum simulators can be tackled by a close parallelism between theory and experiments. As already described in chapter 3, one can find a multitude of interesting phases with inherent quantum properties due to the strongly coupled nature of these models. In this chapter, I will describe a part of the work done in collaboration with the Google Quantum AI division [4], in which we studied the experimental realization of the XY model on a square lattice of up to 69 superconducting qubits. In particular, I will use this chapter to introduce the experimental setting and describe the capabilities of transmon qubits to study quantum spin systems. In this work, we employed a hybrid analogue-digital technique to *ramp* the state of the system from an antiferromagnetic Néel state into the XY phase (Figure 4.1a-b). We can already see that a multitude of phases and mechanisms will play a role in the description of this system. When a quantum system is swept through a quantum critical point (QCP), the variation of the sweep rate can allow

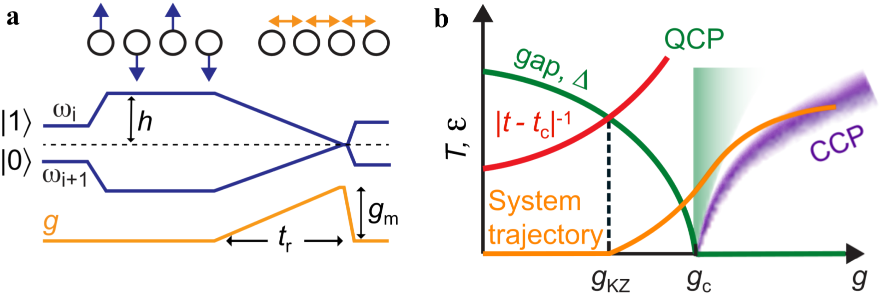

Figure 4.1: **a**, Experimental schematic of qubit frequencies (blue) and coupling (yellow). Details of the ramp and model parameters are discussed in section 4.2. **b**, Phase diagram. Dynamics become diabatic (dashed black) with increased temperature (T) when inverse remaining time (red) exceeds gap (green; $\Delta \propto |g - g_c|^{\nu z}$). QCP and CCP denote the quantum and classical critical points, respectively. This phase diagram is discussed in section 4.3.2. *Figure adapted from [4] under the Creative Commons BY 4.0 license. To view a copy of this license, visit https://creativecommons.org/licenses/by/4.0/.*

for accessing markedly different paths through phase space and correspondingly distinct coarsening behavior. The behavior of states following these types of ramps falls under the description of the celebrated Kibble-Zurek mechanism [185–188], which predicts the correlation length ξ of the final state to follow a universal power-law scaling with the ramp time t_r [189–192]. Furthermore, we know that the gapless XY phase hosts a finite temperature Kosterlitz-Thouless phase transition [193] from an *ordered* phase of bound vortex-anti-vortex pairs into a *disordered* phase where vortices are free to proliferate and scatter. We prepare and characterize states of a two-dimensional XY magnet with a broadly tunable energy density, enabling the exploration of the interplay between quantum and classical critical behavior across the rich phase diagram of our system.

In this chapter, I describe some of the results of [4], in which my contribution was the interpretation of the Kibble-Zurek predictions and of the theoretical comparison with MPS simulations. In section 4.2, I describe the platform in which the experiment was performed, i.e. how superconducting qubits work and the mixed *analog-digital* technique which was employed to time-evolve the state and perform the measurements. In section 4.3, I characterize the properties of the XY phase and show the results of [4] in comparison with the theoretical predictions. I then give an overview of the Kibble-Zurek mechanism and present the predictions and measurements for our system.

The results presented in this chapter also serve the purpose of setting the stage for describing the experimental capabilities of quantum simulators. These will be used as starting point for the discussion in next chapter 5, where I lay down a description of magnons in the 2D XY model by means of a spin-wave expansion in order to characterize some of the quantities one can imagine to extract from these systems.

4.2 Quantum Simulation

Ever since the first proposal of Richard Feynman to use quantum computers to simulate physics [20, 194], the amount of attention to quantum-based technologies has only been growing. A particularly prominent platform for scalable quantum technology are superconducting circuits used for constructing qubits. These systems are fascinating since they exhibit microscopic behavior, i.e. quantum effects, while being macroscopic in size, and the experimental realization of this was awarded the Nobel prize in physics in 2025 [195]. In this part of the thesis, we will focus on so-called *transmon* qubits realized by the Google Quantum AI team (see a picture of the Sycamore processor in Figure 4.2a). These chips were already used to propose quantum advantage [196] as well as many other milestones of quantum computing.

4.2.1 Transmons

A superconducting qubit can be understood using basic circuit analysis [197]. When we talk about a superconducting qubit, we usually refer to the two lowest energy levels of a superconducting circuit. Although this topic has been thoroughly reviewed in the literature -and a full treatment lies beyond the main scope of this thesis -I will briefly introduce the main ideas behind how transmon qubits work and how they can be coupled to one another.

Let us start by considering a superconducting circuit. In such a circuit, all components conduct current without electrical resistance. Besides the usual *linear* circuit elements, namely the capacitor and the inductor, a key ingredient is the *Josephson junction*. This element behaves as a *non-linear* inductive component and is essential because it introduces *anharmonicity* into the system. To understand why this is important, recall that a simple LC circuit, when quantized, becomes a harmonic oscillator with equally spaced energy levels (see left panel of Figure 4.2c). In that case, if we try to drive a transition between the first two energy levels, we will also unintentionally drive transitions to higher levels, since all the transition frequencies are identical. The Josephson junction, represented by the boxed ‘x’ element in circuit diagrams, breaks this symmetry: it modifies the potential energy in a way that makes the energy levels unequally spaced (right panel of Figure 4.2c). This anharmonicity allows us to address only the two lowest levels and to treat them as an effective two-level quantum system -a qubit. In practice, for the system to operate reliably as a qubit, the anharmonicity must be larger than the bandwidth of the control pulses used to drive transitions. In other words, the energy difference between successive levels must exceed the amplitude of the driving field, ensuring that higher levels remain unpopulated during qubit operations.

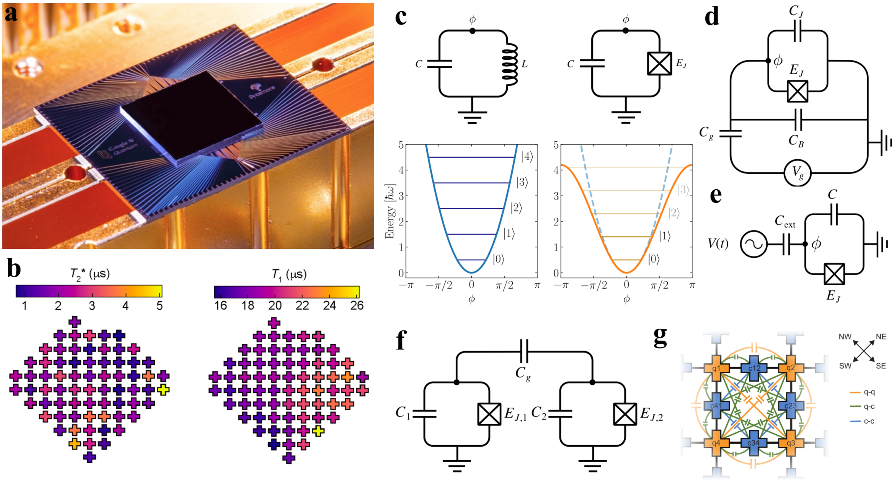

Figure 4.2: **a**, Picture of the Sycamore chip. **b**, Ramsey dephasing (T_2^*) and photon relaxation (T_1) times across the qubit grid used in [4]. **c**, *Left panels*: Circuit of an LC oscillator with inductance L, capacitance C and phase of the superconducting island ϕ. The energy potential of a quantum harmonic oscillator, as can be obtained by an LC circuit, has equidistant energy levels. *Right panels*: Josephson junction qubit circuit, where the linear inductor is replaced by a nonlinear Josephson junction. The potential is now a sinusoidal, yielding non-equidistant energy levels. **d**, Circuit of a transmon qubit. **e**, Microwave driving coupled trough a capacitor to a qubit. **f**, Schematics of capacitive coupling between qubits. **g**, Schematic of underlying coupling pathways in the device used in [4]. In addition to capacitive coupling between neighboring qubits (orange) and couplers (blue), there are also diagonal next-nearest-neighbor couplings.*Panel* **a** *adapted from [196]. Reproduced with permission from Springer Nature. Panels* **c** *to* **f** *adapted from [198] under the Creative Commons BY 4.0 license. To view a copy of this license, visit https://creativecommons.org/licenses/by/4.0/. Panels* **b** *and* **g** *adapted from [4] under the Creative Commons BY 4.0 license. To view a copy of this license, visit https://creativecommons.org/licenses/by/4.0/.*

Transmon qubits, introduced in 2007 [199,200], are one of the most widely used implementations of this concept. Their circuit design, illustrated in Figure 4.2d, includes additional capacitors that increase the total capacitance of the circuit. This adjustment makes the qubit less sensitive to charge noise while still preserving enough anharmonicity to perform coherent quantum operations effectively.

Single-qubit control can be achieved by capacitively coupling a transmon to a microwave drive (see Figure 4.2e). This setup allows us to perform arbitrary single-qubit rotations by tuning the frequency and phase of the external microwave signal to match the qubit transition. In practice, this means that by choosing the appropriate drive parameters, one can rotate the qubit state on the Bloch sphere around any desired axis.

To realize multi-qubit operations, two or more transmons can be coupled together through a capacitive link (see Figure 4.2f). Unlike in the single-qubit case, this coupling cannot be switched on and off directly; instead, the interaction strength is controlled by tuning the two qubits in and out of resonance. When the qubits are brought into resonance, an effective exchange of excitations occurs, allowing the implementation of two-qubit gates such as the $\sqrt{i\text{SWAP}}$ gate.

In more advanced architectures, such as the one used in Ref. [4], the interaction between qubits is mediated by additional *coupler qubits*. As illustrated in Figure 4.2g, these coupler qubits (shown in blue) connect the physical qubits (shown in orange) via capacitive coupling. This design provides greater flexibility in engineering the interaction strengths and connectivity between qubits. However, due to the presence of multiple couplings, corrections must be taken into account when determining the effective single-qubit frequencies. These corrections can introduce residual interactions between more distant (next-nearest-neighbor) qubits, which must be carefully calibrated.

Up to this point, we have treated the qubits as ideal, isolated quantum systems. In reality, however, it is nearly impossible to completely decouple them from their environment. This unavoidable coupling leads to energy loss and decoherence, limiting the time during which reliable quantum operations or simulations can be performed. Two main types of relaxation processes characterize this behavior: *longitudinal* and *transverse* relaxation. The longitudinal relaxation time, denoted by T_1, describes the decay of population along the qubit's quantization axis due to energy exchange with the environment (often referred to as energy relaxation). The transverse relaxation time, denoted by T_2, characterizes the loss of phase coherence in a superposition state. It results both from energy relaxation and from pure dephasing processes, and is often referred to as the Ramsey dephasing time.

Figure 4.2b shows the measured T_1 and T_2 times for the experiment reported in Ref. [4], providing an idea of the timescales available in such devices. The data indicate that the qubits are not perfectly homogeneous across the processor, with Ramsey dephasing times generally exceeding longitudinal relaxation times. The median values reported are $T_1 = 2.0\ \mu s$ and $T_2 = 18.8\ \mu s$, respectively, which define the operational window for coherent quantum dynamics in this platform.

4.2.2 Analog-Digital Approach

The quantum simulator employed in Ref. [4] is capable of implementing universal entangling gates through pairwise interactions between qubits. When all couplers are activated simultaneously, the same platform enables high-fidelity analogue simulation of a $U(1)$-symmetric spin Hamiltonian (Figure 4.3a). The exceptionally low analogue evolution error -historically difficult to achieve with transmon qubits because of correlated cross-talk -is made possible by a newly introduced and scalable

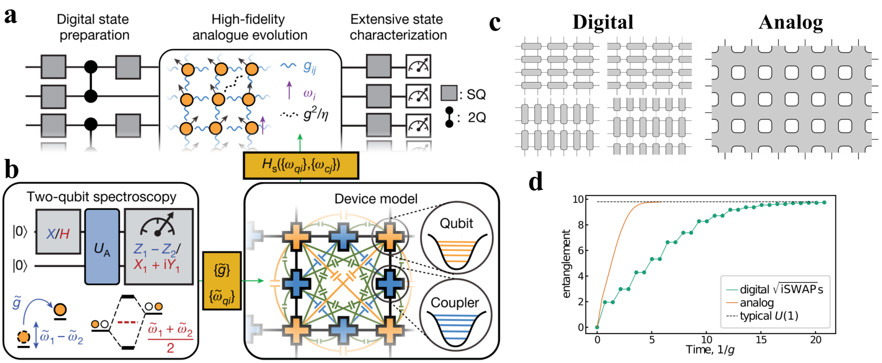

Figure 4.3: **a**, Scheme of the analog-digital platform combining analog time evolution and digital gates for state preparation and measurement. **b**, Schematic of the analog calibration scheme. Swap and single-photon spectroscopy is used to extract dressed coupling rates ($\{\tilde{g}\}$) and qubit frequencies ($\{\tilde{\omega}_{qi}\}$) of two-qubit analogue evolution (U_A), which are converted to bare qubit and coupler frequencies ($\{\omega_{qi}\}$, $\{\omega_{cj}\}$) through detailed device modeling. The bare frequencies allow for establishing the device Hamiltonian of the full system, which is finally projected to a spin Hamiltonian. **c**, Schematic comparison between digital and analog time evolution. **d**, Comparison of entanglement growth in the digital and analog cases for a random product state. The points show entanglement entropy in the digital case after application of each layer in the ABCD gate pattern (**c**). The black dashed line shows the typical entanglement in the $U(1)$ case of a 30-qubit system. *Panels* **a**, **b** *and* **d** *adapted from [4] under the Creative Commons BY 4.0 license. To view a copy of this license, visit https://creativecommons.org/licenses/by/4.0/.*

calibration protocol.

Operating a network of coupled transmons as a high-fidelity analog quantum simulator requires precise knowledge of the underlying many-body spin Hamiltonian, H_s. This Hamiltonian depends on the *bare* transition frequencies $\{\omega_{q_i}\}$ and $\{\omega_{c_j}\}$ of the qubits q_i and couplers c_j, respectively. In practice, however, experimental calibration provides access only to the *dressed* frequencies. These dressed quantities differ from the bare ones because they are modified by hybridization with neighboring qubits and couplers. As a result, frequencies determined in local (isolated) calibrations often shift when the full device is operated, leading to discrepancies between the intended and realized Hamiltonian parameters. This challenge has complicated the characterization of large-scale superconducting qubit arrays. Earlier experimental studies [201, 202] either suffered from significant systematic errors or relied on multi-parameter optimization procedures, which become increasingly difficult to scale with system size. More recent approaches, such as Hamiltonian learning techniques [203, 204], can mitigate some of these limitations, but they remain sensitive to Hamiltonian ramps, noise, and errors in state preparation and measurement

(SPAM).

Here was used a scalable calibration protocol that achieves low systematic error by explicitly determining the bare frequencies of both qubits and couplers. As illustrated in Figure 4.3b, the protocol begins with two-qubit calibration measurements-specifically, single-photon spectroscopy and swap spectroscopy-which are inherently robust against ramps and SPAM errors. These measurements yield the effective coupling $\tilde{g}$ and the dressed qubit frequencies $\{\tilde{\omega}_{q_i}\}$ for every qubit pair. Was then employed a detailed modeling of the underlying device physics to convert these dressed parameters into the bare frequencies $\{\omega_{q_i}\}$ and $\{\omega_{c_j}\}$. Using these bare quantities, it is possible to construct a high-dimensional device Hamiltonian, $H_{\mathrm{d}}(\{\omega_{q_i}\}, \{\omega_{c_j}\})$, which is subsequently projected onto an effective spin Hamiltonian

$$\mathcal{H}_s = \sum_i \omega_i n_i + \sum_{\langle i,j \rangle} \frac{g_{ij}}{2} \Big(X_i X_j + Y_i Y_j \Big) + \mathcal{O}\big(g^2/\eta\big) \tag{4.1}$$

In this reduced model, the on-site potentials ω_i and the nearest-neighbor coupling strengths $|g_{ij}| \approx g$ are tunable parameters. Importantly, the coupling strength g is much smaller than the qubit anharmonicity $\eta \gg g$, ensuring that the system remains within the single-excitation subspace with photon occupation numbers $n_i = 0, 1$. In this regime, the operators X_i and Y_i act as Pauli matrices on the corresponding qubit subspace. The resulting Hamiltonian (4.1) thus belongs to the universality class of an XY model with on-site z-fields.

A natural consequence of hybridization in this system is that H_{s} includes not only nearest-neighbor hopping terms but also density-density interactions and next-nearest-neighbor couplings. These additional terms scale as $\mathcal{O}(g^2/\eta)$ and are at least five to ten times smaller than the primary coupling g.

To conclude this section and transition toward the results, we now compare the time evolution realized in digital and analog settings (see Figure 4.3c). In the digital case, time evolution is implemented through discrete unitary gates, which naturally introduces Trotter errors due to time discretization. Figure 4.3d presents a comparison of the entanglement entropy obtained with the two approaches. Specifically, we analyze the growth rate of the bipartite von Neumann entropy in both digital and analog evolutions. The system under consideration is a two-dimensional 5×6 lattice with open boundary conditions, which we partition into two subsystems of 15 qubits each along the shorter direction. In the analog simulation, we evolve a random product state under a pure XY Hamiltonian with coupling constants g_{ij}. In the digital simulation, we apply a period-4 ABCD sequence of $\sqrt{\text{iSWAP}}$ gates, following the order left–up–right–down, as illustrated in the left panel of Figure 4.3c. As shown in Figure 4.3d, both approaches lead to entanglement entropy growth consistent with the theoretical quarter-circle bound. Notably, the analog implementation reaches this bound nearly four times faster than the digital one.

4.3 Correlations and Ramp Dynamics

Preparing entangled ground states in quantum simulators poses a major experimental challenge, primarily because any excess energy introduced into the system is extremely difficult to dissipate. In other words, cooling a quantum system to its true ground state is inherently hard. A practical strategy to approach the ground state of a target Hamiltonian is to begin from the ground state of a different, simpler system that can be prepared efficiently, and then adiabatically vary the system parameters until the desired Hamiltonian is reached. Such a ramp is ideally *adiabatic* only if no phase transition is crossed during the evolution. At a phase transition, the energy gap closes, and the system can no longer remain in its instantaneous ground state, leading to excitations being created on top of the ground state.

We now define the Hamiltonian of our system, consisting of a square lattice of superconducting qubits. To initialize the system in a well-defined and easy to prepare configuration, we introduce a staggered magnetic field h_z that stabilizes the antiferromagnetic Néel state as the initial ground state. During the adiabatic ramp, this field is gradually reduced while the XY coupling strength g_{XY} is increased, driving the system toward the interacting regime of interest (see the ramp profile in Figure 4.1a). The corresponding Hamiltonian is given by

$$H = \frac{g}{2} \sum_{\langle i,j \rangle} \left(X_i X_j + Y_i Y_j \right) + \tilde{h} \sum_i (-1)^{\# i} Z_i, \tag{4.2}$$

where $(-1)^{\# i} = \pm 1$ distinguishes the two sublattices of the square lattice, and $\langle i, j \rangle$ indicates a summation over nearest-neighbor pairs. We use here the notation of X_i, Y_i, and Z_i denoting the Pauli matrices acting on qubit i.

4.3.1 Results

We now turn to the exploration of the rich phase diagram of the XY model. As illustrated in Figure 4.1b, this system is expected to exhibit both a quantum phase transition in the ground state and a classical Kosterlitz–Thouless (KT) transition at finite temperature [193]. To prepare low-energy states of an antiferromagnetic XY magnet, we first apply a staggered z-field of magnitude $\tilde{h}/(2\pi) = 7.5$ MHz and initialize the qubits in the z-basis Néel state. This choice maximizes the energy with respect to the XY interaction term in (4.2). We then perform an adiabatic ramp in which the staggered field is gradually reduced while simultaneously turning on ferromagnetic couplings of magnitude $g/(2\pi) = 10$ MHz over a duration t_r (Figure 4.1a). Following this protocol [205], the system evolution effectively realizes an antiferromagnetic XY model with a staggered field, initialized close to its ground state.

During an ideal adiabatic ramp, the system would cross a quantum phase transition from a paramagnetic phase with unbroken $U(1)$ symmetry to the XY-ordered

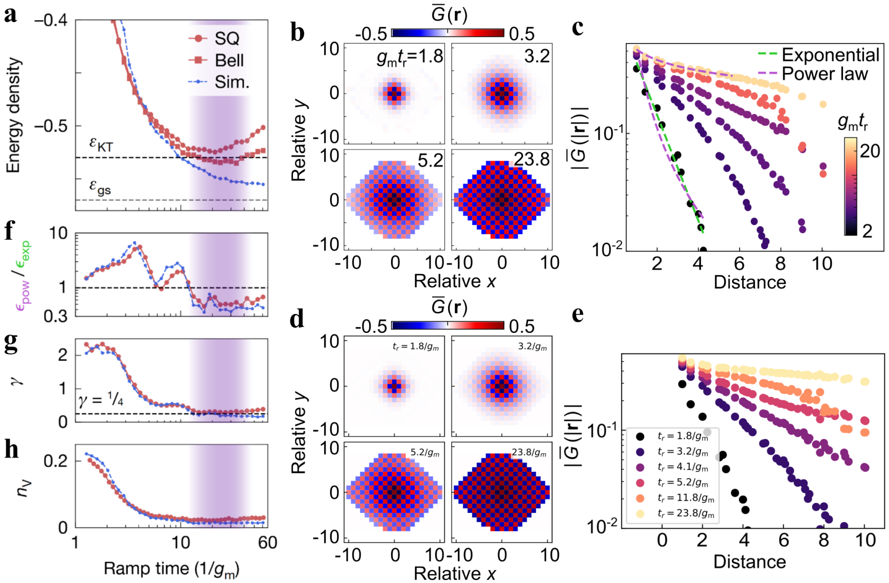

Figure 4.4: **a**, The final energy density approaches the ground state value (ϵ_{gs}, grey) and Kosterlitz-Thouless transition value (ϵ_{KT}, black) as t_r is increased. Red circles and squares indicate single-qubit (SQ) and Bell basis measurements, respectively. Blue, MPS simulation. Purple shading indicates where classical critical behavior is expected. **b** and **d**, Average correlation, $G(r)$ found from averaging $\left(\langle X_i X_j + Y_i Y_j\rangle - \langle X_i\rangle\langle X_j\rangle - \langle Y_i\rangle\langle Y_j\rangle\right)/2$ over all pairs i, j separated by r, measured at various t_r in experiment (**b**) and in MPS simulations (**d**). **c** and **e**, Decay of radially averaged correlations in experiment (**b**) and MPS simulations (**d**). Green and purple curves show examples of exponential and power-law fits, respectively, performed up to a distance of 6 to avoid finite-size effects at longer distances. Error bars represent one standard deviation estimated from bootstrapping ($N_{reps} = 5 \times 10^4$ repetitions). **f**, Ratio between r.m.s. errors from power-law and exponential fits ($\epsilon_{\text{pow}}/\epsilon_{\text{exp}}$) decreases for $g_m t_r > 15$. **g**, Power-law exponent, γ, approaches expected value at Kosterlitz-Thouless transition (1/4; black line). **h**, Vortex density proxy, n_V, decreases to minimum of 2×10^{-2}. *Figure adapted from [4] under the Creative Commons BY 4.0 license. To view a copy of this license, visit https://creativecommons.org/licenses/by/4.0/.*

phase at a time $t_c \sim 0.45 t_r$, corresponding to $\tilde{h}_c/g_c \sim 1.8$. After completing the ramp, the qubits are quickly returned to their idle frequencies and correlation functions are measured. Figure 4.4a shows the ramp-time dependence of the average energy density

$$\epsilon = \frac{1}{n_B} \sum_{\langle i,j\rangle} \frac{\langle X_i X_j + Y_i Y_j\rangle}{2},$$

averaged over $n_B = 110$ bonds ($N_q = 65$) and corrected for readout errors. As t_r increases and the evolution becomes more adiabatic, the energy density decreases toward the theoretically predicted ground-state value $\epsilon_{\mathrm{gs}} = -0.56$, as well as the predicted Kosterlitz-Thouless transition energy $\epsilon_{\mathrm{KT}} = -0.53 \pm 0.01$ (gray and black lines in Figure 4.4a, respectively). The final states are strongly thermalized [4], allowing ϵ to serve as an indicator of the effective temperature. To correct for photon decay errors, digital entangling gates are applied at the end of the circuit to map each qubit pair to the Bell basis, enabling post-selection with respect to photon number conservation (red squares). This procedure yields an improved energy density of $\epsilon = -0.53 \pm 0.01$, approximately equal to the KT transition point. The remaining difference from the MPS-simulated energy (blue dots) is attributed to dephasing effects, which this technique does not correct.

Energy alone does not reveal the effects of thermalization, so we next examine spatial correlations. Figure 4.4b shows the measured average correlation $G(r)$ between pairs of qubits separated by distance r. Antiferromagnetic ordering is clearly observed, with both the range and magnitude of correlations increasing for longer ramp times, consistent with lower-energy states. The radial average of $G(r)$ is then analyzed using both exponential and power-law fits to extract the correlation length ξ and to characterize the scaling behavior (Figure 4.4d). The comparison with MPS-simulated correlations (Figure 4.4d-e) is particularly striking, showing how well the analog time evolution is working.

For short ramp times, correlations decay exponentially, as expected for states above the KT transition where freely proliferating vortices destroy long-range order. For longer ramp times, the decay is better described by a power law (Figure 4.4f), evidenced by a significant decrease in the ratio of root-mean-square errors between power-law and exponential fits, reaching values well below 1 near $g_m t_r = 25$, where the energy is also near its minimum. This behavior is consistent with the classical critical regime, in which free vortices become entropically unfavorable and are replaced by bound vortex-antivortex pairs, leading to algebraically decaying correlations. In the regime with good power-law agreement, the extracted exponent is $\gamma = -0.29$ (Figure 4.4g), close to the universal KT prediction of $1/4$ [206].

To further substantiate this interpretation, four-qubit correlators are measured to construct the Swendsen proxy for vortex density [207]:

$$n_V = \frac{1}{4N_p} \sum_{i=1}^{N_p} \big(1 - X_{i1}X_{i3} - Y_{i1}Y_{i3}\big)\big(1 - X_{i2}X_{i4} - Y_{i2}Y_{i4}\big),$$

where $i = 1, \ldots, N_p$ labels the plaquettes and $\{i1, i2, i3, i4\}$ are the vertices of each plaquette. Indeed, n_V decreases rapidly with increasing t_r (Figure 4.4h), reaching a minimum of 2×10^{-2} in the low-energy regime.

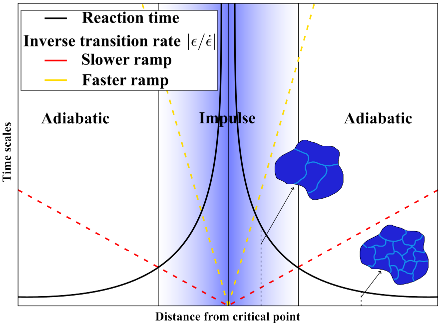

Figure 4.5: The relaxation time τ and the inverse transition rate $|\epsilon/\dot{\epsilon}|$ vary with the dimensionless distance ϵ from the critical point. They coincide at $\hat{\epsilon}_+$ and $\hat{\epsilon}_-$, which indicate the crossovers between the impulse and adiabatic regimes of the time evolution. Close to the critical point the system becomes more coarse grained, with characteristic dimension of domains given by the correlation length.

4.3.2 Kibble-Zurek Mechanism and Deviations

The reason the system does not stay close to the ground state throughout the ramp is due to emergence of excitations when the system passes close to the critical point, in a process called Kibble-Zurek mechanism. The Kibble-Zurek (KZ) mechanism [40, 41] describes the dynamics of a system when it is driven across a second-order phase transition (PT). The mechanism uses scaling arguments to predict the state of the system after the transition, based on how critical quantities diverge near the PT [208].

Let us consider a system characterized by a dimensionless parameter

$$\epsilon = \frac{g - g_c}{g_c},$$

which measures the distance from the phase transition occurring at $g = g_c$. Close to the transition, the correlation length ξ diverges as

$$\xi \sim |\epsilon|^{-\nu},$$

where ν is the critical exponent associated with the divergence of correlations. Similarly, the relaxation time τ, which quantifies the system's ability to respond to external perturbations, diverges according to the dynamical critical exponent z:

$$\tau \sim \xi^z. \tag{4.3}$$

Suppose now that the system parameter ϵ is varied in time with a finite rate, corresponding to a quench of duration t_r:

$$\epsilon(t) = -\frac{t}{t_r}. \tag{4.4}$$

The central idea of the KZ mechanism is captured by the *Adiabatic-Impulse-Adiabatic (AIA)* approximation (see Figure 4.5). Initially, when the system is far from the critical point, it can follow the changing Hamiltonian adiabatically, remaining close to its instantaneous ground state. As the system approaches the phase transition, however, the relaxation time τ grows and eventually becomes longer than the timescale of the parameter variation. At this point, the system can no longer adjust and effectively *freezes* in its state.

For a quantum phase transition, the relaxation time is set by the inverse energy gap:

$$\tau \simeq \Delta^{-1}, \tag{4.5}$$

where the gap Δ closes near the critical point as

$$\Delta \sim |\epsilon|^{\nu z}. \tag{4.6}$$

The crossover from adiabatic to impulse dynamics occurs when the transition rate

$$\left|\frac{\dot{\epsilon}}{\epsilon}\right| = \frac{1}{|t|} \tag{4.7}$$

becomes comparable to the gap, $\Delta \sim |t/t_r|^{\nu z}$. This defines the characteristic Kibble-Zurek time

$$t_{KZ} \sim t_r^{\frac{\nu z}{1+\nu z}}. \tag{4.8}$$

Between $-t_{KZ}$ and t_{KZ}, the system is in the *impulse* regime, during which its state is effectively frozen. After t_{KZ}, the system resumes adiabatic evolution, with the frozen state at $\hat{\epsilon}$ acting as the initial condition for the next adiabatic stage. For sufficiently slow quenches (large t_r), the freeze-out occurs close to the critical point.

Using the scaling hypothesis of renormalization group theory, expectation values of observables in the frozen state can be related to powers of the correlation length $\hat{\xi}$ evaluated at $\hat{\epsilon}$. A commonly studied quantity is the density of quasi-particle excitations generated during the quench, which scales as

$$n_{\text{ex}} \simeq \hat{\xi}^{-d} \sim t_r^{-\frac{d\nu}{1+\nu z}}, \tag{4.9}$$

where d is the spatial dimension of the system. This scaling provides a direct prediction for the non-adiabatic excitations generated by crossing a quantum critical point at a finite rate.

In our specific case defined in (4.2), the system begins in an product state with antiferromagnetic correlations in z direction and is ramped into the gapless XY phase at a critical value of the coupling ratio $g/\tilde{h}$. This transition is analogous to the two-dimensional Mott insulator–superfluid transition [209] and belongs to the universality class of the three-dimensional (3D) XY model, with correlation length and dynamical critical exponents $\nu \sim 0.67$ and $z = 1$, respectively.

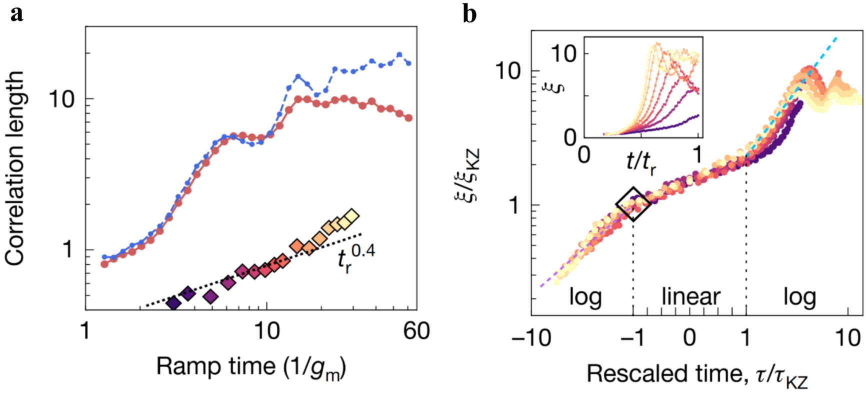

Figure 4.6: a, Correlation length increases with t_r. Both simulation results (blue) and experimental data (red) show substantially more superlinear growth than KZ predictions (dashed black). Diamonds, correlation lengths extracted at expected freezing point (**b**). **b**, Correlation length during the ramp, shown with and without rescaling (main and inset, respectively) and two-sided logarithmic axes for $|\tau| > \tau_{\text{KZ}}$. ξ_{KZ} is found from fitting $\xi(\tau = \tau_{\text{KZ}}) = \xi_0(\tau_{\text{KZ}}/t_r)^{-\beta}$ with $\beta = 0.9(1)$ (difference from $\beta = \nu = 0.67$ expected to be due to finite-size effects). Dashed colored lines show the theoretically expected scaling, $f(x) = |x|^{-\nu}$ with $\nu = 0.67$ for $x < -1$ (purple) and a heuristic $f(x) = x\eta$ with $\eta = 1$ for $x > 1$ (teal). The increase in ξ beyond the freezing point (diamond) causes deviation from KZ predictions. *Figure adapted from [4] under the Creative Commons BY 4.0 license. To view a copy of this license, visit https://creativecommons.org/licenses/by/4.0/.*

A key difference from the standard Kibble-Zurek (KZ) mechanism is that, in this case, the ramp ends inside a gapless phase rather than returning to a gapped phase. As a result, although the system is expected to freeze near the critical point, correlations can continue to grow [210–212]. Indeed, as shown in Figure 4.6a, the correlation length ξ reaches a maximum of ~ 10 at $g_m t_r = 25$, corresponding to the longest dimension of our lattice. At longer ramp times, we observe a slight decrease in ξ, attributed to qubit decoherence, as well as periodic oscillations that are also present in matrix product state (MPS) simulations and are likely due to finite-size effects.

Focusing on shorter ramp times, where these secondary effects are minimal and correlations display a clearer exponential decay, we find a strong deviation from the KZ-predicted power-law scaling, $\xi \sim t_r^{\nu/(1+\nu z)} \approx t_r^{0.4}$. Instead, ξ grows substantially faster than this prediction, with similar discrepancies observed in both experiment and simulation. We attribute this breakdown of KZ scaling to coarsening dynamics occurring beyond the expected freeze-out point [210, 212]. To illustrate this behavior more explicitly, we measure the correlation length along the Hamiltonian ramp (Figure 4.6b). According to KZ theory, the system should freeze at t_{KZ}, when the inverse gap becomes comparable to $|t - t_c|$. In contrast, our measurements show that ξ continues to grow beyond t_{KZ}, indicating that the system can further thermalize, resulting in a larger correlation length at the end of the ramp. To emphasize this point, we plot the experimentally measured correlation lengths at t_{KZ} in Figure 4.6a, which shows improved agreement with the KZ prediction.

Moreover, when rescaling the data as ξ/ξ_{KZ} versus $(t - t_c)/|t_{\mathrm{KZ}} - t_c| \equiv \tau/\tau_{\mathrm{KZ}}$, the curves collapse onto a common function $f(\tau/\tau_{\mathrm{KZ}})$. This collapse, consistent with predictions of universal coarsening dynamics [210, 212, 213], extends well beyond the quantum critical regime ($-\tau_{\mathrm{KZ}} < \tau < \tau_{\mathrm{KZ}}$), highlighting dynamical universality driven by coarsening.

We observe that the collapsed function behaves similarly to the theoretically predicted scaling, $f(x) \propto |x|^{-\nu}$ for $x < -1$, with minor deviations likely due to finite-size effects and small ξ. The ratio $f(1)/f(-1)$ is measured to be 2.3 ± 0.1. For $x > 1$, we heuristically find $f(x) \propto x$, reflecting the interplay between gapped and gapless modes, which is expected to differ from behavior in quantum Ising models.

CHAPTER 5

Theory of Magnons in the Quantum XY Model

5.1 Introduction

As was shown in the previews chapter, a hybrid analog–digital technique on a quantum simulator enables us to probe the state of a quantum spin Hamiltonian, Eq. (4.2). What we studied were measurements performed at a specific time at the end of the ramp, which do not yield information about the dynamical properties of the system, like the dynamical spin structure factor. Let us imagine we could probe probe these dynamical properties in quantum chips: to gain deeper insight into the system's dynamical properties, alongside an improved experimental setup, one would need precise theoretical predictions.

As a simple illustration of the properties we would want to study, let us consider the system of Eq. (4.2) in one spatial dimension. This represents a 'simple' 1D (nearest-neighbor) XY chain, which can be solved by mapping to free fermions by means of the Jordan-Wigner transformation, as detailed in Appendix B. Dynamical properties of the system can be studied by considering time and space resolved correlation functions, of the type

$$\langle \left[S_i^z(t), S_j^z(0) \right] \rangle \tag{5.1}$$

By changing the parameters of the Hamiltonian in a ramp analog to the one studied in the previous chapter (see Figure 4.1), we can access different properties of the system. Since the goal is the comparison with experimental results, I will consider a series of states realized in a ramp starting from an initial staggered field of $\tilde{h}_i = 15/(2\pi)$ MHz which is linearly decreased to 0 while at the same time ramping up

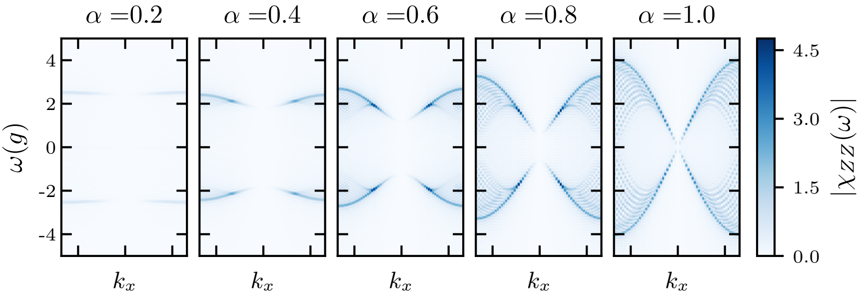

Figure 5.1: S^zS^z correlator (5.1) Fourier transformed in space and time for different stop ratios (5.2) for a 1D periodic chain of $N = 60$ sites. The correlator clearly follows the dispersion relation of the free fermions in the system (5.3).

the nearest neighbor coupling from 0 to the final value of $g_f = 10/(2\pi)$ MHz, as in Figure 4.1a. The intermediate states of the ramp are going to be defined by a stop ratio $\alpha \in [0, 1]$ as

$$\begin{cases} h = h_i(1-\alpha) \\ g = \alpha g_f \end{cases} \tag{5.2}$$

We can then look at the Fourier transformed S^zS^z correlator (5.1) (see Figure 5.1) to see that the what we are actually probing is the dispersion relation of the fermions in the 1D system. As derived in Appendix B, the dispersion relation is

$$\omega(k_x) = \sqrt{\tilde{h}^2 + 4g^2 \cos {k_x}^2} \tag{5.3}$$

This dispersion starts out as gapped at $k_x = 0$ and becomes gapless at the critical point $\alpha = 1$ (or equivalently $\tilde{h} = 0$). This example shows us how to get insights on the particle content and the dynamical properties of the system.

In 2D the situation is markedly different, first of all because the model is no-longer integrable and also because during the ramp we are crossing a quantum phase transition. In order to draw a comparison with theoretical expectations, one can access different observables by using MPS simulations and exact diagonalization. On the other hand, if we want to draw a more intuitive description of correlators and magnons in this system, the best way to do it is by employing mean-field theory. In the case at hand, we will consider the spin Hamiltonian (4.2) including also anisotropy Δ and second nearest neighbor exchange

$$\mathcal{H} = \sum_{\gamma \in \{1,2\}} J_\gamma \sum_{\langle i,j \rangle_\gamma} \left(S_i^x S_j^x + S_i^y S_j^y + \Delta_\gamma S_i^z S_j^z \right) + h \sum_i (-1)^{\#i} S_i^z \tag{5.4}$$

We will use here the spin notation, with the conversion to (4.2) being $g = 2J_1S^2$ and $\tilde{h} = hS$. There are different mean-field decouplings which can be used to study this model. In chapter 3, I showed that Schwinger boson mean-field theory is good to describe the spin liquid states in the Heisenberg model on the kagome lattice. In the case at hand (5.4), a more suited mean-field theory which should be able in particular to give a good description of the excitations of the system (magnons) is the *linear spin wave* theory [42, 214, 215].

In the following chapter, I will start by describing the Holstein-Primakoff (HP) transformation in section 5.2. The key point in the procedure is the choice of an appropriate quantization axis, which leads us to the necessity to find the classical magnetization patterns for different Hamiltonian parameters J_γ, δ_γ and h. In section 5.3, I describe the derivation of space and time resolved correlators. In particular, I show how we derived open boundary results that can be compared with the experimental setup in quantum simulators [4]. Open boundaries in the system introduce a multitude of differences with respect to the periodic case which need to be addressed in order to get meaningful results, given that the system dimensions experimentally available rely to large extent on it. Finally, in section 5.4, I use the derived mean-field Hamiltonian to explore the properties of the magnon population. I derive a consistent theory of magnon scattering and decay when the system is placed in a thermal bath by considering all the relevant scattering processes. This study yields many predictions for the magnon properties which could be relevantly tested in a quantum simulator.

The work reported in this chapter, at the moment this thesis was written, has not yet been published.

5.2 Holstein-Primakoff Mean-Field Theory

Let us take as a starting point the Hamiltonian (5.4), which is a general XY Hamiltonian defined on a square lattice with first and second nearest neighbor interactions J_γ, anisotropy Δ_γ and staggered magnetic field h with value $-h$ on sub-lattice A and h on sub-lattice B. We will mostly focus on the case where Δ_γ is small (up to $\sim 0.1J_\gamma$), since we want to keep the model XY-like and stay away from the Heisenberg limit of $\Delta = 1$. Also, we will focus on the case of antiferromagnetic interactions $J_\gamma > 0$.

The *Holstein-Primakoff* transformation is a powerful mathematical technique used in quantum many-body physics to express spin operators in terms of bosonic creation and annihilation operators. Introduced by T. Holstein and H. Primakoff in 1940 [42], it provides a way to approximate spin systems, such as those in magnetism, using the more tractable language of bosons. This transformation is particularly valuable in the study of *quantum spin waves* (magnons) in ferromagnets and antiferromagnets, where it allows to linearize the complex commutation relations of spin operators and derive dispersion relations for low-lying excitations. In

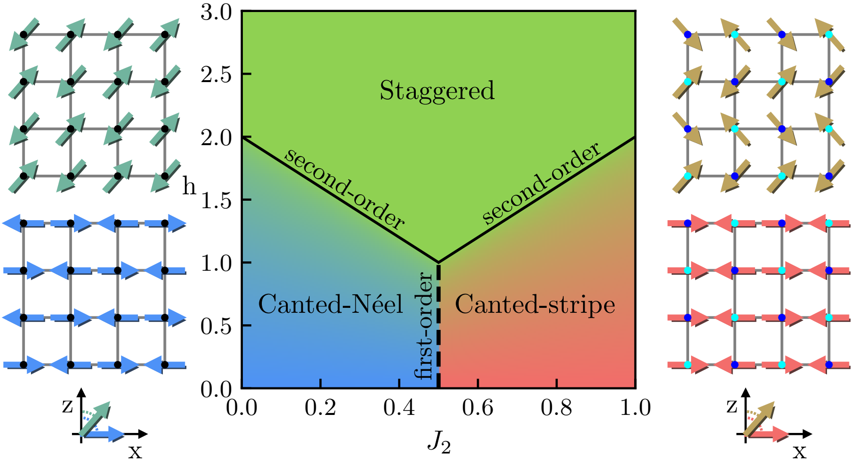

Figure 5.2: Classical phase diagram and spin directions for the $J_1 - J_2$ model (5.4). Here we consider no anisotropy $\Delta_\gamma = 0$ and $J_1 = 1$. The orientations of the spins configurations are coplanar in the $x - z$ plane, with θ taken from the z axis. The striped orders on the right were chosen columnar, but any rotation in the $x - y$ plane of each of the 2 sublattices (marked in cyan and blue) yields the same energy.

essence, this transformation bridges the discrete spin algebra and the continuous bosonic framework, enabling the use of techniques from second quantization and perturbation theory to study collective spin phenomena.

As any mean-field theory, the Holstein-Primakoff transformation has some limitations, primarily tied to its dependence on small fluctuations around an *ordered magnetic state*. The expansion is typically truncated at low orders in the bosonic operators (linear spin wave), which is valid only when the number of excited magnons is small compared to the total spin. As a result, it breaks down for systems with strong quantum fluctuations, or near phase transitions where the magnetic order is destroyed. In such regimes, higher-order corrections become essential, and alternative methods may provide a more accurate description of the quantum spin dynamics.

5.2.1 Classical Magnetization

We are interested in the classical ground state magnetic order of the spins of the model at different Hamiltonian (5.4) parameters values since it will be the starting point of the HP expansion [216–218]. Let us first consider the different magnetization patterns appearing, as outlined in Figure 5.2. For large h, it is easy to see that the spins will be ordered in a staggered-in-z state with spins anti-aligned with the field in the two sub-lattices. For large J_1 instead we expect to find a staggered state in the $x-y$ plane, while for large J_2 the ground state spin configuration becomes a state which is completely decoupled between the two sub-lattices, each realizing a staggered state in the $x-y$ plane.

We can divide the classical orientations in two groups: the canted-Néel and the canted-stripe order. The classical energies read

$$\begin{aligned} E_{\text{c-Néel}}(\theta) &= 2S^2\sin^2\theta(J_2-J_1)+2S^2\cos^2\theta(\Delta_2J_2-\Delta_1J_1)-hS\cos\theta \\ E_{\text{c-stripe}}(\theta) &= -2S^2\sin^2\theta J_2-2S^2\cos^2\theta\Delta_2J_2-hS\cos\theta \end{aligned}$$

and the respective angles are derived as $\cos\theta = h/h_c$ where

$$h_c^{\text{Néel}} = 4S\Big[J_1(1-\Delta_1)-J_2(1-\Delta_2)\Big] \tag{5.5a}$$

$$h_c^{\text{stripe}} = 4SJ_2(1-\Delta_2) \tag{5.5b}$$

From the energies we can clearly see that at $h=0$ the Néel order will be the ground state for $J_2 < J_1/2$ and at finite h the orders will be canted up to the critical fields (5.5) (see Figure 5.2). Thanks to the $U(1)$ symmetry of the model, we can fix the spin orientations on a the $x-z$ plane in the two canted orders. Let us also notice that in the canted-stripe order J_1 does not contribute to the energy and does not influence the canting angle.

5.2.2 Linear Spin Wave Expansion

Let us now consider the spin-wave expansion using the Holstein-Primakoff transformation [42]

$$\begin{aligned} S_i^+ &= \sqrt{2S-n_i}\,a_i \\ S_i^- &= a_i^\dagger\sqrt{2S-n_i} \\ S_i^z &= S-n_i \end{aligned}$$

with $n_i = a_i^\dagger a_i$ where a_i are bosonic operators. The mean-field approximation consists in considering the expansion for high S and low n_i

$$S_i^x = \sqrt{\frac{S}{2}}(a_i+a_i^\dagger)-\frac{1}{4\sqrt{2S}}(a_i^\dagger a_i a_i + a_i^\dagger a_i^\dagger a_i)+\mathcal{O}(a^5) \tag{5.6a}$$

$$S_i^y = -i\sqrt{\frac{S}{2}}(a_i-a_i^\dagger)+\frac{i}{4\sqrt{2S}}(a_i^\dagger a_i a_i - a_i^\dagger a_i^\dagger a_i)+\mathcal{O}(a^5) \tag{5.6b}$$

$$S_i^z = S-a_i^\dagger a_i \tag{5.6c}$$

We need to perform this expansion around the classical spin orientations derived in the previous section, meaning that we will first rotate the spins into a new reference frame. Let us call $(\hat{x},\hat{y},\hat{z})$ the original reference frame of the Hamiltonian and

(x, y, z) the new rotated reference frame. Due to the $U(1)$ symmetry we can fix the classical spin orientations on the $\hat{x} - \hat{z}$ plane. Let us call θ the canting angle, with its value being determined being $\theta_{\text{c-Néel}}$ or $\theta_{\text{c-stripe}}$ depending on the classical order we are considering.

For the case of the canted-Néel order, the transformation is $R_y(\theta)$ on sub-lattice A and $R_y(\theta + \pi)$ on sub-lattice B. Instead, in the canted-stripe phase, we chose a column stripe configuration for $h = 0$, meaning the transformation $R_y(\pm\theta)$ on sub-lattice A and $R_y(\pi \pm \theta)$ on sub-lattice B. Details of the reference frame rotation are given in Appendix C.1.

The Hamiltonian (5.4) in the rotated frame reads

$$\begin{aligned}\mathcal{H} = &\sum_{\gamma\in\{1,2\}} \sum_{\langle i,j\rangle_\gamma} \left[p^{xx}_\gamma S^x_i S^x_j + p^{yy}_\gamma S^y_i S^y_j + p^{zz}_\gamma S^z_i S^z_j\right] - h \sum_i \cos\theta S^z_i \\ &+ \sum_{\gamma\in\{1,2\}} \sum_{\langle i,j\rangle_\gamma} p^{xz}_\gamma (S^x_i S^z_j + S^z_i S^x_j)\end{aligned} \tag{5.7}$$

where the parameters $p^{\alpha\beta}_\gamma$ are functions of J_γ, Δ_γ and θ (details in Appendix C.1). I omitted here the terms proportional to p^{xy}, p^{xz} and p^{yz} since they vanish for any coplanar magnetization pattern and also the term proportional to hS^x since it vanishes with the right choice of quantization axis. The first line of (5.7) will yield the linear spin wave Hamiltonian of the system since it results in quadratic bosonic terms at first order of expansion (5.6). Higher terms in the expansion yielding three and four boson terms (second line and first term of first line, respectively) will be relevant in section 5.4 when considering the three and four boson Hamiltonian for magnon decay and scattering.

We can see from the HP expansion (5.6) that the part quadratic in HP bosons is given by the terms proportional to p^{xx}, p^{yy}, p^{zz} and h. This results into

$$\begin{aligned}\mathcal{H}_{\text{LSW}} = &S \sum_{\gamma\in\{1,2\}} \sum_{\langle i,j\rangle_\gamma} \left[\frac{p^{xx}_\gamma - p^{yy}_\gamma - 2ip^{xy}_\gamma}{2} a_i a_j + \frac{p^{xx}_\gamma + p^{yy}_\gamma}{2} a_i a^\dagger_j + H.c.\right. \\ &\left. + Sp^{zz}_\gamma - p^{zz}_\gamma (a^\dagger_i a_i + a^\dagger_j a_j)\right] + h\cos\theta \sum_i a^\dagger_i a_i - hS\cos\theta N_s\end{aligned} \tag{5.8}$$

with N_s number of sites in the system. Let us note that the initial model (5.4) in the canted states has a two site unit cell. By performing the rotation to the quantization axis and using the HP transformation, we can use a single boson flavor because of the symmetry between the two sublattices.

Let us now study the solution of this model in periodic boundary conditions. We can exactly solve this quadratic Hamiltonian by first applying a Fourier transform

$$a_i = \frac{1}{\sqrt{N_s}} \sum_{\mathbf{k}} e^{-i\mathbf{k}\cdot\mathbf{r}_i} a_{\mathbf{k}}$$

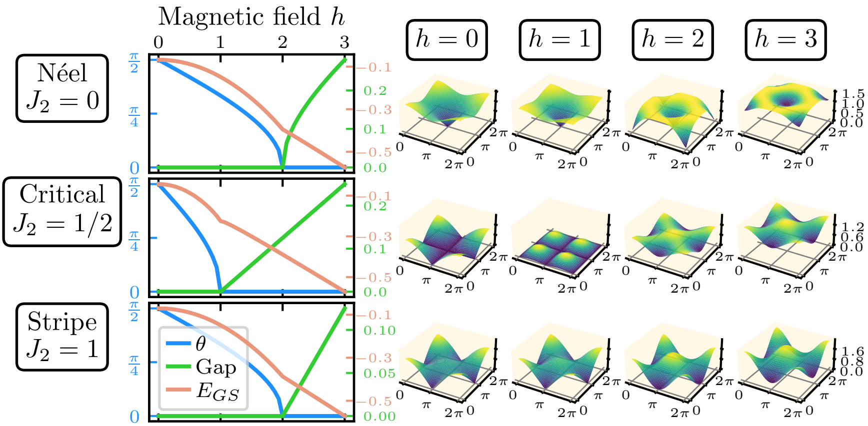

Figure 5.3: Linear spin wave results of the $J_1 - J_2$ model. I consider here the $J_1 = 1$ anisotropic $\Delta_1 = \Delta_2 = 0$ model. On the left are reported the quantization angle θ, the gap and the ground state energy E_{GS} as a function of magnetic field h. On the right, the dispersion relations $\epsilon(\mathbf{k})$ are shown at some selected magnetic fields. The top row shows the $J_2 = 0$ situation where spins cant according to the canted-Néel order. On the bottom row instead the high-J_2 case of canted-stripe order is shown. Finally, in the middle row I show the results of spin wave theory for the critical situation of $J_2 = J_1/2$. Which order is realized in this situation does not influence the result of the dispersion and of the angles.

We can compactly re-write the Hamiltonian in momentum space by using the basis $\psi^\dagger_{\mathbf{k}} = (a^\dagger_{\mathbf{k}}, a_{-\mathbf{k}})$

$$\mathcal{H}_{\text{LSW}}/N_s = E_0 + \frac{1}{N_s}\sum_{\mathbf{k}} \psi^\dagger_{\mathbf{k}} \mathcal{N}_k \psi_{\mathbf{k}}$$

with

$$\mathcal{N}_{11}(\mathbf{k}) = \mathcal{N}_{22}(\mathbf{k}) = S \sum_{\gamma\in\{1,2\}} \Big[(p^{xx}_\gamma + p^{yy}_\gamma)\Gamma_\gamma(\mathbf{k}) - 2p^{zz}_\gamma\Big] + \frac{h}{2}\cos\theta$$

$$\mathcal{N}_{12}(\mathbf{k}) = \mathcal{N}^*_{21}(\mathbf{k}) = S \sum_{\gamma\in\{1,2\}} \Gamma_\gamma(\mathbf{k})\left(p^{xx}_\gamma - p^{yy}_\gamma - 2ip^{xy}_\gamma\right)$$

$$E_0 = 2S(S+1) \sum_{\gamma\in\{1,2\}} p^{zz}_\gamma - h(S+\frac{1}{2})\cos\theta$$

and we introduced the notation $\Gamma_1(\mathbf{k}) = \frac{1}{2}\big[\cos(k_x) + \cos(k_y)\big]$ and $\Gamma_2(\mathbf{k}) = \frac{1}{2}\big[\cos(k_x + k_y) + \cos(k_x - k_y)\big]$. We can finally diagonalize the Hamiltonian by performing a Bogoliubov transformation $\psi_{\mathbf{k}} = \mathcal{M}_{\mathbf{k}}\tilde{\psi}_{\mathbf{k}}$ as detailed in Appendix C.2

and get

$$\mathcal{H}_{\text{LSW}}/N_s = E_{GS} + \frac{1}{N_s}\sum_{\mathbf{k}} \epsilon(\mathbf{k}) b^{\dagger}_{\mathbf{k}} b_{\mathbf{k}} \tag{5.9}$$

with $E_{GS} = E_0 + \frac{1}{2N_s}\sum_{\mathbf{k}} \epsilon(\mathbf{k})$ and

$$\epsilon(\mathbf{k}) = \sqrt{\mathcal{N}_{11}^2 - |\mathcal{N}_{12}|^2} \tag{5.10a}$$

$$\mathcal{M}_{\mathbf{k}} = \begin{pmatrix} \cosh r_{\mathbf{k}} & e^{i\phi_{\mathbf{k}}} \sinh r_{\mathbf{k}} \\ e^{-i\phi_{\mathbf{k}}} \sinh r_{\mathbf{k}} & \cosh r_{\mathbf{k}} \end{pmatrix} \tag{5.10b}$$

$$r_{\mathbf{k}} = -\frac{1}{2}\tanh^{-1}\left[\frac{|\mathcal{N}_{12}|}{\mathcal{N}_{11}}\right] \tag{5.10c}$$

$$\phi_{\mathbf{k}} = \arg\left[\frac{\mathcal{N}_{12}}{|\mathcal{N}_{12}|}\right] \tag{5.10d}$$

The ground state of the system is identified by the vacuum of Bogoliubov bosons, or *magnon* excitations, which have dispersion $\epsilon(\mathbf{k})$.

Let us go through the solutions of 5.9 (see Figure 5.3), starting from the canted-Néel $J_2 = 0$ case. We see (top row of Figure 5.3) that starting at high magnetic field, the dispersion is gapped (green curves on the left panel of Figure 5.3) as we expect being the single magnon excitations related to the flipping of an individual spin. At the critical field 5.5 of $h = 4SJ_1$ the dispersion becomes gapless and the quantization angle starts to tilt away from the z-axis. Finally, at the pure XY point of $h = 0$, we find the expected ground state energy of ~ -0.54 and the dispersion has the clear gapless point at $M = (\pi, \pi)$, maximum at $\Gamma = (0, 0)$ and a saddle point at $X = (0, \pi)$ and $Y = (\pi, 0)$, which will be relevant for section 5.4 since the magnons here will decay much faster due to the van Hove singularity in the density of states. In the language of stop ratios (5.2) the critical field for the anisotropic first nearest-neighbor model (3.2) is reached at $\alpha_c = 3/11 \sim 0.273$.

Going to high-J_2, the dispersion becomes gapless at X and Y, with maxima at Γ. In the gapped phase we see that the gap is now increasing linearly with the magnetic field. Finally, at the transition point of $J_2 = J_1/2$, we recover the interesting transition point in which the dispersion becomes gapless on an extended line connecting M and X. This parameter set corresponds to the quantum phase transition between the two orders and we expect the frustration to result into highly non-trivial phases. The critical transition from Néel to stripe order has been explored extensively both in the XY [219] and especially in the Heisenberg case [220–222]. The focus of the work presented here is not in understanding the highly entangled phases realized close to the critical point but more into describing the magnon excitations deep in the Néel and striped phases using the spin wave framework, which we anyway expect to fail in capturing highly entangled phases.

5.3 Mean-Field Eigenstates and Correlation Functions

With this model at hand, the first thing we can compute are correlation functions of the form $\langle\big[A_i(t), B_j(0)\big]\rangle$, where A and B can be expressed in terms of the spin operators $\mathbf{S}_i$. We can easily see that the commutator can be expressed in terms of the correlator by

$$\langle\big[A_i(t), B_j(0)\big]\rangle = 2i\text{Im}\Big[\langle A_i(t)B_j(0)\rangle\Big] \tag{5.11}$$

so they yield the same information. In order to understand it in the framework of the HP transformation, one first has to rotate the operators in the quantization axis reference frame. This in turns allows us to express the operators in terms of the HP bosons (5.6) and compute their expectation value on the ground state. This is an important aspect of the calculation: while in the 1D case we were able to compute the time evolution of the system along the ramp and thus create a state with a similar occupation of excitations, in the present case we are limited to ground state expectation values.

There are two ways to compute the correlators (5.11): the first one relies on the momentum space analytic solution derived above, which inherently assumes periodic boundary conditions. The second one instead consists in solving the model using a real space basis wavefunction. While the momentum space description allows to derive analytical formulas for the correlators, it does not allow to keep into consideration the boundary effects. By using a real space description we are limited to smaller system sizes since we will need to diagonalize a $2N_s \times 2N_s$ matrix but it allows us to consider open boundary conditions as well as inhomogeneities in the system. Since we want to simulate system sizes where boundary effects are likely to to be relevant[1], I will focus on the real-space solution, while the results for the momentum space calculation are detailed in Appendix C.4. Finally, let us note that in the case of open boundary conditions, the classical magnetization direction at each site might not be uniform due to boundary effects. This would then imply we need to consider site-dependent canting angles $\theta = \theta_i$ and, in turn, bond-dependent parameters $p^{\alpha\beta}_{\gamma}(i,j)$ as defined in Appendix C.1.

5.3.1 Wavefunctions

Starting from the real space Hamiltonian (5.8), we now consider spatially dependent quantization axis canting, neighbor couplings and magnetic field. We use as basis the wavefunction $\psi^\dagger = \left(a_1^\dagger, a_2^\dagger \dots a_{N_s}^\dagger, a_1, a_2 \dots a_{N_s}\right)$ to get

$$\mathcal{H} = \sum_{ij} \psi_i^\dagger \mathcal{N}_{ij} \psi_j + \text{const}$$

---

[1] The largest chip for current experiments is of the order of 10×10 qubits.

As for the diagonalization in momentum space, we have to perform a Bogoliubov transformation to diagonalize $\mathcal{H}$, being careful to respect the bosonic commutation relations. The procedure is described in Appendix C.3, where I follow the derivation of Ref. [175]. The transformation matrix $\psi = \mathcal{J}^{-1}\tilde{\psi}$ gives us the coefficients to express the original HP bosons in terms of the Bogoliubov bosons

$$a_i = \sum_{n=1}^{N_s} \left(U_{i,n} b_n + V_{i,n} b_n^\dagger \right) \tag{5.12a}$$

$$a_i^\dagger = \sum_{n=1}^{N_s} \left(V_{i,n} b_n + U_{i,n} b_n^\dagger \right) \tag{5.12b}$$

The wavefunctions U and V describe the single magnon excitations of the system, in particular

$$\Phi_{i,n} = (-1)^{\# i} \Big(U_{i,n} - V_{i,n} \Big) \tag{5.13}$$

describes the spatial distribution of excitation mode n. The spatial modulation is needed to take into account the different quantization axis in each site of the system. As I will show in the next section 5.4, these modes can be harnessed to create, collide and measure single magnons inside the system.

5.3.1.1 Fourier Transform for Open Boundary Conditions

To compute the Fourier transform of a space-dependent quantity $C(\boldsymbol{x})$ for a system with open boundary conditions, one must take into account that the function is not assumed to be periodic. In such cases, the standard discrete Fourier transform (DFT), which assumes periodicity at the boundaries by using plane waves, is not strictly applicable. Instead, one typically applies a transform consistent with open boundaries, such as a sine or cosine transform, depending on the physical symmetry of the problem. The discrete sine transform (DST) corresponds to vanishing values of $C(\boldsymbol{x})$ at the boundaries, since it assumes an odd extension of the function, i.e. $C(-\boldsymbol{x}) = -C(\boldsymbol{x})$. Instead, the discrete cosine transform (DCT) corresponds to vanishing derivatives (or currents) since it assumes an even extension $C(-\boldsymbol{x}) = C(\boldsymbol{x})$. Our model at zero magnetic field consists in the antiferromagnetic XX model. It has a gapless dispersion at $\mathbf{k} = (\pi, \pi)$ and maxima at $\mathbf{k} = (0, 0)$. We therefore expect the correct transform for an open system to be given by a DCT, since the solution to the diffusion equation gives a zero current at the edge. In particular, the so-called DCT of type 2 (in one dimension) reads

$$\begin{aligned} f(k) &= \sum_{n=0}^{N-1} f(n) \cos\left[(n + \frac{1}{2}) k \right] \\ k &= 0, \frac{\pi}{N}, \ldots, \frac{N-1}{N}\pi \end{aligned}$$

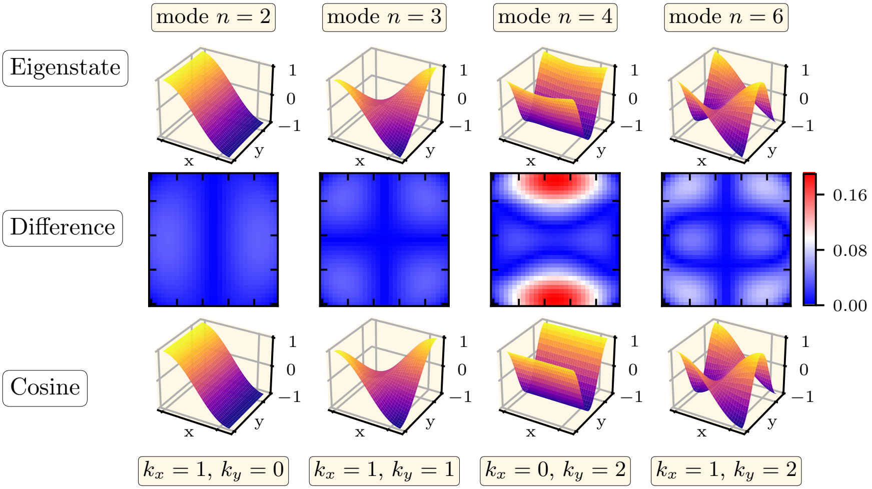

Figure 5.4: Comparison between the mean-field eigenstates (top row) and the cosines defined for the type-2 discrete cosine transform (bottom row), in a 30×31 square grid. While at bare eye they might look the same, differences arise when going to higher modes. The middle row shows the square difference per site.

This transform is even at $k = 0$, while it is odd at $k = \pi$, where it identically vanishes. This is what we expect for a system with a gapless dispersion, and is indeed what we find by looking at the eigenstates (5.13): as shown in Figure 5.4 the mean-field eigenstates (top row) do resemble cosine functions (bottom row), but with some differences (middle row). This comparison motivates the use of the DCT as the correct method to Fourier transform the real-space coordinates to momentum space, and it is the transformation I will use in the following section when computing the correlators.

5.3.2 Correlators

We can compute any correlator of the type $\langle S_i^{\hat{\alpha}}(t) S_j^{\hat{\beta}}(0)\rangle$ by first rotating to the reference frame, as specified in Appendix C.1. We then get a combination of expectation values, like

$$\langle S_i^{\hat{z}}(t) S_j^{\hat{z}}(0)\rangle = \sum_{\alpha,\beta} t_i^{\alpha z} t_j^{\beta z} \langle S_i^{\alpha}(t) S_j^{\beta}(0)\rangle$$

which means we need to derive formulas for all the possible correlators. Let us start from the $S^z S^z$ one: we begin by rewriting it in terms of HP bosons a

$$\langle S_i^z(t) S_j^z(0)\rangle = S^2 - S\left(\langle a_i^\dagger(t) a_i(t)\rangle + \langle a_j^\dagger(0) a_j(0)\rangle\right) + \langle a_i^\dagger(t) a_i(t) a_j^\dagger(0) a_j(0)\rangle$$

Since we care only about the imaginary part of this quantity, we only need to consider the last term, which we decompose using Wick theorem

$$\text{Im}\left[\langle S_i^z(t)S_j^z(0)\rangle\right] = \text{Im}\left[\langle a_i^\dagger(t)a_j^\dagger(0)\rangle\langle a_i(t)a_j(0)\rangle + \langle a_i^\dagger(t)a_j(0)\rangle\langle a_i(t)a_j^\dagger(0)\rangle\right]$$

There are then 4 different operators to compute

$$\begin{aligned}A_{ij}(t) &= \langle a_i^\dagger(t)a_j^\dagger(0)\rangle\\ B_{ij}(t) &= \langle a_i(t)a_j(0)\rangle\\ G_{ij}(t) &= \langle a_i^\dagger(t)a_j(0)\rangle\\ H_{ij}(t) &= \langle a_i(t)a_j^\dagger(0)\rangle\end{aligned}$$

We re-write them in terms of the energy eigenstates operators $b_{\mathbf{k}}$ and use the fact that the ground state is the vacuum of these particles to get

$$A_{ij}(t) = \langle\sum_{n=1}^{N_s} V_{i,n}b_n e^{-it\mathcal{H}}\sum_{n'=1}^{N_s} U_{j,n'}b_{n'}^\dagger\rangle = \sum_{n=1}^{N_s} e^{-it\epsilon(n)}V_{i,n}U_{j,n}$$

with $\epsilon(n)$ the eigenvalue of eigenstate $b_n^\dagger$. Similarly,

$$\begin{aligned}B_{ij}(t) &= \sum_{n=1}^{N_s} e^{-it\epsilon(n)}U_{i,n}V_{j,n}\\ G_{ij}(t) &= \sum_{n=1}^{N_s} e^{-it\epsilon(n)}V_{i,n}V_{j,n}\\ H_{ij}(t) &= \sum_{n=1}^{N_s} e^{-it\epsilon(n)}U_{i,n}U_{j,n}\end{aligned}$$

Using these formulas we can now derive all possible correlators. Let us note that correlators $\langle S_i^z(t)S_j^x(0)\rangle$ and $\langle S_i^z(t)S_j^y(0)\rangle$ will vanish since they contain an odd number of creation/annihilation operators. Let us also mention that without going to higher orders in the HP expansion (5.6), the S^zS^z term is the only one with 4 operators, whose expectation value is computed using Wick's theorem

$$\begin{aligned}\text{Im}\left[\langle S_i^z(t)S_j^z(0)\rangle\right] &= \text{Im}\left[G_{ij}(t)H_{ij}(t) + A_{ij}(t)B_{ij}(t)\right]\\ \text{Im}\left[\langle S_i^x(t)S_j^x(0)\rangle\right] &= \frac{S}{2}\text{Im}\left[G_{ij}(t) + H_{ij}(t) + A_{ij}(t) + B_{ij}(t)\right]\\ \text{Im}\left[\langle S_i^y(t)S_j^y(0)\rangle\right] &= \frac{S}{2}\text{Im}\left[G_{ij}(t) + H_{ij}(t) - A_{ij}(t) - B_{ij}(t)\right]\\ \text{Im}\left[\langle S_i^x(t)S_j^y(0)\rangle\right] &= \frac{S}{2}\text{Re}\left[H_{ij}(t) - G_{ij}(t) + A_{ij}(t) - B_{ij}(t)\right]\\ \text{Im}\left[\langle S_i^y(t)S_j^x(0)\rangle\right] &= \frac{S}{2}\text{Re}\left[G_{ij}(t) - H_{ij}(t) + A_{ij}(t) - B_{ij}(t)\right]\end{aligned}$$

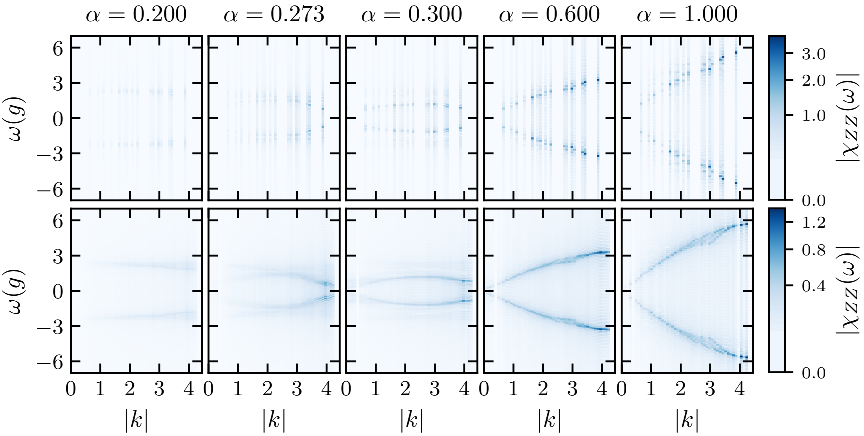

Figure 5.5: $\langle[Z_i(t), Z_j(0)]\rangle$ correlator at different stop ratios (5.2) for 7×9 (top row) and 20×20 (bottom row) systems. The site j is fixed in the middle of the grid and the correlator is evaluated for a measurement time of 800 ns with a step time 2 ns. The correlators showed here are Fourier transformed in time and space with a DFT and DCT, respectively. On the horizontal axis is used the absolute value of momentum. The critical stop ratio is $\alpha = 3/11 \sim 0.273$.

Finally, the full commutator reads, using the parameters of the spin rotation $t_i^{\alpha\beta}$ defined in Appendix C.1,

$$\begin{aligned}\langle\left[S_i^{\hat z}(t), S_j^{\hat z}(0)\right]\rangle = 2i\Big\{ & t_i^{zz}t_j^{zz}\mathrm{Im}\left[G_{ij}(t)H_{ij}(t) + A_{ij}(t)B_{ij}(t)\right] \\ & + \frac{S}{2}\left(t_i^{xz}t_j^{xz} + t_i^{yz}t_j^{yz}\right)\mathrm{Im}\left[G_{ij}(t) + H_{ij}(t)\right] \\ & + \frac{S}{2}\left(t_i^{xz}t_j^{xz} - t_i^{yz}t_j^{yz}\right)\mathrm{Im}\left[A_{ij}(t) + B_{ij}(t)\right] \\ & + \frac{S}{2}\left(t_i^{xz}t_j^{yz} + t_i^{yz}t_j^{xz}\right)\mathrm{Re}\left[A_{ij}(t) - B_{ij}(t)\right] \\ & + \frac{S}{2}\left(t_i^{xz}t_j^{yz} - t_i^{yz}t_j^{xz}\right)\mathrm{Re}\left[H_{ij}(t) - G_{ij}(t)\right]\Big\}\end{aligned} \tag{5.14}$$

There is much information one can extract from the correlators derived above. While all the formulas derived until here are general for the $J_1 - J_2$ model (5.4), from here on we will consider mostly the 1st nearest-neighbor model, since it is the main contributor to the setting of Ref. [4]. In Figure 5.5 is shown the $\langle[Z_i(t), Z_j(0)]\rangle$ correlator at different stop ratios (5.2) for two system sizes: the top 7×9 correlator represents a realistic system size reachable in systems like the one in [4], while the bottom row represents a 20×20 system where features are more clearly visible. In

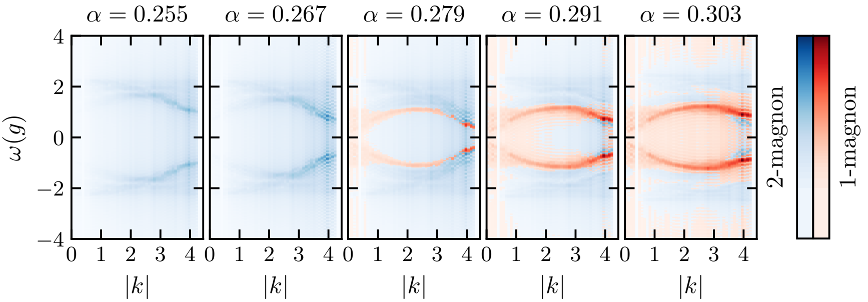

Figure 5.6: 1 (red) and 2 (blue) magnon contributions to the $\langle[Z_i(t), Z_j(0)]\rangle$ correlator of Figure 5.5.

order to get these results I used a DFT for the time dimension and a DCT for the real-space coordinate, as explained in the previous section 5.3.1.1. One can clearly see that this correlator probes the *single-magnon* dispersion in the gapless regime, while in the gapped phase we are left with mostly 2-magnon processes (first line of Eq. (5.14)).

One of the perks of the theoretical framework derived here is the possibility to separate the single contributions adding up to the full correlators. In the case of the $\langle[Z_i(t), Z_j(0)]\rangle$ correlator we divide it into the 1 - and 2 - magnon components appearing in Eq. (5.14), as in Figure 5.6. We can see clearly that the 1-magnon terms disappear below the critical stop-ratio, whereas the 2-magnon components are present for every stop-ratio but become progressively less prominent in the gapless phase $\alpha > 3/11 \sim 0.273$.

5.4 Magnon Decay and Scattering

The theoretical framework developed in this chapter has a very direct application in the description of magnon excitations. Experimentally, one can imagine creating a coherent state realizing single magnons by performing single Z rotations on the qubits

$$|n\rangle = e^{\pm i \frac{A}{2} \sum_j \Phi_{j,n} Z_j} |0\rangle \tag{5.15}$$

In the pure XY pase this amounts to creating a magnon state since $Z_j \sim a_j + a_j^\dagger$ and

$$b_n + b_n^\dagger = \sum_j \Phi_{jn}(a_j^\dagger + a_j) \tag{5.16}$$

with Φ_{jn} the mean-field wavefunctions defined in Eq. (5.13).

In order to explain theoretically the processes happening when exciting a particular magnon mode (5.15), we consider the situation in which at temperature T, a non-thermal population of magnons in a specific mode n is generated and is free to interact with the thermal environment. Given the small sizes of the lattices considered we expect momentum conservation to not restrict considerably the allowed processes, so we disregard it and consider only energy conservation. At lowest order the processes which will likely play a role are $1 \leftrightarrow 2$, $1 \leftrightarrow 3$ and $2 \leftrightarrow 2$ (see insets of Figure 5.7). The Hamiltonian is diagonalized at the linear spin wave level as mentioned in the section above, and we use the Bogoliubov matrices (5.12) to derive the vertices and decay rates for each of these processes.

For each of the processes, one needs to derive the corresponding vertex from the bosonic Hamiltonian (5.7). The three boson vertex will be given by the cross terms of $S^x S^z$ while the four boson vertices derive from $S^z S^z$ and from the higher order expansion (5.6) of the $S^x S^x$ and $S^y S^y$. I will refer to these vertices as $V_n(l,m)$, $V_n(l,m,p)$ and $V_{nl}(m,p)$ for the $1 \leftrightarrow 2$, $1 \leftrightarrow 3$ and $2 \leftrightarrow 2$ vertices, respectively. The details of the derivation of the interaction vertices are given in Appendix C.5.

Let us go through the first order processes in which one activated magnon mode n either decays or scatters with its thermal environment. There are two processes arising from the $1 \leftrightarrow 2$ vertex: either the mode n decays into two thermal modes ($1 \rightarrow 2$) or it scatters with a thermal mode into another thermal mode ($2 \rightarrow 1$). We can then compute the decay rate of this process using Fermi's golden rule

$$\Gamma_1^{1\rightarrow 2}(n) = 2\pi \sum_{lm} |V_n(l,m)|^2 \delta_\gamma(\epsilon_n - \epsilon_l - \epsilon_m) \frac{(1-e^{-\beta\epsilon_n})e^{\beta(\epsilon_l+\epsilon_m)}}{(e^{\beta\epsilon_l}-1)(e^{\beta\epsilon_m}-1)}$$

where the meaning of the index $_1$ will be clear in the next section 5.4.1. For the second process, following the same procedure we derive

$$\Gamma_1^{2\rightarrow 1}(n) = 4\pi \sum_{lm} |V_l(n,m)|^2 \delta_\gamma(\epsilon_l - \epsilon_n - \epsilon_m) \frac{(1-e^{-\beta\epsilon_n})e^{\beta\epsilon_l}}{(e^{\beta\epsilon_l}-1)(e^{\beta\epsilon_m}-1)}$$

Differently from the first considered process - which involves the *decay* of the activated mode - this one is thermally activated since it involves the scattering of the activated mode with a mode from the thermal bath. We get the decay associated to the 3 boson vertex by summing these two processes

$$\Gamma_1^{1\leftrightarrow 2}(n) = \Gamma_1^{1\rightarrow 2}(n) + \Gamma_1^{2\rightarrow 1}(n)$$

Let us follow the same procedure for the other two vertices. The $1 \leftrightarrow 3$ vertex also has two relevant processes: either the activated mode decays into three thermal modes ($1 \rightarrow 3$) or it scatters with two thermal modes into another thermal mode ($3 \rightarrow 1$), as shown in the insets of Figure 5.7. As in the $1 \leftrightarrow 2$ case, we use Fermi's golden rule to compute

$$\Gamma_1^{1\to 3}(n) = 6\pi \sum_{l,m,r} |V_n(l,m,r)|^2 \delta_\gamma(\epsilon_n - \epsilon_l - \epsilon_m - \epsilon_r) \\ \times \frac{(1-e^{-\beta\epsilon_n})e^{\beta(\epsilon_l+\epsilon_m+\epsilon_r)}}{(e^{\beta\epsilon_l}-1)(e^{\beta\epsilon_m}-1)(e^{\beta\epsilon_r}-1)}$$

for the first process, and

$$\Gamma_1^{3\to 1}(n) = 18\pi \sum_{l,m,r} |V_l(n,m,r)|^2 \delta_\gamma(\epsilon_l - \epsilon_n - \epsilon_m - \epsilon_r) \\ \times \frac{(1-e^{-\beta\epsilon_n})e^{\beta\epsilon_l}}{(e^{\beta\epsilon_l}-1)(e^{\beta\epsilon_m}-1)(e^{\beta\epsilon_r}-1)}$$

for the second. Also in this case we note that the first one is a pure decay, while the second one requires a thermal population of magnons to happen. Again, we sum them to get the full rate of the vertex

$$\Gamma_1^{1\leftrightarrow 3}(n) = \Gamma_1^{1\to 3}(n) + \Gamma_1^{3\to 1}(n)$$

Finally, the $2 \leftrightarrow 2$ vertex describes a process in which an activated magnon n scatters with a thermal mode into two others (inset of Figure 5.7). We then obtain the thermally activated decay rate

$$\Gamma_1^{2\leftrightarrow 2}(n) = 4\pi \sum_{l,m,r} |V_{n,r}(l,m)|^2 \delta_\gamma(\epsilon_n + \epsilon_r - \epsilon_l - \epsilon_m) \\ \times \frac{(1-e^{-\beta\epsilon_n})e^{\beta(\epsilon_l+\epsilon_m)}}{(e^{\beta\epsilon_r}-1)(e^{\beta\epsilon_l}-1)(e^{\beta\epsilon_m}-1)}$$

Because of the finite grid of our sample, also the energy landscape has some ‘discreteness’, meaning one cannot simply take an exact energy delta function. For this reason, we consider here a Lorentzian approximation to the delta function $\delta_\gamma(x) = \frac{1}{\pi}\frac{\gamma}{x^2+\gamma^2}$ with full width at half-maximum 2γ chosen as the mean energy difference between the energy eigenvalues of the system.

All the processes described above require an estimation of the temperature of the system. While in this theoretical setup we can chose the temperature we prefer by just fixing the Boltzmann factor, we want a method to extract the temperature consistently from an experimental setup. In experiments on quantum simulators one can access the bond energy, which serves as a thermometer of the state. In the framework of spin waves we can add a thermal population of magnons to the state and see how it affects the energy of the system, so we can map the state energy to an estimation of the temperature. This procedure is detailed in Appendix C.6.

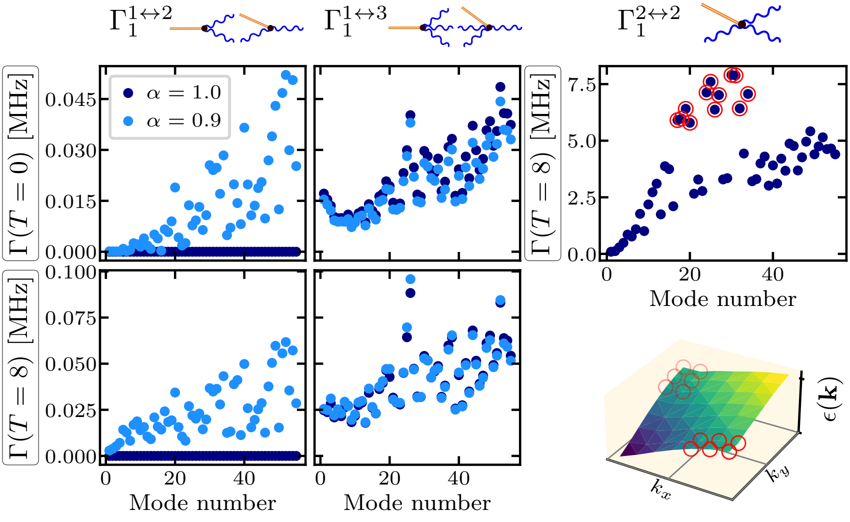

Figure 5.7: First order magnon decays for the 3 scattering processes considered (5.20) in a 7×8 system. The top row compares the decay rates at $T = 0$, the bottom row at $T = 8$ MHz. The processes are depicted in the cartoons on the top, with wiggly blue lines representing thermal modes and orange double lines the activate magnon mode (x axis). As expected the dominant role at finite temperature is played by the $2 \leftrightarrow 2$ process. The branching of decay rates corresponds to modes close to the Brillouin zone saddle points.

In Figure 5.7 are shown all the considered scattering and decay processes. The $1 \leftrightarrow 2$ vertex (left column) gives a decay rate which is vanishingly small at 0 magnetic field. Since in a realistic setting there might be remnant magnetic terms at the end of the ramp, we compare it with some small values h to see how fast it grows. We also compare the case of 0 temperature (top row) and of a finite realistic temperature of 8 MHz (which corresponds to a ground state energy of $-0.5(g)$, as explained in Appendix C.6).

What we find is that at finite values of the temperature, even at small finite magnetic fields, the $2 \leftrightarrow 2$ vertex gives the highest scattering rate among all the considered processes. This was somewhat expected given that the $1 \leftrightarrow 2$ process vanishes for 0 magnetic field and the $1 \leftrightarrow 3$ has lower amplitude. What is instead more surprising is the observed branching of decay rates, which points to shorter lifetimes for a particular set of activated modes (see red-circled modes in lower-right panel of Figure 5.7). This decay rate dependence on the mode number can be explained in a comprehensive way by considering the position in momentum space of the single magnon modes. As explained in section 5.3.1.1, the wavefunctions (5.13) are somewhat similar to the cosine functions we use to perform the DCT in real space. Motivated by this similarity, we can try to assign a momentum to the single magnon modes by choosing the highest peak in their DCT. As shown in the inset of Figure 5.7, the modes which correspond to the highest decay rates are located in proximity of the saddle points of the dispersion, i.e. close to the X-symmetry point. We can interpret the short life of these magnons due to the van Hove singularity in the density of states at the saddle point.

5.4.1 Amplitude Dependence

The processes we derived define the rate equation for the non-thermal population of mode n as

$$\frac{dN_n}{dt} = -\Gamma_1 N_n \tag{5.17}$$

with scattering processes yielding a decay rate Γ_1 as defined above. We can quantify the non-thermal population of modes n generated in the experimental setting, where a rotation of the spins is performed in order to get, for a given mode n, with a given amplitude A, the state (5.15). Since this is a coherent state, we get that the population of mode n is then $N_n(t=0) = \langle b_n^\dagger b_n \rangle = \frac{A^2}{4}$. From 5.17 we see that there should be no dependence of the decay rate on the amplitude for this process.

The situation changes if we consider processes in which multiple non-thermal modes n interact with each other. In particular, we can consider situations in which two n modes interact with each other. This can happen in all the above-mentioned vertices (Figure): in the $2 \leftrightarrow 2$ vertex with two n modes scattering into two thermal modes, in the $1 \leftrightarrow 3$ vertex with two activated modes and a thermal mode decaying into another thermal mode and also in the $1 \leftrightarrow 2$ vertex with two n modes decaying into one thermal, but we can see already here that due to energy conservation the matrix elements will be very small in this case. Same goes for higher order, where the only process in which three n modes interact is through the $1 \leftrightarrow 3$ vertex where they can combine into a thermal mode. We can write down the modified rate equation taking into account these processes as

$$\frac{dN_n}{dt} = -\Gamma_1 N_n - \Gamma_2 N_n^2 - \Gamma_3 N_n^3 \tag{5.18}$$

This rate equation no-longer has a well specified solution of exponential decay. The decay rate instead will experience a crossover from an exponential decay at long-times to an amplitude dependent decay at short-times, as

$$\Gamma(n) = \begin{cases} \Gamma_1(n) & \text{at long times} \\ \Gamma_1(n) + \frac{A^2}{4}\Gamma_2(n) + \frac{A^4}{16}\Gamma_3(n) & \text{at short times} \end{cases} \tag{5.19}$$

We can now combine the different decay processes to get at first order

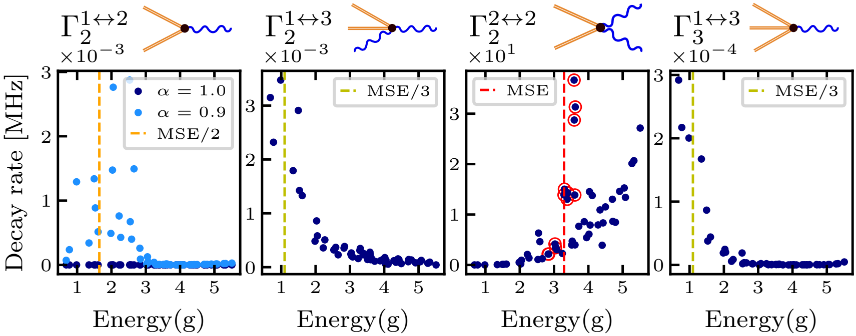

Figure 5.8: Second and third order processes as a function of mode energy (in units of g) for $T = 8$ MHz. The high density of states near the saddle-points influences the behavior of each scattering process. The mean saddle-point energy (MSE), taken as the mean energy of the circled modes (same modes as in Figure 5.7) shows us that the $1 \leftrightarrow 2$ and $1 \leftrightarrow 3$ rates peak around a half and a third of its value, respectively.

$$\Gamma_1(n) = \Gamma_1^{1\leftrightarrow 2}(n) + \Gamma_1^{1\leftrightarrow 3}(n) + \Gamma_1^{2\leftrightarrow 2}(n) \tag{5.20}$$

At second order we have

$$\Gamma_2(n) = \Gamma_2^{1\leftrightarrow 2}(n) + \Gamma_2^{1\leftrightarrow 3}(n) + \Gamma_2^{2\leftrightarrow 2}(n)$$

with

$$\Gamma_2^{1\leftrightarrow 2}(n) = \pi \sum_l |V_l(n,n)|^2 \delta_\gamma(2\epsilon_n - \epsilon_l) \frac{(1 - e^{-2\beta\epsilon_n})e^{\beta\epsilon_l}}{(e^{\beta\epsilon_l} - 1)}$$

$$\Gamma_2^{1\leftrightarrow 3}(n) = 6\pi \sum_{ml} |V_m(n,n,l)|^2 \delta_\gamma(2\epsilon_n + \epsilon_l - \epsilon_m) \frac{(1 - e^{-2\beta\epsilon_n})e^{\beta\epsilon_m}}{(e^{\beta\epsilon_l} - 1)(e^{\beta\epsilon_m} - 1)}$$

$$\Gamma_2^{2\leftrightarrow 2}(n) = 2\pi \sum_{ml} |V_{nn}(l,m)|^2 \delta_\gamma(2\epsilon_n - \epsilon_m - \epsilon_l) \frac{(1 - e^{-2\beta\epsilon_n})e^{\beta(\epsilon_l+\epsilon_m)}}{(e^{\beta\epsilon_l} - 1)(e^{\beta\epsilon_m} - 1)}$$

Finally, the only third order process comes from the $1 \leftrightarrow 3$ vertex,

$$\Gamma_3(n) = \pi \sum_l |V_l(n,n,n)|^2 \delta_\gamma(3\epsilon_n - \epsilon_l) \frac{(1 - e^{-3\beta\epsilon_n})e^{\beta\epsilon_l}}{e^{\beta\epsilon_l} - 1}$$

We can see from Figure 5.8 the behavior of the higher order decays for each mode as a function of energy. First of all, we note from the magnitude that also at second order the $2 \leftrightarrow 2$ vertex dominates the decay. This can be explained by the fact that it is no-longer thermally suppressed since it only depends on two activated magnons

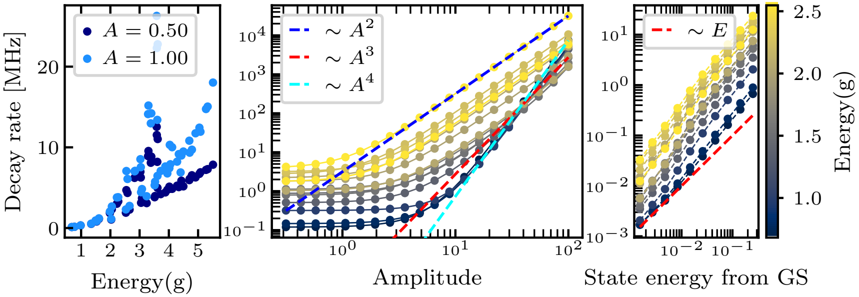

Figure 5.9: Full decay rate (5.19) at $T = 8$ MHz for a 7×8 system. The left panel shows the decay rate dependence on the mode energy for two amplitude values of 0.5 and 1: the branching of modes discussed in the text is evident in both cases. The central panel shows the decay rate dependence on the amplitude of some of the first low-energy states: the scaling with the amplitude changes depending on the mode energy. The right panel shows the dependence of the decay rate (in the limit $A \to 0$) on the bath energy (temperature). The modes considered are the same in the central and right panel.

scattering with each other, and it also has a large phase space of possible magnons to decay into, differently from the $1 \leftrightarrow 2$ and $1 \leftrightarrow 3$. We note from the $1 \leftrightarrow 2$ vertex (left panel of Figure 5.8) that, while this process is still activated only at non-zero magnetic fields, it peaks around values of about half of the saddle-point mode-energies. Same behavior occurs also for the $1 \leftrightarrow 3$ processes, were also we can expect the rate to be relevant only for modes with energy smaller than a third of the maximum magnon mode energy.

By combining all the processes as in (5.19) we obtain the final decay rate at a given amplitude A, as shown in the left panel of Figure 5.9. Increasing the amplitude the decay rate of the modes increases in a non-uniform way depending on the mode energy. We study this in the first few magnon modes in the central panel of Figure 5.9: after an initial range of low amplitudes where the decay rate stays almost constant we can see that the decay rates grows following a power-law scaling. In particular, we find different scalings ranging from A^2 to A^4 which depend largely on the mode energy. This can be understood also by comparing with the behavior of $\Gamma_3^{1\leftrightarrow 3}$ (right panel of Figure 5.8) which is the term yielding the A^4 dependence.

Finally, we can use the mapping from state energy to temperature (described in Appendix C.6) to determine the temperature dependence of the decay rate (right panel of Figure 5.9). We can see that for low temperature, the decay rate seems to scale linearly with the energy of the system, another prediction which can be easily tested on quantum simulators.

To conclude, in this section I showed that the study of scattering and decay of magnon excitations in the XY model, accessible by the use of analog-digital quantum simulators [4], may uncover unexplored phenomena. With the techniques developed in this chapter we have a toolbox to understand these processes and predict their behavior. The inclusion of second nearest-neighbors and anisotropies may yield even more interesting phenomena, and is left for future studies.

CHAPTER 6

Conclusions

6.1 Summary

The study of quantum magnetism in synthetic systems has become one of the most vibrant areas in condensed matter physics and quantum simulation. By combining the tunability of engineered materials with the conceptual richness of magnetic phenomena, we gain access to novel regimes of many-body physics that are often beyond reach in conventional materials. In this thesis, I have explored two broad and complementary classes of synthetic systems - moiré materials and quantum simulators - to investigate the emergence, characterization, and theoretical description of quantum magnetic behavior.

Quantum Magnetism in Moiré Systems The first part of this thesis focused on moiré heterostructures as naturally emerging synthetic magnets. In these systems, the interplay of lattice mismatch and twisting leads to long-wavelength modulation of the electronic and magnetic interactions, giving rise to new collective behaviors. In the case of strained layers of CrBr_3, the large spin magnitude $S = 3/2$ permitted a semiclassical approach to describe the resulting non-collinear magnetic textures. Through this, I demonstrated that moiré strain patterns can stabilize complex spin configurations, serving as an ideal platform for studying emergent magnetism at the mesoscale. This project illustrated how classical magnetism can still yield rich and tunable physics in the moiré context, connecting spin-lattice coupling to effective magnetic patterns that could, in principle, be directly imaged and controlled.

The second project turned to the quantum regime of magnetism in transition metal dichalcogenide (TMD) heterobilayers, specifically WSe_2/WS_2. Here, the low-energy excitations map onto an effective Heisenberg model on the kagome lattice, a canonical system for frustrated quantum magnetism. In this context, the inherently quantum nature of the material required the use of Schwinger boson mean-field theory to classify possible spin-liquid states and magnetically ordered phases. This part of the work highlighted one of the central themes of this thesis - the role of mean-field theories in describing complex magnetic systems. By comparing the predictions of Schwinger boson mean-field theory to MPS simulations, I discussed the scope and limitations of such approaches in capturing the subtle interplay between frustration, quantum fluctuations, and emergent order.

Quantum Magnetism in Quantum Simulators The second half of the thesis shifted from moiré materials to artificially engineered quantum systems - in particular, quantum processors composed of superconducting qubits. In collaboration with the Google Quantum AI team, I explored how these devices can realize and probe magnetic Hamiltonians through mixed analog-digital simulation techniques.

In the first project, I investigated the ground state preparation of the XY model via adiabatic ramps, connecting the experimental dynamics to the Kibble–Zurek mechanism of defect formation. This study demonstrated not only that key features of the XY phase could be observed in programmable quantum devices, but also that such systems can access dynamic quantities - notably space- and time-resolved correlation functions - which provide a new window into the real-time dynamics of quantum magnetism.

In the second project, I developed a mean-field theoretical framework to describe the 2D XY model realized in these quantum simulators. Using a linear spin-wave expansion based on the Holstein-Primakoff transformation, I provided a quantitative description of the magnon content and its signatures in measurable observables. This approach allowed for an analytic understanding of correlation functions, magnon dispersion, and decay processes in the presence of a thermal bath. Importantly, these results suggest that single-magnon excitations and finite-temperature effects can be probed directly within quantum simulator experiments, bridging theoretical predictions and experimental observables.

6.1.1 Additional Works Related to this Thesis

Related to the study of magnetism in moiré systems, another project I am currently pursuing is the characterization of the moiré properties of WSe_2/WS_2 by means of angular resolved photoemission spectroscopy (ARPES) [38, 39]. The moiré pattern in this heterobilayer leads to the emergence of side bands localized in the resulting mini-Brillouin zone. These bands can in turn be observed in ARPES experiment and through them we can derive both a better understanding of the single layers band structures and also how these bands are modified by the action of the moiré potential, leading to intensity modulations, gaps and side band displacements.

6.2 Synthesis and Outlook

Across both platforms - moiré materials and quantum simulators - a unifying theme of this thesis has been the search for controlled realizations of quantum magnetism and the development of theoretical tools to describe them. Mean-field approaches, whether in the form of Schwinger boson theory or linear spin-wave theory, have played a central role in bridging the gap between complex microscopic models and experimentally relevant observables. As shown in several contexts, these methods also reveal their limitations, particularly when addressing regimes dominated by strong correlations or quantum entanglement. Nevertheless, I showed that one of the powers of mean-field methods is to provide physical understanding and intuition, as opposed to numerical methods.

The comparison of engineered moiré systems and artificial quantum simulators emphasizes a dual strategy in the modern study of quantum magnetism. On one hand, moiré materials offer a fertile ground for discovering emergent phases of matter with minimal experimental intervention. On the other, quantum simulators allow the deliberate construction and interrogation of magnetic Hamiltonians under controlled conditions, where parameters can be tuned dynamically and observables measured with high fidelity.

Looking forward, the connection between these approaches holds promise for a new era of quantum magnetism research. Future directions include the exploration of non-equilibrium spin dynamics, finite-temperature spin-liquid behavior, and hybrid analog–digital protocols capable of probing topological order. Moreover, extending mean-field frameworks with variational or machine-learning-based techniques could further enhance their predictive power in strongly correlated regimes.

In summary, this thesis demonstrates how synthetic systems - both material and programmable - provide powerful and complementary platforms for realizing, controlling, and understanding quantum magnetism. By combining experimental innovation with rigorous theoretical modeling, we move closer to a complete understanding of strong interactions and magnetism in condensed matter systems.

APPENDIX A

Additional Details on Schwinger Boson

A.1 Gap Scaling

As mentioned in the main text, the difference between long range order (LRO) and spin liquid (SL) for a given ansatz can be identified in terms of the value of the Bogoliubov spinons' gap in the thermodynamic limit. If the gap closes the ground state gets a macroscopic occupation of spinons and this condensate leads to a LRO phase, since the global spin rotational invariance has been broken. On the other hand, if the gap remains finite then the system is in a $\mathbb{Z}_2$ spin liquid phase. The value of the gap is meaningful just at the thermodynamic limit, so we need to perform finite size scaling in order to infer its behavior.

The mean-field free energy that needs to be minimized in order to obtain the ground state is (3.9) and we can see that it contains a summation over the Brillouin Zone (BZ). For each value of $\mathbf{k}$ we consider in the BZ we then need to construct the matrix $\mathcal{N}_{\mathbf{k}}$ and diagonalize it with the Bogoliubov transformation in order to get Bogoliubov spinons' bands $\epsilon^{\mu}(k)$. Each value of k that we take corresponds to a new unit cell in the real space that we are considering for the value of the energy. In the code, we consider a grid of values over the BZ, which contains $\Omega = N_{\mathbf{k}} \times N_{\mathbf{k}}$ $\mathbf{k}$-points. As value of the gap is kept the smallest energy of the lowest band on the points of the grid.

It is clear that in order to correctly estimate the gap value we need to consider grids where the gap closing point is very close to one of the points of the grid. The position in the BZ where the gap closes for different LRO can be derived exactly. For the $q = 0$ order the gap closes at $(0, 0)$-point in the BZ, so there will be two degener-

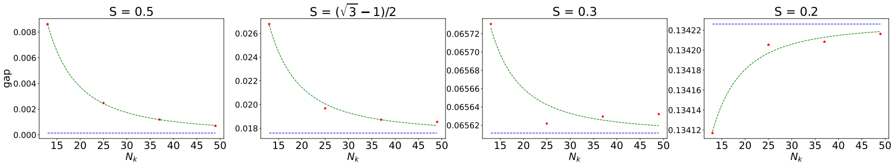

Figure A.1: Gap scaling at different spin values for ansatz 20 solutions at $J_2 = J_3 = 0$. The fit in green is performed using a function of the type $a/N_s + b$ where N_s is the number of sites in the system. In blue is reported the asymptotic value of the fit.

ate eigenvectors associated to the zero energy eigenvalue. For the $\sqrt{3} \times \sqrt{3}$ order the gap closes at $\mathbf{k} = (2\pi/3, 2\pi/3)$ while for the *cuboc-1* at $\mathbf{k} = (\pi/2, \sqrt{3}\pi/2)$. These values are all easily included in the grid because they are dependent of the size of the unit cell of the corresponding LRO. The $\mathbf{Q} = 0$ has a three-site unit cell, meaning that any even [1] value of N_k will contain it. The $\sqrt{3} \times \sqrt{3}$ order has nine sites in the unit cell, meaning 3 kagome unit cells, so any value of $N_{\mathbf{k}}$ multiple of three will do. Finally, the *cuboc-1* has a 12 sites unit cell, corresponding to 4 kagome unit cells, so N_k needs to be a multiple of 4. Following this scheme, the first value of $N_{\mathbf{k}}$ containing all the desired k points is 12, then 24, 36 etc. By plotting the value of the gap for increasing grid's thickness we can see how it scales towards the thermodynamic limit.

Let us look at some examples of typical behaviors. The gap should scale as $1/N_s$ with N_s the number of sites. In terms of N_k and of the unit cell size m this corresponds to $N_s = mN_{\mathbf{k}}^2$. We can fit with a function $a/N_s + b$ and check the value of b. Finally, we will have to introduce a cutoff on the value of the gap at the thermodynamic limit in order to distinguish between the two phases. In Figure A.1 is shown the gap scaling for ansatz 20 for different spin values at $J_2 = J_3 = 0$. The gap values go from being very well described by the fit at $S = 0.50$, indicating a LRO, to being very far from it at lower spin values, indicating a SL.

A.2 Spin Structure Factor

A.2.1 Using the Condensate

In the case of LRO we can extract the spin structure factor from the solution of the minimization by looking at the shape of the condensate. The procedure to do so is explained in [129, 177], here we report it with some additional practical details.

Once the gap closes, the spinons condense and form a particular orientation of the spins. The information is encoded in the spinon condensate, which we can write

---

[1] The grids consider both initial and final point of the BZ, so in the end $N_{\mathbf{k}}$ is increased by 1.

as

$$\chi(r) = \begin{pmatrix} \langle a_r \rangle \\ \langle b_r \rangle \end{pmatrix}. \tag{A.1}$$

The first think to look at are points in the BZ where the gap closes. These can be degenerate or more than one. Once these have been identified, let us call them $\tilde{\mathbf{k}}$, we need to extract the eigenvectors corresponding to the zero-energy bands. In particular, these will be the corresponding columns of $M_{\tilde{\mathbf{k}}}$ as defined in (3.11). Let us call them $\phi_{\tilde{\mathbf{k}}}$. The presence of a condensate is evidenced by a non-zero expectation value in the ground state of the wavefunction, i.e.

$$\langle \psi_{\tilde{\mathbf{k}}} \rangle = \begin{pmatrix} \langle a_{\tilde{\mathbf{k}}} \rangle \\ \langle b^\dagger_{\tilde{\mathbf{k}}} \rangle \end{pmatrix} = c\phi_{\tilde{\mathbf{k}}}. \tag{A.2}$$

By Fourier transforming the spinons in (A.1) we get

$$\chi(r) = \begin{pmatrix} \langle \sum_{\mathbf{k}} e^{i\mathbf{k}\cdot\mathbf{r}} a_{\mathbf{k}} \rangle \\ \langle \sum_{\mathbf{k}} e^{i\mathbf{k}\cdot\mathbf{r}} b_{\mathbf{k}} \rangle \end{pmatrix} = \begin{pmatrix} \sum_{\tilde{\mathbf{k}}} \langle a_{\tilde{\mathbf{k}}} \rangle e^{i\tilde{\mathbf{k}}\cdot\mathbf{r}} \\ \sum_{\tilde{\mathbf{k}}} \langle b_{\tilde{\mathbf{k}}} \rangle e^{i\tilde{\mathbf{k}}\cdot\mathbf{r}} \end{pmatrix},$$

since the expectation value of the spinons on all other k's is zero. The constants c in (A.2) will determine the global spin orientations while leaving the relative angles unchanged. The final value of the spins' directions will be given by

$$\mathbf{S}(\mathbf{r}) = \frac{1}{2}\chi^\dagger(\mathbf{r})\vec{\sigma}\chi(\mathbf{r}).$$

Once the directions of the spins have been determined, we compute the spin structure factor in the usual way as for the classical orders using the definition, (3.12).

A.2.2 Using the Ground State

In the case of a SL phase in order to compute the spin structure factor we need to rely on a slightly more involved calculation [178]. We can use the same method as for self consistency and write down the spin structure factor in terms of Bogoliubov spinons. Then we evaluate it on the ground state, which is the vacuum of spinons.

Let us start by writing the spinons a and b in terms of thew Bogoliubov bosons α and β

$$\psi_{\mathbf{k}} = \begin{pmatrix} a_{\mathbf{k}} \\ b^\dagger_{-\mathbf{k}} \end{pmatrix} = M_{\mathbf{k}}\tilde{\psi}_{\mathbf{k}} = \begin{pmatrix} U_{\mathbf{k}} & X_{\mathbf{k}} \\ V_{\mathbf{k}} & Y_{\mathbf{k}} \end{pmatrix} \begin{pmatrix} \alpha_{\mathbf{k}} \\ \beta^\dagger_{-\mathbf{k}} \end{pmatrix},$$

$$\psi^\dagger_{\mathbf{k}} = \begin{pmatrix} a^\dagger_{\mathbf{k}} & b_{-\mathbf{k}} \end{pmatrix} = \tilde{\psi}^\dagger_{\mathbf{k}} M^\dagger_{\mathbf{k}} = \begin{pmatrix} \alpha^\dagger_{\mathbf{k}} & \beta_{-\mathbf{k}} \end{pmatrix} \begin{pmatrix} U^\dagger_{\mathbf{k}} & V^\dagger_{\mathbf{k}} \\ X^\dagger_{\mathbf{k}} & Y^\dagger_{\mathbf{k}} \end{pmatrix}.$$

We need to keep in mind that there is an additional unit cell index ranging from 1 to m, where m is the unit cell size of the ansatz. Let us consider in detail how to derive the xx component of the spin structure factor (3.12), i.e. just the terms $S_i^x S_j^x$. In fact, for $SU(2)$ invariant models it is enough to compute only one of the three components.

$$\begin{aligned}\Xi(\mathbf{Q})^{xx} = \frac{1}{\mathcal{N}}\langle \sum_i \sum_{\mathbf{k},\mathbf{k}'} & e^{-i\mathbf{r}_i\cdot\mathbf{Q} - i\mathbf{x}_i\cdot(\mathbf{k}-\mathbf{k}')} \left(a^\dagger_{\mathbf{k}} b_{\mathbf{k}'} + b^\dagger_{\mathbf{k}} a_{\mathbf{k}'}\right) \\ \sum_j \sum_{\mathbf{t},\mathbf{t}'} & e^{i\mathbf{r}_j\cdot\mathbf{Q} - i\mathbf{x}_i\cdot(\mathbf{t}-\mathbf{t}')} \left(a^\dagger_{\mathbf{t}} b_{\mathbf{t}'} + b^\dagger_{\mathbf{t}} a_{\mathbf{t}'}\right)\rangle.\end{aligned}$$

Note that the position vector $\mathbf{r}_i$ is the *site* position whereas $\mathbf{x}_i$ in our convention is the ansatz unit cell position. We can decouple $\mathbf{r}_i$ into unit cell position plus position of site in the unit cell, which will be denoted by $\mathbf{s}_\mu$ ($\mu = 1, \dots m$). By summing over the unit cells we get two delta functions of the form $\delta(\mathbf{Q}+\mathbf{k}-\mathbf{k}')$ and $\delta(-\mathbf{Q}+\mathbf{t}-\mathbf{t}')$ so that

$$\Xi(\mathbf{Q})^{xx} = \frac{1}{\mathcal{N}}\langle \sum_{\mu,\gamma} \sum_{\mathbf{k},\mathbf{t}} \left(a^\dagger_{\mu,\mathbf{k}} b_{\mu,\mathbf{k}+\mathbf{Q}} + b^\dagger_{\mu,\mathbf{k}} a_{\mu,\mathbf{k}+\mathbf{Q}}\right) \left(a^\dagger_{\gamma,\mathbf{t}} b_{\gamma,\mathbf{t}-\mathbf{Q}} + b^\dagger_{\gamma,\mathbf{t}} a_{\gamma,\mathbf{t}-\mathbf{Q}}\right)\rangle.$$

where we call μ, γ the unit cell index of sites i, j respectively. Now, we can substitute Schwinger bosons a, b with Bogoliubov bosons α, β. We know these will respect the same commutation relations because of the construction of $M_{\mathbf{k}}$ as detailed in 3.3.1. By using the fact that the ground state is the vacuum of Bogoliubov bosons we arrive at the final form

$$\begin{aligned}\Xi(\mathbf{Q})^{xx} =& \frac{1}{\mathcal{N}} \sum_{\mathbf{k},\mu,\gamma} e^{i\mathbf{Q}\cdot(\mathbf{s}_\gamma - \mathbf{s}_\mu)} \Big\{ X^*_{\mu\nu}(\mathbf{k}) Y^*_{\mu,\nu'}(-\mathbf{k}-\mathbf{Q}) \Big[X_{\gamma\nu}(\mathbf{k}) Y_{\gamma\nu'}(-\mathbf{k}-\mathbf{Q}) \\ & + Y_{\gamma\nu}(\mathbf{k}) X_{\gamma\nu'}(-\mathbf{k}-\mathbf{Q}) \Big] + V_{\mu\nu}(-\mathbf{k}) U_{\mu\nu'}(\mathbf{k}+\mathbf{Q}) \Big[V^*_{\gamma\nu}(-\mathbf{k}) U^*_{\gamma\nu'}(\mathbf{k}+\mathbf{Q}) \\ & + U^*_{\gamma\nu}(-\mathbf{k}) V^*_{\gamma\nu'}(\mathbf{k}+\mathbf{Q}) \Big] \Big\}.\end{aligned}$$

Similar expressions can be derived for $\Xi(\mathbf{Q})^{yy}$ and $\Xi(\mathbf{Q})^{zz}$.

APPENDIX B

Jordan-Wigner Transformation

When the system is composed of a 1D chain of spins, it realizes a XX model with staggered field (eq. 3.2). In absence of further neighbor exchange or anisotropy ZZ, this model is exactly integrable by means of a Jordan-Wigner transformation [223] to fermions c_i

$$\begin{aligned} \sigma_i^+ &= c_i^\dagger Q_i^\dagger \\ \sigma_i^- &= Q_i c_i \\ \sigma_i^z &= 2c_i^\dagger c_i - 1 \end{aligned}$$

with

$$Q_i = \exp\left\{ i\pi \sum_{j=1}^{i-1} c_j^\dagger c_j \right\} = \prod_{j=1}^{i-i} \exp\left\{ i\pi c_j^\dagger c_j \right\} = \prod_{j=1}^{i-i} T_j$$

Let us start by using raising/lowering operators as $\sigma_i^x \sigma_{i+1}^x + \sigma_i^y \sigma_{i+1}^y = \frac{1}{2}(\sigma_i^+ \sigma_{i+1}^- + \sigma_i^- \sigma_{i+1}^+)$. Translating to fermionic operators then

$$\sigma_i^- \sigma_{i+1}^+ = Q_i c_i c_{i+1}^\dagger Q_{i+1}^\dagger = c_i e^{i\pi c_i^\dagger c_i} c_{i+1}^\dagger = c_i c_{i+1}^\dagger T_i$$

We can then consider the action of T_i on the eigenstates of $\sigma^{+/-}$ to see that

$$\begin{aligned} c_i T_i \left|+\right\rangle &= -\left|-\right\rangle \\ c_i T_i \left|-\right\rangle &= 0 \end{aligned}$$

and since

$$\begin{aligned} c_i \left|+\right\rangle &= \left|-\right\rangle \\ c_i \left|-\right\rangle &= 0 \end{aligned}$$

we conclude that $c_i T_i = -c_i$. Finally,

$$\begin{aligned} \sigma_i^- \sigma_{i+1}^+ &= c_{i+1}^\dagger c_i \\ \sigma_i^+ \sigma_{i+1}^- &= c_i^\dagger c_{i+1} \end{aligned}$$

Considering periodic boundary conditions we can thus rewrite the Hamiltonian with free fermions on a chain of N_s sites

$$\begin{aligned} H_{JW} =& g \sum_{i=1}^{N_s} \left(c_i^\dagger c_{i+1} + c_{i+1}^\dagger c_i \right) + h \sum_{i=1}^{N_s} (-1)^i c_i^\dagger c_i \\ &- g \left(c_{N_s}^\dagger c_1 + c_1^\dagger c_{N_s} \right) \left(e^{i\pi \sum_{j=1}^{N_s} c_j^\dagger c_j} + 1 \right) \end{aligned} \tag{B.1}$$

For large system size we may neglect the last term proportional to $e^{i\pi \sum_{j=1}^{N_s} c_j^\dagger c_j} + 1$. States with an odd number of excitations will not be affected by this additional term, while for states with an even number of excitations there will be a correction of order $1/N_s$. We can diagonalize the system by performing a Fourier transform $c_j = \frac{1}{\sqrt{N_s}} \sum_k e^{-ikj} c_k^\alpha$ on the two sub-lattices $\alpha = A, B$

$$H = \sum_{k=0}^{\pi} \psi_k^\dagger \mathcal{N}_k \psi_k, \qquad \psi_k = \begin{pmatrix} c_k^A \\ c_k^B \end{pmatrix}, \qquad \mathcal{N}_k = \begin{pmatrix} h & 2g\cos k \\ 2g\cos k & -h \end{pmatrix}$$

We can directly diagonalize this Hamiltonian to get the eigenstates γ and the eigenvalues ω

$$H = \sum_{k=0}^{\pi} \omega(k) \gamma_k^\dagger \gamma_k, \qquad \omega(k) = \sqrt{h^2 + 4g^2 \cos k^2}$$

The system is gapped for any finite value of h and is composed of a filled fraction of fermionic (γ_k) states.

B.1 Time Evolution and Correlators

We are interested in computing space-time resolved correlators. For this purpose, we diagonalize the Hamiltonian B.1 in *real space* using as basis the fermionic operators $\psi = (c_1, c_2 \ldots {}_{N_s})^T$. Doing so, we can both compute the correlators in real space and also add terms which would break the translational invariance of the system, like a disordered magnetic field. The diagonalization yields the system's eigenstates as a combination of real space operators c_i

$$\gamma_k^\dagger = \sum_{i=1}^{N_s} \beta_{ik} c_i^\dagger$$

where β_{ik} are the eigenvectors of B.1. We perform a linear ramp of the system as in the experiment by time evolving each eigenstate independently, i.e.

$$|\psi_k(t)\rangle = \hat{T} e^{-i2\pi \int_{t_0}^{t} H(t')dt'} \, |\psi_k(t_0)\rangle \simeq \lim_{\delta t \to 0} \prod_{j=1}^{t/\delta t} e^{-i2\pi H(j\delta t)\delta t} \, |\psi_k(t_0)\rangle$$

with $\hat{T}$ the time ordering operator, and δt the time step.

At the end of the time evolution, which we also stop according to the stop ratio, we compute the correlators by transforming to fermions

$$\langle [Z_i(t), Z_0(0)] \rangle = 2i\mathrm{Im}\left[\langle Z_i(t) Z_0(0) \rangle\right] = 2i\mathrm{Im}\left[\langle c_i^\dagger(t) c_0(0) \rangle \langle c_i(t) c_0^\dagger(0) \rangle\right]$$

Let us introduce the notation

$$\begin{aligned} G_{ij}(t) &= \langle c_i^\dagger(t) c_j(0) \rangle \\ H_{ij}(t) &= \langle c_i(t) c_j^\dagger(0) \rangle \end{aligned}$$

Using Heisenberg formulation of operators we can compute these quantities from the components of the time-evolved wavefunction (α_{ik}) and the eigenstates of the instantaneous Hamiltonian (β_{ik}) as

$$\begin{aligned} G_{ij}(t) &= \sum_{k=1}^{N_s/2} \langle \psi_k | \, e^{-i2\pi H t} c_i^\dagger e^{i2\pi H t} c_j \, | \psi_k \rangle \\ &= \sum_{k=1}^{N_s/2} \sum_{l_1, l_2, q_1, q_2, q_3, q_4 = 1}^{N_s} \alpha_{l_1,k}^* \beta_{l_1 q_1} \beta_{i q_2}^* e^{-i2\pi\epsilon(q_2)t} \beta_{j q_3} \alpha_{l_2 k} \beta_{l_2 q_4}^* \, \langle 0 | \, \gamma_{q_1} \gamma_{q_2}^\dagger \gamma_{q_3} \gamma_{q_4}^\dagger \, | 0 \rangle \\ &= \sum_{k=1}^{N_s/2} \sum_{l_1, l_2 = 1}^{N_s} \sum_{q_1, q_2 = 1}^{N_s} \alpha_{l_1,k}^* \beta_{l_1 q_1} \beta_{i q_1}^* e^{-i2\pi\epsilon(q_1)t} \beta_{j q_2} \alpha_{l_2 k} \beta_{l_2 q_2}^* \\ &= \sum_{k=1}^{N_s/2} \sum_{l_1, q_1 = 1}^{N_s} \alpha_{jk} \alpha_{l_1 k}^* \beta_{l_1 q_1} e^{-i2\pi\epsilon(q_1)t} \beta_{i q_1}^* \\ &= \left[\alpha \alpha^\dagger \beta U(t) \beta^\dagger\right]_{ji} \end{aligned}$$

Other correlators including energy and spin-current can be defined using

$$E_j = \frac{g}{2}\Big(X_j X_{j+1} + Y_j Y_{j+1}\Big) = g\big(c_j^\dagger c_{j+1} + c_{j+1}^\dagger c_j\big) \tag{B.2}$$

$$J_j = \frac{g}{2}\Big(X_j Y_{j+1} - Y_j X_{j+1}\Big) = ig\big(c_j^\dagger c_{j+1} - c_{j+1}^\dagger c_j\big) \tag{B.3}$$

We can then proceed as above for the ZZ correlator and evaluate

$$\begin{aligned}
\langle [Z_j(t), Z_0(0)] \rangle &= 2i\mathrm{Im}\left[G_{j,0}(t)H_{j,0}(t)\right] \\
\langle [E_j(t), E_0(0)] \rangle &= 2i\mathrm{Im}\left[G_{j,1}(t)H_{j+1,0}(t) + G_{j,0}(t)H_{j+1,1}(t)\right. \\
&\qquad\qquad \left. + G_{j+1,1}(t)H_{j,0}(t) + G_{j+1,0}(t)H_{j,1}(t)\right] \\
\langle [J_j(t), J_0(0)] \rangle &= 2i\mathrm{Im}\left[-G_{j,1}(t)H_{j+1,0}(t) + G_{j,0}(t)H_{j+1,1}(t)\right. \\
&\qquad\qquad \left. + G_{j+1,1}(t)H_{j,0}(t) - G_{j+1,0}(t)H_{j,1}(t)\right] \\
\langle [E_j(t), Z_0(0)] \rangle &= 2i\mathrm{Im}\left[G_{j,0}(t)H_{j+1,0}(t) + G_{j+1,0}(t)H_{j,0}(t)\right] \\
\langle [Z_j(t), E_0(0)] \rangle &= 2i\mathrm{Im}\left[G_{j,1}(t)H_{j,0}(t) + G_{j,0}(t)H_{j,1}(t)\right] \\
\langle [J_j(t), Z_0(0)] \rangle &= 2i\mathrm{Re}\left[G_{j,0}(t)H_{j+1,0}(t) - G_{j+1,0}(t)H_{j,0}(t)\right] \\
\langle [Z_j(t), J_0(0)] \rangle &= 2i\mathrm{Re}\left[G_{j,1}(t)H_{j,0}(t) - G_{j,0}(t)H_{j,1}(t)\right] \\
\langle [E_j(t), J_0(0)] \rangle &= 2i\mathrm{Re}\left[G_{j,1}(t)H_{j+1,0}(t) - G_{j,0}(t)H_{j+1,1}(t)\right. \\
&\qquad\qquad \left. + G_{j+1,1}(t)H_{j,0}(t) - G_{j+1,0}(t)H_{j,1}(t)\right] \\
\langle [J_j(t), E_0(0)] \rangle &= 2i\mathrm{Re}\left[G_{j,1}(t)H_{j+1,0}(t) + G_{j,0}(t)H_{j+1,1}(t)\right. \\
&\qquad\qquad \left. - G_{j+1,1}(t)H_{j,0}(t) - G_{j+1,0}(t)H_{j,1}(t)\right]
\end{aligned}$$

B.2 Results

By using a finite ramp in a system with $N_s = 60$ qubit chain with initial magnetic field of $15(2\pi)$ MHz and a final coupling of $10(2\pi)$ MHz. We obtain the result in Figure 5.1 in the main text. One can consider additionally the effect of finite temperature in the system, by either making the ramp faster (Figure B.1a) or by introducing by hand a finite temperature in the system using the Fermi-Dirac distribution (Figure B.1b). By introducing some noise in the parameters we can also see an emergent asymmetry in the branches, as can be seen in Figure B.2. Finally, we show off some of the other correlator in Figure B.3.

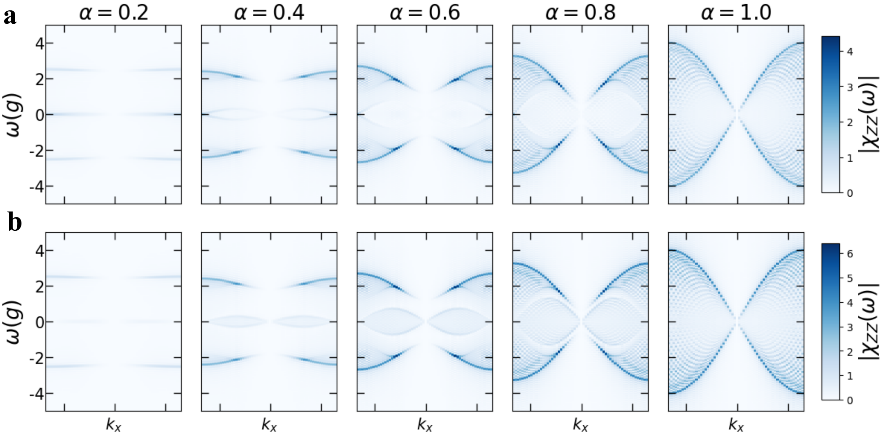

Figure B.1: **a**, $\langle[Z_i(t), Z_j(0)]\rangle$ correlator from a 80ns ramp. **b**, $\langle[Z_i(t), Z_j(0)]\rangle$ correlator evaluated with a temperature of $g/2$.

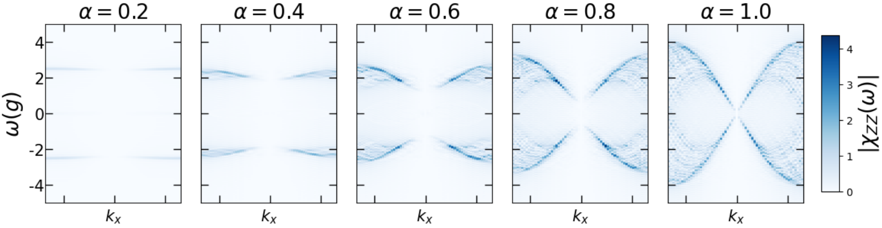

Figure B.2: $\langle[Z_i(t), Z_j(0)]\rangle$ correlator with added 1% uniform noise in parameters g and h.

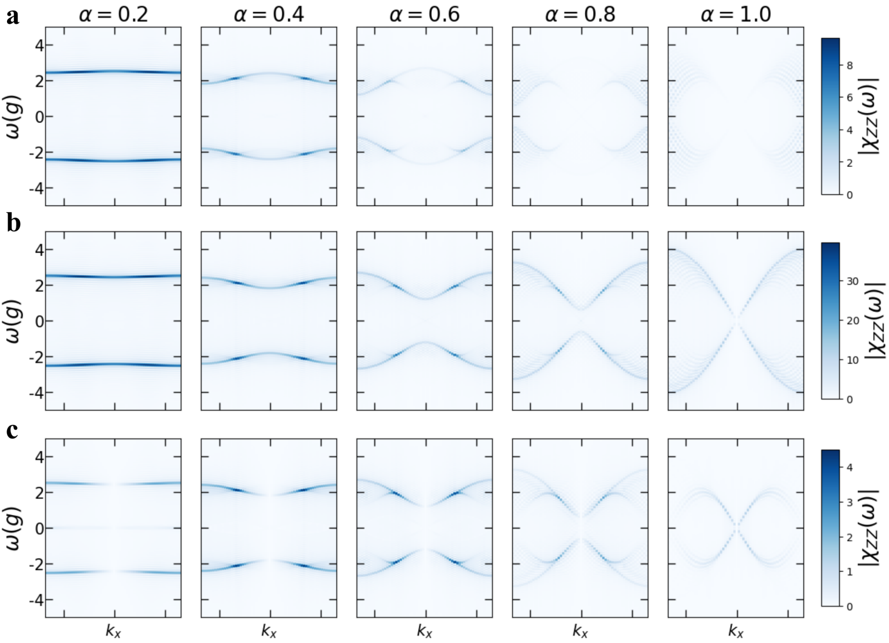

Figure B.3: $\langle [E_i(t), E_j(0)] \rangle$ (**a**), $\langle [J_i(t), J_j(0)] \rangle$ (**b**) and $\langle [Z_i(t), E_j(0)] \rangle$ (**c**) correlators with 500ns ramp and uniform parameters.

APPENDIX C

Additional Details on Holstein-Primakoff

C.1 Parameters of Canted-Néel and Canted-Stripe Orders

Here we derive the parameters of the spins in the rotated reference as used in 5.7 for the two classical orders we consider: canted-Néel and canted-stripe (see Figure 5.2).

For each order, the new reference frame in term of the canting angles $\theta(i)$ corresponds to a rotation with respect to y of this angle. If we consider the case of the canted-Néel order i a homogeneous system, the angle θ obtained from Eq. (5.5) defines an order of spins where the sub-lattice A and B are rotated by θ and $\theta + \pi$. we can explicitly evaluate

$$Z_{A/B} = \pm \begin{pmatrix} \sin\theta \\ 0 \\ \cos\theta \end{pmatrix}, \qquad X_{A/B} = \pm \begin{pmatrix} \cos\theta \\ 0 \\ -\sin\theta \end{pmatrix}, \qquad Y_{A/B} = \begin{pmatrix} 0 \\ 1 \\ 0 \end{pmatrix}$$

In the sections in the main text we will refer to these coefficients as

$$t_i^{\alpha\beta} = \alpha_i \cdot \beta$$

so that for example $t_{i\in A}^{zx} = \sin\theta\cos\phi$. Using this language we can write the spin components in the new frame like $S_{i\in A}^{\hat{x}} = \sum_{\alpha=x,y,z} t_{i\in A}^{\alpha x} S_{i\in A}^{\alpha} = \cos\theta\cos\phi S_i^x - \sin\phi S_i^y + \sin\theta\cos\phi S_i^z$ and so on.

For the canted-stripe order instead we have to distinguish the two sub-lattices A, B and in each of these the two sub-lattices $1, 2$ since each sublattice creates a staggered pattern (see Figure 5.2). In this order, on sub-lattice A the rotations will be θ and $\theta + \pi$ while on sublattice B $-\theta$ and $-\theta + \pi$.

We can then compute the parameters $p_\gamma^{\alpha\beta}$, which include all the terms multiplying $S_i^\alpha \sigma_j^\beta$ after the reference frame rotation. The general formula is

$$p_\gamma^{\alpha\beta}(i,j) = \sum_{\delta=x,y,z} J_\gamma^\delta t_i^{\alpha\delta} t_j^{\beta\delta}$$

where $J_\gamma^x = J_\gamma^y = J_\gamma$ and $J_\gamma^z = J_\gamma \Delta_\gamma$.

Let us see as an example the term p_1^{xx}: this will contain all the terms proportional to $S_i^x S_j^x$ at 1st nearest neighbor after the reference frame rotation. Starting from the Hamiltonian 5.4 we get, for the canted-Néel order (without J_2),

$$p_1^{xx} = J_1 \left(t_i^{xx} t_j^{xx} + t_i^{xy} t_j^{xy} + \Delta_1 t_i^{xz} t_j^{xz} \right) = -J_1(\cos^2\theta + \Delta_1 \sin^2\theta)$$

C.2 Bogoliubov Transformation for Bosonic System: Analytic

We write down here explicitly the steps to perform the Bogoliubov transformation for a bosonic system. Let us start from a system with Hamiltonian

$$\mathcal{H}/N_s = E_0 + \frac{1}{N_s} \sum_k \psi_k^\dagger \mathcal{N}_k \psi_k$$

with $\psi_k = (a_k, a_{-k}^\dagger)^T$. The transformation matrix $\mathcal{M}_k$ is defined as

$$\psi_k = \mathcal{M}_k \tilde{\psi}_k$$

where $\tilde{\psi}_k = (\alpha_k, \alpha_{-k}^\dagger)^T$ are the Bogoliubov bosons. In order for the transformation to be well defined we first find that, for general

$$\mathcal{M}_k = \begin{pmatrix} p & q \\ r & s \end{pmatrix}$$

we need

$$\begin{aligned} a_k &= p\alpha_k + q\alpha_{-k}^\dagger \\ a_{-k}^\dagger &= r\alpha_k + s\alpha_{-k}^\dagger = p^*\alpha_{-k}^\dagger + q^*\alpha_k \end{aligned}$$

so we get

$$\mathcal{M}_k = \begin{pmatrix} p & q \\ q^* & p^* \end{pmatrix}$$

In order to get correct commutation relations for the Bogoliubov bosons we get the constraint

$$\left[\alpha_k, \alpha^\dagger_{k'}\right] = \frac{\delta_{k-k'}}{|p|^2 - |q|^2}$$

so that we can re-parametrize the transformation matrix as

$$\mathcal{M}_k = \begin{pmatrix} \cosh r_k & e^{i\phi} \sinh r_k \\ e^{-i\phi} \sinh r_k & \cosh r_k \end{pmatrix} \tag{C.1}$$

Here we also used the fact that a general phase multiplied to $\mathcal{M}_k$ does not modify it so that the diagonal is pure real.

Since we are dealing with bosons let us note that $\mathcal{M}_k^{-1} \neq \mathcal{M}_k^\dagger$. In order to diagonalize the Hamiltonian then we need to introduce

$$\Gamma = \begin{pmatrix} 1 & 0 \\ 0 & -1 \end{pmatrix}$$

so that we can write

$$\psi_k^\dagger \mathcal{N}_k \psi_k = \tilde{\psi}_k^\dagger \mathcal{M}_k^\dagger \mathcal{N}_k \mathcal{M}_k \tilde{\psi}_k = \tilde{\psi}_k^\dagger \Gamma \mathcal{M}_k^{-1} \Gamma \mathcal{N}_k \mathcal{M}_k \tilde{\psi}_k = \tilde{\psi}_k^\dagger \Gamma \mathcal{D} \tilde{\psi}_k$$

which means that we have to diagonalize

$$\Gamma \mathcal{N}_k = \begin{pmatrix} f & g \\ -g^* & -f \end{pmatrix}$$

where we introduced a shorter notation for $f = \mathcal{N}_{11}$ and $g = \mathcal{N}_{12}$. By computing the characteristic polynomial we get the dispersion

$$\lambda = \pm\sqrt{f^2 - |g|^2}$$

and

$$\mathcal{D} = \begin{pmatrix} \lambda & 0 \\ 0 & -\lambda \end{pmatrix}$$

Using Eq. (C.1) we then compute

$$\begin{aligned} \mathcal{M}^{-1} \Gamma \mathcal{N} \mathcal{M} &= \begin{pmatrix} \cosh r_k & -e^{i\phi} \sinh r_k \\ -e^{-i\phi} \sinh r_k & \cosh r_k \end{pmatrix} \begin{pmatrix} f & g \\ -g^* & -f \end{pmatrix} \begin{pmatrix} \cosh r_k & e^{i\phi} \sinh r_k \\ e^{-i\phi} \sinh r_k & \cosh r_k \end{pmatrix} \\ &= \begin{pmatrix} \sqrt{f^2 - |g|^2} & 0 \\ 0 & -\sqrt{f^2 - |g|^2} \end{pmatrix} \end{aligned}$$

We get two equations for the two elements in the first row

$$\begin{cases} \sqrt{f^2 - |g|^2} = (\cosh^2 r_k + \sinh^2 r_k) f + \sinh r_k \cosh r_k 2Re[g e^{-i\phi}] \\ -2 \sinh r_k \cosh r_k f = 2Re[g e^{-i\phi}] \sinh^2 r_k + g e^{-i\phi} \end{cases}$$

From the second equation we see that $ge^{-i\phi}$ is real, and so by using the property that $\tanh 2x = \frac{\sinh 2x}{\cosh 2x} = \frac{2\sinh x \cosh x}{2\sinh^2 x+1}$ we finally obtain

$$\begin{aligned} e^{i\phi} &= \frac{g}{|g|} \\ \tanh 2r_k &= -\frac{|g|}{f} \end{aligned}$$

C.3 Bogoliubov Transformation for Bosonic System: Numeric

When diagonalizing the Hamiltonian in real space we do not have access to the analytical solution. We then have to resort to a numerical diagonalization, paying attention to respect the commutation relations of the resulting bosons diagonalizing the Hamiltonian. The case we have at hand was described by Colpa [175] in Section 4, as the case of a general boson Hamiltonian. Since here we only have real coefficients in the Hamiltonian parameters we resort to the method described in Section 5, which we recap here in order to have a closed description. Let us specify that the method described here works for *real* Hamiltonians. The general model we consider (5.4) has an Hamiltonian which is not strictly real since in case of $p_\gamma^{xy} \neq 0$ we have a complex term. Nevertheless this term is 0 for any coplanar order and the derivation of the general case is so much more complicated that we only consider the simplified solution here.

The Hamiltonian can be separated into

$$\mathcal{H} = \begin{pmatrix} A & B \\ B & A \end{pmatrix}$$

and we call the transformation matrix $\tilde{\psi} = \mathcal{J}\psi$ where $\psi^\dagger = (a_1^\dagger, a_2^\dagger \dots a_N^\dagger, a_1, a_2 \dots a_N)$ and $\tilde{\psi}^\dagger = (\gamma_1^\dagger, \gamma_2^\dagger \dots \gamma_N^\dagger, \gamma_1, \gamma_2 \dots \gamma_N)$. This transformation matrix $\mathcal{J}$ performs a so-called para-unitary transformation on the system. We further divide into

$$\mathcal{J}^{-1} = \begin{pmatrix} U & V \\ V & U \end{pmatrix}, \qquad \mathcal{J} = \begin{pmatrix} U^\dagger & -V^\dagger \\ -V^\dagger & U^\dagger \end{pmatrix}$$

The form of $\mathcal{J}$ ensures that the bosons γ respect canonical commutation relations. The transformation can be written as

$$\left(\mathcal{J}^\dagger\right)^{-1} \mathcal{H} \mathcal{J}^{-1} = \mathrm{diag}(\omega_1, \dots \omega_{N_s}, \omega_1, \dots \omega_{N_s})$$

We start by writing the eigenvalue equation, using as u_r, v_r the columns of U and V

$$\begin{aligned} Au_r + Bv_r &= u_r\omega_r \\ Bu_r + Av_r &= -v_r\omega_r \end{aligned}$$

Adding and subtracting we write in terms of $\phi_r = u_r + v_r$ and $\psi_r = u_r - v_r$

$$\begin{aligned}(A+B)\phi_r &= \omega_r \psi_r \\ (A-B)\psi_r &= \omega_r \phi_r\end{aligned}$$

By multiplying by $A - B$ and $A + B$ we get the eigenvalue equations

$$\begin{aligned}(A-B)(A+B)\phi_r &= \omega_r^2 \phi_r \\ (A+B)(A-B)\psi_r &= \omega_r^2 \psi_r\end{aligned}$$

We can then start our procedure by first performing a Cholesky decomposition of $A - B = K^\dagger K$, so that

$$K^\dagger \left[K(A+B)K^\dagger - \omega_r^2 \mathcal{I}\right] (K^\dagger)^{-1} \phi_r = 0$$

We then diagonalize $K(A+B)K^\dagger$ which will have eigenvalues ω_r^2 and eigenvectors $\tilde{\chi}_r$. We normalize these eigenvectors in order to get $\chi_r^\dagger \chi_r = \omega_r^{-1}$ and finally obtain

$$\begin{aligned}\phi_r &= K^\dagger \chi_r \\ \psi_r &= \frac{1}{\omega_r}(A+B)K^\dagger \chi_r\end{aligned}$$

From these we derive the matrices U and V and finally the transformation matrix $\mathcal{J}^{-1}$.

C.4 Correlators in Momentum Space

The momentum space description relies on the analytical solution derived in section (5.10). Since the definition of momentum relies on the periodicity of the lattice, this method inherently assumes periodic boundary conditions. Let us consider the specific example of the $\langle \left[S_i^{\hat{z}}(t), S_j^{\hat{z}}(0)\right] \rangle$ correlator. First of all, we need to rotate each S^z operator in the quantization axis basis using the coefficients $t_i^{\alpha\beta}$ defined in Appendix C.1

$$S_i^{\hat{z}} = t_i^{xz} S^x + t_i^{yz} S^y + t_i^{zz} S^z$$

where the hat refers to the measurement basis. We see that we will have to compute correlators of S^α with S^β for all combinations of $\alpha, \beta = x, y, z$. The correlator is evaluated using the Heisenberg representation of time evolution

$$\langle S_i^{\hat{z}}(t) S_j^{\hat{z}}(0) \rangle = \langle GS| \, e^{i\mathcal{H}t} S_i^{\hat{z}} e^{-i\mathcal{H}t} S_j^{\hat{z}} \, |GS\rangle$$

Let us express each spin operator using the HP bosons and performing the Fourier transformation as

$$S_i^x = \sqrt{\frac{S}{2}}(a_i + a_i^\dagger) = \sqrt{\frac{S}{2N_s}} \sum_{\mathbf{k}} e^{-i\mathbf{k}\cdot\mathbf{r}_i}(a_{\mathbf{k}} + a_{-\mathbf{k}}^\dagger)$$

$$S_i^y = -i\sqrt{\frac{S}{2}}(a_i - a_i^\dagger) = -i\sqrt{\frac{S}{2Ns}} \sum_{\mathbf{k}} e^{-i\mathbf{k}\cdot\mathbf{r}_i}(a_{\mathbf{k}} - a_{-\mathbf{k}}^\dagger)$$

$$S_i^z = S - a_i^\dagger a_i = S - \frac{1}{N_s} \sum_{\mathbf{k},\mathbf{k}'} e^{-i(\mathbf{k}+\mathbf{k}')\cdot\mathbf{r}_i} a_{-\mathbf{k}}^\dagger a_{\mathbf{k}'}$$

Finally, we can now use the transformation to Bogoliubov bosons derived in Appendix C.3 $a_{\mathbf{k}} = \cosh r_{\mathbf{k}} b_{\mathbf{k}} + e^{i\phi_{\mathbf{k}}} \sinh r_{\mathbf{k}} b_{-\mathbf{k}}^\dagger$, the property of the ground state of being the vacuum of such bosons and these being eigenstates of the Hamiltonian with eigenvalue $\epsilon(\mathbf{k})$ to get[1]

$$\begin{aligned}
e^{-i\mathcal{H}t} S_j^{\hat{z}} |GS\rangle &= t_j^{zz} \frac{S}{N_s} \sum_{\mathbf{k}} e^{-i(\phi_{\mathbf{k}} - \phi_{-\mathbf{k}})} \sinh r_{\mathbf{k}} \sinh r_{-\mathbf{k}} \\
&- \frac{t_j^{zz}}{N_s} \sum_{\mathbf{k},\mathbf{k}'} e^{-i(\mathbf{k}+\mathbf{k}')\cdot\mathbf{r}_j} e^{-it(\epsilon(-\mathbf{k})+\epsilon(-\mathbf{k}'))} e^{i\phi_{\mathbf{k}'}} \cosh r_{\mathbf{k}} \sinh r_{\mathbf{k}'} b_{-\mathbf{k}}^\dagger b_{-\mathbf{k}'}^\dagger \\
&+ \sqrt{\frac{S}{2N_s}} \sum_{\mathbf{k}} e^{-i\mathbf{k}\cdot\mathbf{r}_j} e^{-it\epsilon(-\mathbf{k})} \Big[(t_j^{xz} - it_j^{yz}) e^{i\phi_{\mathbf{k}}} \sinh r_{\mathbf{k}} + (t_j^{xz} + it_j^{yz}) \cosh r_{\mathbf{k}} \Big] b_{-\mathbf{k}}^\dagger
\end{aligned}$$

We do the same for the left term $\langle GS| e^{i\mathcal{H}t} S_i^{\hat{z}}$ and then sandwich the two terms together. The resulting expression will contain expectation values of operators with different numbers of Bogoliubov bosons $b_{\mathbf{k}}$. It is evident that only terms with even number of operators will have a non-vanishing expectation value on the ground state. By using the fact that $\phi_{\mathbf{k}} = \phi_{-\mathbf{k}}$ and $r_{\mathbf{k}} = r_{-\mathbf{k}}$ we finally get

$$\begin{aligned}
\langle S_i^{\hat{z}}(t) S_j^{\hat{z}}(0) \rangle &= t_i^{zz} t_j^{zz} \left(S - \frac{1}{N_s} \sum_{\mathbf{k}} \sinh^2 r_{\mathbf{k}} \right) \\
&+ \frac{S}{2N_s} \sum_{\mathbf{k}} e^{-i\mathbf{k}\cdot(\mathbf{r}_i - \mathbf{r}_j)} e^{-it\epsilon(\mathbf{k})} \Big[(t_i^{xz} - it_i^{yz}) \cosh r_{\mathbf{k}} + (t_i^{xz} + it_i^{yz}) e^{-i\phi_{\mathbf{k}}} \sinh r_{\mathbf{k}} \Big] \\
&\qquad \times \Big[(t_j^{xz} + it_j^{yz}) \cosh r_{\mathbf{k}} + (t_j^{xz} - it_j^{yz}) e^{i\phi_{\mathbf{k}}} \sinh r_{\mathbf{k}} \Big] \\
&+ \frac{t_i^{zz} t_j^{zz}}{N_s^2} \sum_{\mathbf{k},\mathbf{k}'} e^{-i(\mathbf{k}+\mathbf{k}')\cdot(\mathbf{r}_i - \mathbf{r}_j)} e^{-it(\epsilon(\mathbf{k})+\epsilon(\mathbf{k}'))} \Big(\sinh^2 r_{\mathbf{k}} \cosh^2 r_{\mathbf{k}'} \\
&\qquad + \frac{1}{2} e^{i(\phi_{\mathbf{k}'} - \phi_{\mathbf{k}})} \sinh 2r_{\mathbf{k}} \sinh 2r_{\mathbf{k}'} \Big)
\end{aligned}$$

---

[1] The GS energy phase factor cancels with the term on the left side of the correlator, so we omit it.

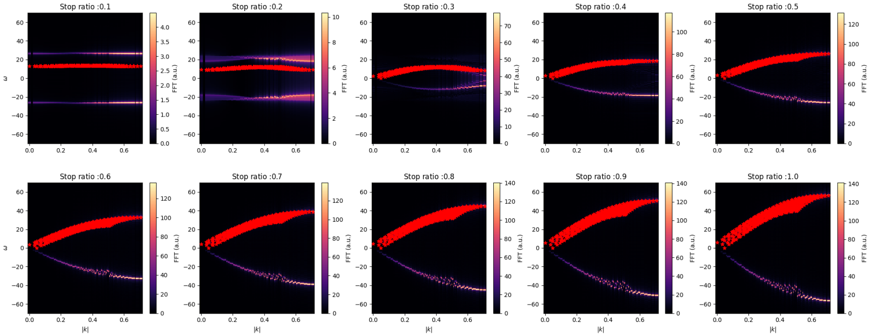

Figure C.1: Fourier transform of $\langle [S_i^{\hat{z}}(t), S_j^{\hat{z}}(0)] \rangle$ plotted as a function of momentum absolute value for system size 30×30. This correlator has been computed using the momentum description, so it assumes periodic boundary conditions, where the standard FFT is justified. Red stars superimposed on the picture are the dispersion of the magnons.

The result of this calculation is showed in Figure C.1 for different stop ratios (defined in section 5.3). The plot shows the Fourier-transformed version of the correlator, plotted over the absolute value of momentum. In this way it is clear that by computing the $\langle [S^z, S^z] \rangle$ correlator we are effectually probing the dispersion of magnons in the system. In particular, for stop ratio 1 (end of the ramp) the rotation brings $S^z \to a + a^\dagger$ so the single magnon response is directly probed.

C.5 Interaction Vertices

3-Boson Hamiltonian

In order to compute the vertex describing one magnon resulting in two magnons, we need to consider the three boson Hamiltonian. With the properly aligned quantization axis, the only non-vanishing three boson term comes from the mixed $S^x S^z$ term (5.7)

$$\hat{V}^3 = f \sum_{\langle i,j \rangle} \left[a_i^\dagger a_i (a_j + a_j^\dagger) + i \leftrightarrow j \right] \tag{C.2}$$

with the parameter $f = -\sqrt{\frac{S}{2}} \sum_\gamma p_\gamma^{xz}$ which in the case of $J_2 = 0$ takes the explicit form $f = -\sqrt{\frac{S}{2}} J_1 (1 - \Delta_1) \sin(2\theta)$. We can already see from here that this process will be identically 0 both in the pure XY phase where $\theta = \pi/2$ and in the gapped phase where $\theta = 0$, as explained also in the main text.

$1 \leftrightarrow 2$ **Process**

By transforming to Bogoliubov bosons (5.12) we will obtain all possible combinations of bosonic terms. The vertex we are interested in is

$$\hat{V}^{1\to 2} = \sum_{l,m,n} V_n(l,m) \left(b_l^\dagger b_m^\dagger b_n + H.c. \right)$$

Let us note that from the same Hamiltonian (C.2) one could also derive the matrix elements for the processes of spontaneous annihilation and creation from the vacuum of three magnons $\propto b_l b_m b_n$ and $\propto b_l^\dagger b_m^\dagger b_n^\dagger$, respectively.

We obtain the $1 \leftrightarrow 2$ vertex as

$$\begin{aligned} V_n(l,m) =& \frac{f}{2} \sum_{\langle i,j\rangle_\gamma} \Big[U_{jm} V_{jl} \big(U_{in} + V_{in}\big) + U_{jn} \big(U_{il} U_{jm} + U_{jm} V_{il}\big) \\ & + V_{jn} \big(V_{il} V_{jm} + U_{il} V_{jm}\big) + (l \leftrightarrow m) \Big] + (i \leftrightarrow j) \end{aligned}$$

The symmetrization $l \leftrightarrow m$ is needed to get the correct vertex.

4-**Boson Hamiltonian**

For the $1 \leftrightarrow 3$ and the $2 \leftrightarrow 2$ vertices one needs to derive the vertex associated with the four-boson part of the Hamiltonian. By inspection of (5.7), we can determine that it derives from the terms $S^z S^z$ and from the higher order expansion (5.6) of terms $S^x S^x$ and $S^y S^y$.

We derive the vertex to be given by three terms

$$\begin{aligned} \hat{V}^4 = \sum_{\langle i,j\rangle} \Big\{ & f_1 \left[(a_i a_j^\dagger + a_i^\dagger a_j) a_j^\dagger a_j + i \leftrightarrow j \right] \\ & + f_2 \left[(a_i a_j + a_i^\dagger a_j^\dagger) a_j^\dagger a_j + i \leftrightarrow j \right] \\ & + f_3 \left[a_i^\dagger a_i a_j^\dagger a_j + i \leftrightarrow j \right] \Big\} \end{aligned} \tag{C.3}$$

with parameters

$$\begin{aligned} f_1^\gamma &= -\frac{p_\gamma^{xx} + p_\gamma^{yy}}{8} \\ f_2^\gamma &= -\frac{p_\gamma^{xx} - p_\gamma^{yy}}{8} \\ f_3^\gamma &= \frac{p_\gamma^{zz}}{2} \end{aligned}$$

Vertex $1 \leftrightarrow 3$

We derive the matrix elements

$$\hat{V}^{1\to 3} = \sum_{n,l,m,p} V_n(l,m,p) \left(b_l^\dagger b_m^\dagger b_p^\dagger b_n + H.c. \right)$$

by expanding Hamiltonian (C.3) in terms of Bogoliubov bosons. We need to symmetrize the vertex over the $l \leftrightarrow m \leftrightarrow p$ indices. We obtain

$$\begin{aligned} V_n(l,m,r) = & \sum_\gamma \frac{f_1^\gamma}{6} \sum_{\langle i,j\rangle_\gamma} \Big[V_{in}V_{jl}U_{jm}U_{jp} + U_{jn}U_{il}U_{jm}U_{jp} + 2V_{jn}U_{il}V_{jm}U_{jp} \\ & + U_{in}V_{jl}V_{jm}U_{jp} + 2U_{jn}V_{il}V_{jm}U_{jp} + V_{jn}V_{il}V_{jm}V_{jp} + (l \leftrightarrow m \leftrightarrow p) \Big] \\ + & \sum_\gamma \frac{f_2^\gamma}{6} \sum_{\langle i,j\rangle_\gamma} \Big[U_{in}V_{jl}U_{jm}U_{jp} + U_{jn}V_{il}U_{jm}U_{jp} + 2V_{jn}V_{il}V_{jm}U_{jp} \\ & + V_{in}V_{jl}V_{jm}U_{jp} + 2U_{jn}U_{il}V_{jm}U_{jp} + V_{jn}U_{il}V_{jm}V_{jp} + (l \leftrightarrow m \leftrightarrow p) \Big] \\ + & \sum_\gamma \frac{f_3^\gamma}{6} \sum_{\langle i,j\rangle_\gamma} \Big[U_{in}U_{il}V_{jm}U_{jp} + V_{in}V_{il}V_{jm}U_{jp} + U_{jn}U_{jl}V_{im}U_{ip} \\ & + V_{jn}V_{jl}V_{im}U_{ip} + (l \leftrightarrow m \leftrightarrow p) \Big] + (i \leftrightarrow j) \end{aligned}$$

Vertex $2 \leftrightarrow 2$

We derive the matrix elements

$$\hat{V}^{2\to 2} = \sum_{n,l,m,p} V_{n,l}(m,p) b_m^\dagger b_p^\dagger b_n b_l$$

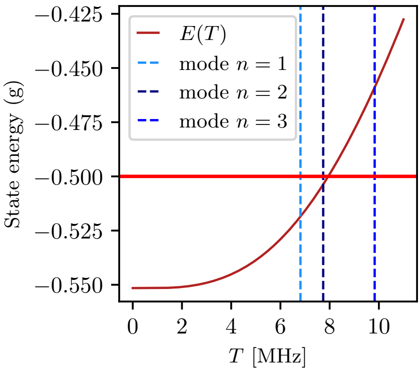

Figure C.2: Temperature dependence of the state energy (C.4) in a 7×8 system. Dashed lines represent the energies of the first magnon modes.

by expanding Hamiltonian (C.3) in terms of Bogoliubov bosons. We need to symmetrize the vertex over the $n \leftrightarrow l$, $m \leftrightarrow p$ and $nl \leftrightarrow mp$ indices. We obtain

$$\begin{aligned}
V_{nl}(m,p) = \sum_{\gamma} \frac{f_1^\gamma}{4} \sum_{\langle i,j \rangle_\gamma} \Big[& U_{jn}V_{il}U_{jm}U_{jp} + 2V_{in}V_{jl}U_{jm}V_{jp} + 2U_{jn}V_{jl}U_{im}U_{jp} \\
& + V_{jn}V_{jl}U_{im}V_{jp} + 2U_{in}U_{jl}U_{jm}V_{jp} + U_{jn}V_{il}V_{jm}V_{jp} \\
& + U_{jn}U_{jl}U_{jm}V_{ip} + 2U_{jn}V_{jl}V_{im}V_{jp} + (n \leftrightarrow l; m \leftrightarrow p; nl \leftrightarrow mp) \Big] \\
+ \sum_{\gamma} \frac{f_2^\gamma}{4} \sum_{\langle i,j \rangle_\gamma} \Big[& U_{in}U_{jl}U_{jm}U_{jp} + 2U_{in}V_{jl}U_{jm}V_{jp} + 2U_{jn}V_{jl}U_{jm}V_{ip} \\
& + V_{jn}V_{jl}V_{im}V_{jp} + 2U_{jn}V_{il}U_{jm}V_{jp} + V_{in}V_{jl}V_{jm}V_{jp} \\
& + U_{jn}U_{jl}U_{im}U_{jp} + 2U_{jn}V_{jl}U_{im}V_{jp} + (n \leftrightarrow l; m \leftrightarrow p; nl \leftrightarrow mp) \Big] \\
+ \sum_{\gamma} \frac{f_3^\gamma}{4} \sum_{\langle i,j \rangle_\gamma} \Big[& U_{in}V_{il}U_{jm}V_{jp} + U_{in}U_{jl}U_{im}U_{jp} + U_{in}V_{jl}U_{im}V_{jp} \\
& + U_{jn}V_{il}U_{jm}V_{ip} + V_{in}V_{jl}V_{im}V_{jp} + U_{jn}V_{jl}U_{im}V_{ip} \\
& + (n \leftrightarrow l; m \leftrightarrow p; nl \leftrightarrow mp) \Big] + (i \leftrightarrow j)
\end{aligned}$$

C.6 Temperature Estimation

In order to compute the scattering processes described in section 5.4 we need an estimate of the temperature of the system. To get it, we compare the energy measured in the experimental system with the energy of a thermal state of magnons in our mean-field calculation. What is measured experimentally is an average over all the bonds of the lattice

$$E_{exp}(T) = \frac{1}{N_b} \sum_{\langle i,j \rangle} \frac{\langle X_i X_j + Y_i Y_j \rangle_T}{2} \tag{C.4}$$

We take into account the conventions in our analysis to get

$$E_{exp}(T) = -(S+1) + \frac{1}{J_1 N_b} \sum_k \epsilon(k) + \frac{2}{J_1 N_b} \sum_k \frac{\epsilon(k)}{e^{\beta \epsilon(k)} - 1}$$

where the first two terms are the ground state energy for the finite-size system and the last term is the thermal distribution of magnons at temperature $T = 1/\beta$. The eigenvalues $\epsilon(\mathbf{k})$ are the same we computed in section 5.2. We then derive a temperature dependence of the energy which gives (see Figure C.2) a temperature of $\sim 8MHz$ for an experimentally measured energy of ~ -0.5 MHz in a 7×8 system. This temperature falls between the second and third excited mode.

References

[1] F. Yao *et al.*, Nature Communications **15**, 10377 (2024), Publisher: Nature Publishing Group.

[2] J. Motruk, D. Rossi, D. A. Abanin, and L. Rademaker, Physical Review Research **5**, L022049 (2023), Publisher: American Physical Society.

[3] D. Rossi, J. Motruk, L. Rademaker, and D. A. Abanin, Physical Review B **108**, 144406 (2023), Publisher: American Physical Society.

[4] T. I. Andersen *et al.*, Nature **638**, 79 (2025), Publisher: Nature Publishing Group.

[5] W. Heisenberg, Zeitschrift für Physik **49**, 619 (1928).

[6] L. Savary and L. Balents, Reports on Progress in Physics **80**, 016502 (2016), Publisher: IOP Publishing.

[7] N. D. Mermin and H. Wagner, Physical Review Letters **17**, 1307 (1966), Publisher: American Physical Society.

[8] P. W. Anderson, Materials Research Bulletin **8**, 153 (1973).

[9] A. Kitaev, Annals of Physics **321**, 2 (2006).

[10] T.-H. Han *et al.*, Nature **492**, 406 (2012), Publisher: Nature Publishing Group.

[11] L. Balents, Nature **464**, 199 (2010), Publisher: Nature Publishing Group.

[12] Y. Shimizu, K. Miyagawa, K. Kanoda, M. Maesato, and G. Saito, Physical Review Letters **91**, 107001 (2003), Publisher: American Physical Society.

[13] P. A. Lee, N. Nagaosa, and X.-G. Wen, Reviews of Modern Physics **78**, 17 (2006), Publisher: American Physical Society.

[14] D. J. Scalapino, Reviews of Modern Physics **84**, 1383 (2012), Publisher: American Physical Society.

[15] A. Y. Kitaev, Annals of Physics **303**, 2 (2003).

[16] C. Nayak, S. H. Simon, A. Stern, M. Freedman, and S. Das Sarma, Reviews of Modern Physics **80**, 1083 (2008), Publisher: American Physical Society.

[17] L. Balents, C. R. Dean, D. K. Efetov, and A. F. Young, Nature Physics **16**, 725 (2020), Publisher: Nature Publishing Group.

[18] E. Altman *et al.*, PRX Quantum **2**, 017003 (2021), Publisher: American Physical Society.

[19] P. Mellado, Journal of Physics. Condensed Matter: An Institute of Physics Journal **37** (2025).

[20] R. P. Feynman, International Journal of Theoretical Physics **21**, 467 (1982).

[21] M. H. Devoret and R. J. Schoelkopf, Science **339**, 1169 (2013), Publisher: American Association for the Advancement of Science.

[22] D. Jaksch and P. Zoller, Annals of Physics **315**, 52 (2005).

[23] J. I. Cirac and P. Zoller, Physical Review Letters **74**, 4091 (1995), Publisher: American Physical Society.

[24] A. Browaeys and T. Lahaye, Nature Physics **16**, 132 (2020), Publisher: Nature Publishing Group.

[25] P. Lecheminant, B. Bernu, C. Lhuillier, L. Pierre, and P. Sindzingre, Physical Review B **56**, 2521 (1997), Publisher: American Physical Society.

[26] A. M. Läuchli, J. Sudan, and R. Moessner, Physical Review B **100**, 155142 (2019), Publisher: American Physical Society.

[27] S. R. White, Physical Review Letters **69**, 2863 (1992), Publisher: American Physical Society.

[28] E. M. Stoudenmire and S. R. White, Annual Review of Condensed Matter Physics **3**, 111 (2012), Publisher: Annual Reviews.

[29] W. M. C. Foulkes, L. Mitas, R. J. Needs, and G. Rajagopal, Reviews of Modern Physics **73**, 33 (2001), Publisher: American Physical Society.

[30] R. Bistritzer and A. H. MacDonald, Proceedings of the National Academy of Sciences **108**, 12233 (2011), Company: National Academy of Sciences Distributor: National Academy of Sciences ISBN: 9781108174107 Institution: National Academy of Sciences Label: National Academy of Sciences Publisher: Proceedings of the National Academy of Sciences.

[31] M. Gibertini, Journal of Physics D: Applied Physics **54**, 064002 (2020), Publisher: IOP Publishing.

[32] Y. Cao *et al.*, Nature **556**, 80 (2018), Publisher: Nature Publishing Group.

[33] E. Y. Andrei and A. H. MacDonald, Nature Materials **19**, 1265 (2020), Publisher: Nature Publishing Group.

[34] K. F. Mak and J. Shan, Nature Nanotechnology **17**, 686 (2022), Publisher: Nature Publishing Group.

[35] X. Wang *et al.*, Nature **604**, 468 (2022), Publisher: Nature Publishing Group.

[36] Y. Tang *et al.*, Nature Nanotechnology **18**, 233 (2023), Publisher: Nature Publishing Group.

[37] E. Anderson *et al.*, Science **381**, 325 (2023), Publisher: American Association for the Advancement of Science.

[38] G. Gatti *et al.*, In preparation .

[39] D. Rossi, G. Gatti, F. Baumberger, and L. Rademaker, In preparation .

[40] T. W. B. Kibble, Journal of Physics A: Mathematical and General **9**, 1387 (1976).

[41] W. H. Zurek, Nature **317**, 505 (1985), Publisher: Nature Publishing Group.

[42] T. Holstein and H. Primakoff, Physical Review **58**, 1098 (1940), Publisher: American Physical Society.

[43] F. Escudero, A. Sinner, Z. Zhan, P. A. Pantaleón, and F. Guinea, Physical Review Research **6**, 023203 (2024), Publisher: American Physical Society.

[44] Y. Cao *et al.*, Nature **556**, 43 (2018), Publisher: Nature Publishing Group.

[45] A. L. Sharpe *et al.*, Science **365**, 605 (2019), Publisher: American Association for the Advancement of Science.

[46] L. Ciorciaro *et al.*, Nature **623**, 509 (2023), Publisher: Nature Publishing Group.

[47] L. Wang *et al.*, Nature Materials **19**, 861 (2020), Publisher: Nature Publishing Group.

[48] T. Song *et al.*, Science **374**, 1140 (2021), Publisher: American Association for the Advancement of Science.

[49] Y. Xu *et al.*, Nature Nanotechnology **17**, 143 (2022), Number: 2 Publisher: Nature Publishing Group.

[50] H. Xie *et al.*, Nature Physics **19**, 1150 (2023), Publisher: Nature Publishing Group.

[51] G. Cheng *et al.*, Nature Electronics **6**, 434 (2023), Publisher: Nature Publishing Group.

[52] C. Boix-Constant *et al.*, Nature Materials **23**, 212 (2024), Publisher: Nature Publishing Group.

[53] C. N. Lau, M. W. Bockrath, K. F. Mak, and F. Zhang, Nature **602**, 41 (2022), Publisher: Nature Publishing Group.

[54] M. Kapfer *et al.*, Science **381**, 677 (2023), Publisher: American Association for the Advancement of Science.

[55] L. Li and M. Wu, ACS Nano **11**, 6382 (2017), Publisher: American Chemical Society.

[56] E. C. Regan *et al.*, Nature Reviews Materials **7**, 778 (2022), Publisher: Nature Publishing Group.

[57] Q. Tong, F. Liu, J. Xiao, and W. Yao, Nano Letters **18**, 7194 (2018), Publisher: American Chemical Society.

[58] K. Hejazi, Z.-X. Luo, and L. Balents, Proceedings of the National Academy of Sciences **117**, 10721 (2020), Publisher: Proceedings of the National Academy of Sciences.

[59] C. Wang, Y. Gao, H. Lv, X. Xu, and D. Xiao, Physical Review Letters **125**, 247201 (2020), Publisher: American Physical Society.

[60] F. Xiao, K. Chen, and Q. Tong, Physical Review Research **3**, 013027 (2021), Publisher: American Physical Society.

[61] M. Akram and O. Erten, Physical Review B **103**, L140406 (2021), Publisher: American Physical Society.

[62] M. Akram *et al.*, Nano Letters **21**, 6633 (2021), Publisher: American Chemical Society.

[63] H. Xie *et al.*, Nature Physics **18**, 30 (2022), Publisher: Nature Publishing Group.

[64] B. Yang, Y. Li, H. Xiang, H. Lin, and B. Huang, Nature Computational Science **3**, 314 (2023), Publisher: Nature Publishing Group.

[65] A. O. Fumega and J. L. Lado, 2D Materials **10**, 025026 (2023), Publisher: IOP Publishing.

[66] W. Chen *et al.*, Science **366**, 983 (2019), Publisher: American Association for the Advancement of Science.

[67] M. Kim *et al.*, Nature Electronics **2**, 457 (2019), Publisher: Nature Publishing Group.

[68] F. Yao *et al.*, Nature Communications **14**, 4969 (2023), Number: 1 Publisher: Nature Publishing Group.

[69] H. H. Kim *et al.*, Proceedings of the National Academy of Sciences **116**, 11131 (2019), Publisher: Proceedings of the National Academy of Sciences.

[70] Z. Wang *et al.*, Nature Communications **12**, 6659 (2021), Publisher: Nature Publishing Group.

[71] D. R. Klein *et al.*, Science **360**, 1218 (2018), Publisher: American Association for the Advancement of Science.

[72] H. H. Kim *et al.*, Nano Letters **18**, 4885 (2018), Publisher: American Chemical Society.

[73] T. Song *et al.*, Science **360**, 1214 (2018), Publisher: American Association for the Advancement of Science.

[74] Z. Wang *et al.*, Nature Communications **9**, 2516 (2018), Publisher: Nature Publishing Group.

[75] K. F. Mak, J. Shan, and D. C. Ralph, Nature Reviews Physics **1**, 646 (2019), Publisher: Nature Publishing Group.

[76] C. Tan *et al.*, Nature Communications **9**, 1554 (2018), Publisher: Nature Publishing Group.

[77] J. M. D. Coey, *Magnetism and Magnetic Materials* (Cambridge University Press, Cambridge, 2010).

[78] Z. Wang *et al.*, Nano Letters **18**, 4303 (2018), Publisher: American Chemical Society.

[79] C. K. Singh and M. Kabir, Physical Review Materials **6**, 084407 (2022), Publisher: American Physical Society.

[80] Z. Cai *et al.*, Physical Review B **104**, L020402 (2021).

[81] W. Sun *et al.*, ACS Applied Nano Materials **6**, 17021 (2023), Publisher: American Chemical Society.

[82] A. O. Fumega *et al.*, Journal of Materials Chemistry C **8**, 13582 (2020), Publisher: The Royal Society of Chemistry.

[83] S. Nikitin *et al.*, Physical Review Letters **129**, 127201 (2022), Publisher: American Physical Society.

[84] D. Sasamoto and J. Nasu, Schwinger boson theory for $S=1$ Kitaev quantum spin liquids, 2025, arXiv:2509.25761 [cond-mat].

[85] V. Kalmeyer and R. B. Laughlin, Physical Review Letters **59**, 2095 (1987), Publisher: American Physical Society.

[86] D. F. Schroeter, E. Kapit, R. Thomale, and M. Greiter, Physical Review Letters **99**, 097202 (2007), Publisher: American Physical Society.

[87] Y. Tang *et al.*, Nature **579**, 353 (2020), Publisher: Nature Publishing Group.

[88] E. C. Regan *et al.*, Nature **579**, 359 (2020), Publisher: Nature Publishing Group.

[89] T. Li *et al.*, Nature **597**, 350 (2021), Publisher: Nature Publishing Group.

[90] A. Ghiotto *et al.*, Nature **597**, 345 (2021), Publisher: Nature Publishing Group.

[91] T. Li *et al.*, Nature **600**, 641 (2021), Publisher: Nature Publishing Group.

[92] Y. Xu *et al.*, Nature **587**, 214 (2020), Publisher: Nature Publishing Group.

[93] X. Huang *et al.*, Nature Physics **17**, 715 (2021), Publisher: Nature Publishing Group.

[94] H. Li *et al.*, Nature Materials **20**, 945 (2021), Publisher: Nature Publishing Group.

[95] E. Liu *et al.*, Physical Review Letters **127**, 037402 (2021), Publisher: American Physical Society.

[96] S. Miao *et al.*, Nature Communications **12**, 3608 (2021), Publisher: Nature Publishing Group.

[97] F. Wu, T. Lovorn, E. Tutuc, and A. MacDonald, Physical Review Letters **121**, 026402 (2018), Publisher: American Physical Society.

[98] Y. Zhang, N. F. Q. Yuan, and L. Fu, Physical Review B **102**, 201115 (2020), Publisher: American Physical Society.

[99] L. Rademaker, Physical Review B **105**, 195428 (2022), Publisher: American Physical Society.

[100] Y. Zhang, T. Devakul, and L. Fu, Proceedings of the National Academy of Sciences **118**, e2112673118 (2021), Publisher: Proceedings of the National Academy of Sciences.

[101] M. Takahashi, Journal of Physics C: Solid State Physics **10**, 1289 (1977).

[102] H. Pan, F. Wu, and S. Das Sarma, Physical Review Research **2**, 033087 (2020), Publisher: American Physical Society.

[103] J. Zang, J. Wang, J. Cano, and A. J. Millis, Physical Review B **104**, 075150 (2021), Publisher: American Physical Society.

[104] A. Wietek *et al.*, Physical Review Research **4**, 043048 (2022), Publisher: American Physical Society.

[105] L. Messio, S. Bieri, C. Lhuillier, and B. Bernu, Physical Review Letters **118**, 267201 (2017), Publisher: American Physical Society.

[106] L. Messio, O. Cépas, and C. Lhuillier, Physical Review B **81**, 064428 (2010), Publisher: American Physical Society.

[107] K. Mondal and C. Kadolkar, Physical Review B **95**, 134404 (2017), Publisher: American Physical Society.

[108] Y. Huh, L. Fritz, and S. Sachdev, Physical Review B **81**, 144432 (2010), Publisher: American Physical Society.

[109] M. Norman, Reviews of Modern Physics **88**, 041002 (2016), Publisher: American Physical Society.

[110] P. Mendels and F. Bert, Comptes Rendus. Physique **17**, 455 (2016).

[111] J. Knolle and R. Moessner, Annual Review of Condensed Matter Physics **10**, 451 (2019), Publisher: Annual Reviews.

[112] H. C. Jiang, Z. Y. Weng, and D. N. Sheng, Physical Review Letters **101**, 117203 (2008), Publisher: American Physical Society.

[113] S. Yan, D. A. Huse, and S. R. White, Science **332**, 1173 (2011), Publisher: American Association for the Advancement of Science.

[114] H. Liao *et al.*, Physical Review Letters **118**, 137202 (2017), Publisher: American Physical Society.

[115] Y.-C. He, M. P. Zaletel, M. Oshikawa, and F. Pollmann, Physical Review X **7**, 031020 (2017), Publisher: American Physical Society.

[116] Y. Iqbal *et al.*, Physical Review B **104**, 144406 (2021), Publisher: American Physical Society.

[117] M. P. Shores, E. A. Nytko, B. M. Bartlett, and D. G. Nocera, Journal of the American Chemical Society **127**, 13462 (2005), Publisher: American Chemical Society.

[118] J. S. Helton *et al.*, Physical Review Letters **98**, 107204 (2007), Publisher: American Physical Society.

[119] F. Bert *et al.*, Physical Review B **76**, 132411 (2007), Publisher: American Physical Society.

[120] P. Mendels *et al.*, Physical Review Letters **98**, 077204 (2007), Publisher: American Physical Society.

[121] P. Khuntia *et al.*, Nature Physics **16**, 469 (2020), Publisher: Nature Publishing Group.

[122] F. H. Aidoudi *et al.*, Nature Chemistry **3**, 801 (2011), Publisher: Nature Publishing Group.

[123] B. Fåk *et al.*, Physical Review Letters **109**, 037208 (2012), Publisher: American Physical Society.

[124] L. Clark *et al.*, Physical Review Letters **110**, 207208 (2013), Publisher: American Physical Society.

[125] X.-H. Chen, Y.-X. Huang, Y. Pan, and J.-X. Mi, Journal of Magnetism and Magnetic Materials **512**, 167066 (2020).

[126] Z. Zeng *et al.*, Physical Review B **105**, L121109 (2022), Publisher: American Physical Society.

[127] J. Liu *et al.*, Physical Review B **105**, 024418 (2022), Publisher: American Physical Society.

[128] F. Lu *et al.*, Communications Physics **5**, 272 (2022), Publisher: Nature Publishing Group.

[129] S. Sachdev, Physical Review B **45**, 12377 (1992), Publisher: American Physical Society.

[130] Y. Ran, M. Hermele, P. A. Lee, and X.-G. Wen, Physical Review Letters **98**, 117205 (2007), Publisher: American Physical Society.

[131] M. Hermele, Y. Ran, P. A. Lee, and X.-G. Wen, Physical Review B **77**, 224413 (2008), Publisher: American Physical Society.

[132] Y.-M. Lu, Y. Ran, and P. A. Lee, Physical Review B **83**, 224413 (2011), Publisher: American Physical Society.

[133] L. Messio, B. Bernu, and C. Lhuillier, Physical Review Letters **108**, 207204 (2012), Publisher: American Physical Society.

[134] T. Tay and O. I. Motrunich, Physical Review B **84**, 020404 (2011), Publisher: American Physical Society.

[135] Y. Iqbal, F. Becca, and D. Poilblanc, Physical Review B **84**, 020407 (2011), Publisher: American Physical Society.

[136] Y. Iqbal, F. Becca, S. Sorella, and D. Poilblanc, Physical Review B **87**, 060405 (2013), Publisher: American Physical Society.

[137] Y. Iqbal, D. Poilblanc, and F. Becca, Physical Review B **89**, 020407 (2014), Publisher: American Physical Society.

[138] F. L. Buessen and S. Trebst, Physical Review B **94**, 235138 (2016), Publisher: American Physical Society.

[139] M. Hering, J. Sonnenschein, Y. Iqbal, and J. Reuther, Physical Review B **99**, 100405 (2019), Publisher: American Physical Society.

[140] J. Thoenniss, M. K. Ritter, F. B. Kugler, J. v. Delft, and M. Punk, Multiloop pseudofermion functional renormalization for quantum spin systems: Application to the spin-$\frac{1}{2}$ kagome Heisenberg model, 2020, arXiv:2011.01268 [cond-mat].

[141] J. T. Chalker and J. F. G. Eastmond, Physical Review B **46**, 14201 (1992), Publisher: American Physical Society.

[142] P. W. Leung and V. Elser, Physical Review B **47**, 5459 (1993), Publisher: American Physical Society.

[143] C. Waldtmann *et al.*, The European Physical Journal B - Condensed Matter and Complex Systems **2**, 501 (1998).

[144] H. Nakano and T. Sakai, Journal of the Physical Society of Japan **80**, 053704 (2011), Publisher: The Physical Society of Japan.

[145] A. M. Läuchli, J. Sudan, and E. S. Sørensen, Physical Review B **83**, 212401 (2011), Publisher: American Physical Society.

[146] S. Depenbrock, I. P. McCulloch, and U. Schollwöck, Physical Review Letters **109**, 067201 (2012), Publisher: American Physical Society.

[147] H.-C. Jiang, Z. Wang, and L. Balents, Nature Physics **8**, 902 (2012), Publisher: Nature Publishing Group.

[148] H. J. Changlani, D. Kochkov, K. Kumar, B. K. Clark, and E. Fradkin, Physical Review Letters **120**, 117202 (2018), Publisher: American Physical Society.

[149] W. Zhu, X. Chen, Y.-C. He, and W. Witczak-Krempa, Science Advances **4**, eaat5535 (2018), Publisher: American Association for the Advancement of Science.

[150] Z. Xie *et al.*, Physical Review X **4**, 011025 (2014), Publisher: American Physical Society.

[151] J.-W. Mei, J.-Y. Chen, H. He, and X.-G. Wen, Physical Review B **95**, 235107 (2017), Publisher: American Physical Society.

[152] S. Jiang, P. Kim, J. H. Han, and Y. Ran, SciPost Physics **7**, 006 (2019).

[153] Y. Iqbal, F. Becca, and D. Poilblanc, Physical Review B **83**, 100404 (2011), Publisher: American Physical Society.

[154] R. Suttner, C. Platt, J. Reuther, and R. Thomale, Physical Review B **89**, 020408 (2014), Publisher: American Physical Society.

[155] Y. Iqbal, D. Poilblanc, and F. Becca, Physical Review B **91**, 020402 (2015), Publisher: American Physical Society.

[156] F. Kolley, S. Depenbrock, I. P. McCulloch, U. Schollwöck, and V. Alba, Physical Review B **91**, 104418 (2015), Publisher: American Physical Society.

[157] S.-S. Gong, W. Zhu, and D. N. Sheng, Scientific Reports **4**, 6317 (2014), Publisher: Nature Publishing Group.

[158] S.-S. Gong, W. Zhu, L. Balents, and D. N. Sheng, Physical Review B **91**, 075112 (2015), Publisher: American Physical Society.

[159] Q.-C. Sun *et al.*, Nature Communications **12**, 1989 (2021).

[160] I. Dzyaloshinsky, Journal of Physics and Chemistry of Solids **4**, 241 (1958).

[161] T. Moriya, Physical Review **120**, 91 (1960), Publisher: American Physical Society.

[162] O. Cépas, C. M. Fong, P. W. Leung, and C. Lhuillier, Physical Review B **78**, 140405 (2008), Publisher: American Physical Society.

[163] I. Rousochatzakis, S. R. Manmana, A. M. Läuchli, B. Normand, and F. Mila, Physical Review B **79**, 214415 (2009), Publisher: American Physical Society.

[164] C.-Y. Lee, B. Normand, and Y.-J. Kao, Physical Review B **98**, 224414 (2018), Publisher: American Physical Society.

[165] M. Hering and J. Reuther, Physical Review B **95**, 054418 (2017), Publisher: American Physical Society.

[166] F. L. Buessen, V. Noculak, S. Trebst, and J. Reuther, Physical Review B **100**, 125164 (2019), Publisher: American Physical Society.

[167] R. Thomale, E. Kapit, D. F. Schroeter, and M. Greiter, Physical Review B **80**, 104406 (2009), Publisher: American Physical Society.

[168] Y.-C. He, D. Sheng, and Y. Chen, Physical Review Letters **112**, 137202 (2014), Publisher: American Physical Society.

[169] Y.-C. He and Y. Chen, Physical Review Letters **114**, 037201 (2015), Publisher: American Physical Society.

[170] A. Wietek and A. M. Läuchli, Physical Review B **102**, 020411 (2020), Publisher: American Physical Society.

[171] A. Auerbach and D. P. Arovas, Physical Review Letters **61**, 617 (1988), Publisher: American Physical Society.

[172] A. Auerbach, *Interacting Electrons and Quantum Magnetism*Graduate Texts in Contemporary Physics (Springer, New York, NY, 1994).

[173] X.-G. Wen, Physical Review B **65**, 165113 (2002), Publisher: American Physical Society.

[174] L. Messio, C. Lhuillier, and G. Misguich, Physical Review B **87**, 125127 (2013).

[175] J. H. P. Colpa, Physica A: Statistical Mechanics and its Applications **93**, 327 (1978).

[176] G. Misguich, Physical Review B **86**, 245132 (2012), Publisher: American Physical Society.

[177] F. Wang and A. Vishwanath, Physical Review B **74**, 174423 (2006), Publisher: American Physical Society.

[178] J. C. Halimeh and M. Punk, Physical Review B **94**, 104413 (2016), Publisher: American Physical Society.

[179] F. A. Gómez Albarracín and P. Pujol, Physical Review B **97**, 104419 (2018), Publisher: American Physical Society.

[180] L. Messio, C. Lhuillier, and G. Misguich, Physical Review B **83**, 184401 (2011), Publisher: American Physical Society.

[181] D. Kiese, Y. He, C. Hickey, A. Rubio, and D. M. Kennes, APL Materials **10**, 031113 (2022).

[182] K. Mondal and C. Kadolkar, Journal of Physics: Condensed Matter **33**, 505801 (2021), Publisher: IOP Publishing.

[183] M. Claassen, L. Xian, D. M. Kennes, and A. Rubio, Nature Communications **13**, 4915 (2022), Publisher: Nature Publishing Group.

[184] A. P. Reddy, T. Devakul, and L. Fu, Physical Review Letters **131**, 246501 (2023), Publisher: American Physical Society.

[185] J. Dziarmaga, Physical Review Letters **95**, 245701 (2005), Publisher: American Physical Society.

[186] W. H. Zurek, U. Dorner, and P. Zoller, Physical Review Letters **95**, 105701 (2005).

[187] A. Polkovnikov, Physical Review B **72**, 161201 (2005).

[188] A. Ali *et al.*, Nature Communications **15**, 10756 (2024), arXiv:2403.00091 [quant-ph].

[189] A. del Campo and W. H. Zurek, International Journal of Modern Physics A **29**, 1430018 (2014), Publisher: World Scientific Publishing Co.

[190] N. Navon, A. L. Gaunt, R. P. Smith, and Z. Hadzibabic, Science **347**, 167 (2015), Publisher: American Association for the Advancement of Science.

[191] A. Keesling *et al.*, Nature **568**, 207 (2019).

[192] S. Ebadi *et al.*, Nature **595**, 227 (2021), Publisher: Nature Publishing Group.

[193] J. M. Kosterlitz and D. J. Thouless, Journal of Physics C: Solid State Physics **6**, 1181 (1973).

[194] S. Lloyd, Science **273**, 1073 (1996), Publisher: American Association for the Advancement of Science.

[195] J. Clarke, A. N. Cleland, M. H. Devoret, D. Esteve, and J. M. Martinis, Science **239**, 992 (1988), Publisher: American Association for the Advancement of Science.

[196] F. Arute *et al.*, Nature **574**, 505 (2019), Publisher: Nature Publishing Group.

[197] S. Rasmussen *et al.*, PRX Quantum **2**, 040204 (2021), Publisher: American Physical Society.

[198] A. Rasmussen, Y.-Z. You, and C. Xu, Stable Gapless Bose Liquid Phases without any Symmetry, 2016, arXiv:1601.08235 [cond-mat].

[199] J. A. Schreier *et al.*, Physical Review B **77**, 180502 (2008), Publisher: American Physical Society.

[200] J. Koch *et al.*, Physical Review A **76**, 042319 (2007), Publisher: American Physical Society.

[201] C. Neill *et al.*, Nature Physics **12**, 1037 (2016), Publisher: Nature Publishing Group.

[202] P. Roushan *et al.*, Science **358**, 1175 (2017), Publisher: American Association for the Advancement of Science.

[203] E. Bairey, I. Arad, and N. H. Lindner, Physical Review Letters **122**, 020504 (2019), Publisher: American Physical Society.

[204] T. J. Evans, R. Harper, and S. T. Flammia, Scalable Bayesian Hamiltonian learning, 2019, arXiv:1912.07636 [quant-ph].

[205] C. Chen *et al.*, Nature **616**, 691 (2023), Publisher: Nature Publishing Group.

[206] D. R. Nelson and J. M. Kosterlitz, Physical Review Letters **39**, 1201 (1977), Publisher: American Physical Society.

[207] R. H. Swendsen, Physical Review Letters **49**, 1302 (1982), Publisher: American Physical Society.

[208] J. Dziarmaga, Advances in Physics **59**, 1063 (2010).

[209] M. P. A. Fisher, P. B. Weichman, G. Grinstein, and D. S. Fisher, Physical Review B **40**, 546 (1989), Publisher: American Physical Society.

[210] R. Samajdar and D. A. Huse, Quantum and classical coarsening and their interplay with the Kibble-Zurek mechanism, 2024, arXiv:2401.15144 [cond-mat, physics:quant-ph].

[211] D. Sadhukhan *et al.*, Physical Review B **101**, 144429 (2020), Publisher: American Physical Society.

[212] G. Biroli, L. F. Cugliandolo, and A. Sicilia, Physical Review E **81**, 050101 (2010), Publisher: American Physical Society.

[213] A. Chandran, A. Erez, S. S. Gubser, and S. L. Sondhi, Physical Review B **86**, 064304 (2012), Publisher: American Physical Society.

[214] F. Bloch, Zeitschrift für Physik **61**, 206 (1930).

[215] J. C. Slater, Physical Review **52**, 198 (1937), Publisher: American Physical Society.

[216] V. A. Stephanovich and M. E. Zhitomirsky, Europhysics Letters **95**, 17007 (2011).

[217] M. E. Zhitomirsky and A. L. Chernyshev, Physical Review Letters **82**, 4536 (1999), Publisher: American Physical Society.

[218] M. Mourigal, M. E. Zhitomirsky, and A. L. Chernyshev, Physical Review B **82**, 144402 (2010), Publisher: American Physical Society.

[219] Y.-H. Chan, H.-C. Jiang, and Y.-C. Chen, Physical Review B **107**, 214402 (2023), Publisher: American Physical Society.

[220] H.-C. Jiang, H. Yao, and L. Balents, Physical Review B **86**, 024424 (2012), Publisher: American Physical Society.

[221] S.-S. Gong, W. Zhu, D. Sheng, O. I. Motrunich, and M. P. Fisher, Physical Review Letters **113**, 027201 (2014), Publisher: American Physical Society.

[222] F. Ferrari and F. Becca, Physical Review B **102**, 014417 (2020), Publisher: American Physical Society.

[223] P. Jordan and E. Wigner, Zeitschrift für Physik **47**, 631 (1928).